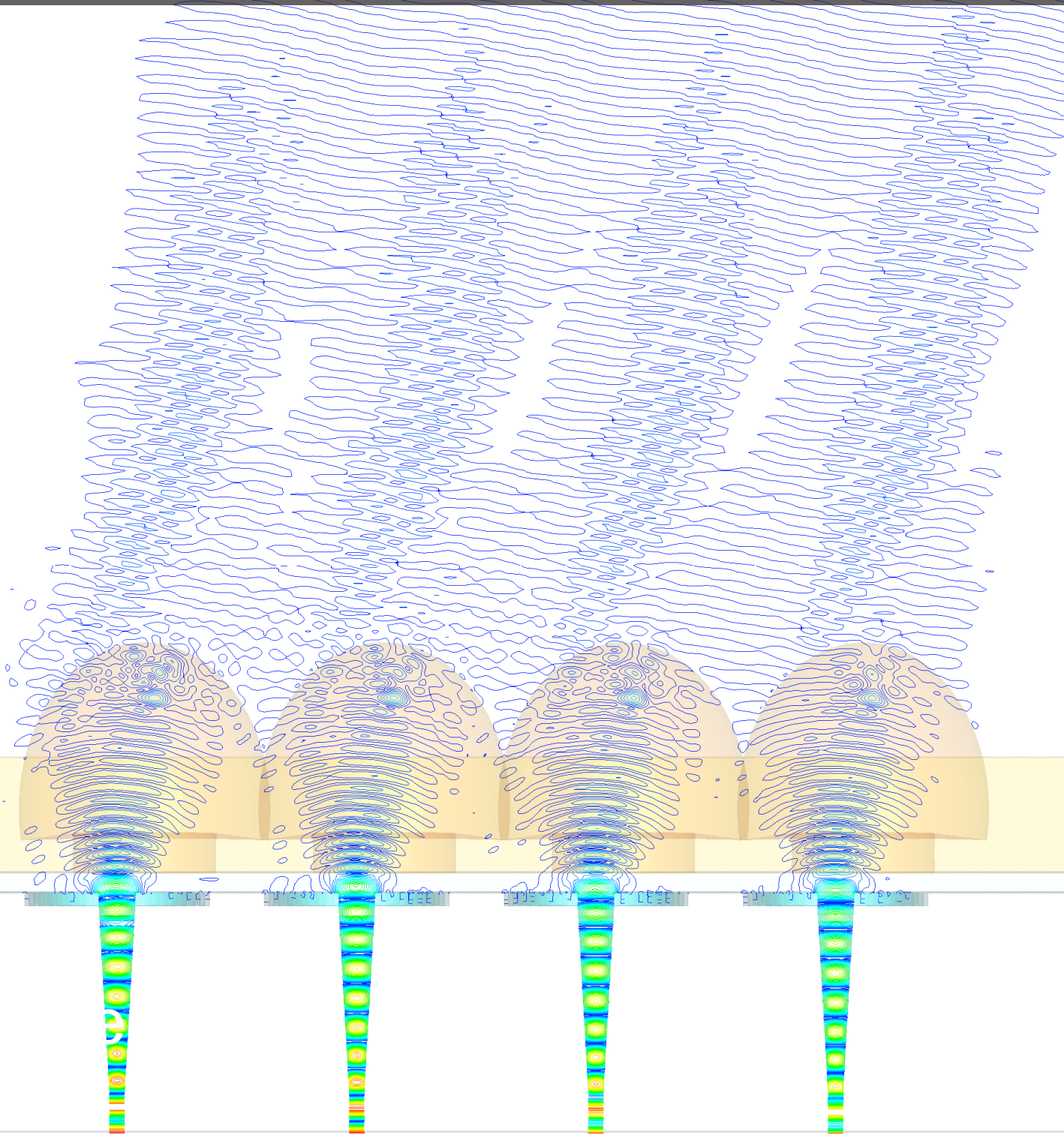


On the Development of a Lens Phased-Array at 100GHz

N. van Rooijen



On the Development of a Lens Phased-Array at 100GHz

by

N. van Rooijen

| Student Name | Student Number | Email address |
|------------------|----------------|---------------|
| Nick van Rooijen | 4378113 | - |

Supervisors: Prof. dr. Nuria Llombart Juan
Dr. Maria Alonso-delPino
Dr. Marco Spirito
Sjoerd Bosma

Institution: Delft University of Technology

Place: Faculty of Electrical Engineering, Delft

Project Duration: October, 2020 - June, 2021

Cover Image: E-field CST simulation of the proposed 4×1 array

Acknowledgements

Working on a thesis during times of COVID-19 can be challenging. Fortunately, I have had the support of many great people during this time period.

First of all, I would like to express my sincere gratitude to Sjoerd Bosma, my PhD supervisor. His willingness and friendliness to help is something I deeply admire. Despite his own full agenda, he would always find time somewhere to offer his insights and guidance whenever I got stuck with some random problem. I feel very fortunate to have been under his supervision for the past year.

Next, I would like to thank my three supervisors, Maria Alsonso-delPino, Nuria Llombart Juan and Marco Spirito for their help, expertise and patience throughout this year. In recognition of the difficulty of supervising from a distance, the three of them have done an excellent job of guiding me through the making of this thesis.

Of course, my roommates Wouter and Chris have also had their roles in the development of this thesis work. Their contributions to my home office environment have been invaluable. Their calls for coffee, lunches with 'snert' and 'knakworsten', and festive dinners have been important thesis fuels.

My friends of 't Zoldertje', thank you for the enduring friendship. I hope you can forgive my mental and physical absence during the final weeks of this thesis writing. With the writing of this master thesis, I realize how much time has passed since the group's founding during high school, some 10 years ago. I am certain that with the passage of even more time, we will share additional beautiful moments together.

Finally, I would also like to use this opportunity to thank my parents. They have offered their support and sanctuary in Maasland throughout my studies. As abstract and puzzling as my study may seem to them, they have always provided me the freedom to pursue my goals. Without you, I wouldn't be here ;)

N. van Rooijen
Delft, June 2021

Abstract

This thesis is concerned with a first time demonstration of a high frequency scanning lens phased-array with dynamic steering. Such phased-array could provide the high gain, wide bandwidth, and steering capability that the next generation of wireless applications requires. The phased-array development was divided into three distinct parts. First, the electronic phase steering system was discussed and developed, and its stability was characterized over time. Results obtained over 24 hours indicated that the system would be stable to within 6° of high frequency output phase. The drifts in output amplitude remained to within 0.3dB. Next, the lens antenna elements were developed with a novel corrugated leaky-wave feed that provides very high and broadband aperture efficiency. Antenna measurements have validated its ability to be a very aperture efficient radiator ($> 80\%$) with wide bandwidth (1:2). Scanning measurements have shown a 3dB scan loss at around 15° . Finally, the phase steering and antenna elements were combined into a 4×1 array concept. Its behaviour was simulated and indicated again good performance with wide bandwidth (1:2) and high directivity (31.5dBi). Simulated scan loss was approximately 3dB at 20° . The amplitude and phase errors resulted in a SLL standard deviation of 0.63dB. The array prototype is currently awaiting completion of fabrication by DEMO at the TU Delft.

Contents

| | |
|---|------------|
| Acknowledgements | iii |
| Abstract | v |
| 1 Introduction | 1 |
| 1.1 Context | 1 |
| 1.2 Scanning lens phased-arrays | 3 |
| 1.3 Thesis objectives | 5 |
| 2 Electronic steering of array factor | 7 |
| 2.1 Electronics overview | 7 |
| 2.1.1 Local Oscillators. | 8 |
| 2.1.2 IQ mixers and DAC. | 8 |
| 2.1.3 Frequency extenders | 9 |
| 2.2 Low frequency measurements | 10 |
| 2.2.1 Time drifts of the IQ mixers. | 12 |
| 2.3 High-frequency measurements | 13 |
| 2.3.1 Relative phases | 15 |
| 2.3.2 Time drifts of the high-frequency setup | 17 |
| 2.4 Discussion | 18 |
| 2.5 Summary | 19 |
| 3 Lens antenna based on a corrugated LW feed | 21 |
| 3.1 Leaky-wave feed with corrugated ground-plane: Dispersion equation . . | 22 |
| 3.2 Leaky-wave feed with corrugated ground-plane: Radiation performance | 24 |
| 3.2.1 Input reflection coefficient. | 24 |
| 3.2.2 Primary patterns. | 25 |
| 3.2.3 Aperture efficiency | 25 |
| 3.2.4 Secondary Patterns | 27 |
| 3.3 WR-5 Prototype. | 28 |
| 3.3.1 Simulated and measured performance | 30 |
| 3.4 Summary | 38 |
| 4 Scanning lens phased-array | 41 |
| 4.1 Geometry | 42 |
| 4.2 Performance of the Array. | 42 |
| 4.2.1 Broadside | 42 |
| 4.2.2 Scanned beam performance. | 43 |
| 4.2.3 Performance under phase and amplitude errors | 48 |
| 4.2.4 Discussion | 50 |

| | | |
|----------|--|-----------|
| 4.3 | Prototype development | 50 |
| 4.3.1 | Waveguide split block | 50 |
| 4.3.2 | Lens structure | 52 |
| 4.3.3 | Piezoelectric motor | 52 |
| 4.3.4 | Screws and connectors | 52 |
| 4.4 | Summary and outlook | 53 |
| 5 | Conclusion | 55 |
| | Bibliography | 57 |
| A | Modeling techniques for lens antennas | 61 |
| B | Lens-to-lens coupling | 63 |
| C | Additional near-field measurement results | 65 |

Introduction

1.1. Context

Recent developments in the antenna field have shown a general tendency to move towards higher frequencies, where more bandwidth is available and antenna dimensions are greatly reduced [1]. A wide range of new potential applications is being explored by moving to the millimeter- and submillimeter-wave frequencies. These include sensing, positioning, imaging and communications [2]. New antenna designs are required that are capable of handling large bandwidths with high gains, and have beam steering mechanisms.

One of the challenges of moving to these higher frequencies is the additional path loss. As described by the famous Friis' equation, the power transmitted between two isotropic antennas drops proportionally to the square of the frequency [3]. Highly directive beamformers that overcome the high path losses are the proposed solution. With large gains ($>30\text{dB}$) and bandwidths ($>20\%$), lens antennas could become a key enabler for future wireless applications [4].

However, many of these future applications will rely on a coverage of a certain Field of View (FoV), requiring beam steering of the highly directive patterns. FoVs of up to $\pm 25^\circ$ are demanded by some applications [5]. This angular range can be achieved with lenses by using a whole myriad of techniques. These include fly-eye arrays [4] and spherical-lens arrays [6], both consisting of individual lens elements covering a portion of the FoV. These kind of antennas are known as 'point-to-multipoint.'

A downside of these methods is that they do not provide dynamic steering that can compensate for the lower gain in their overlapping patterns. Some other commonly used methods that do not have this problem achieve the FoV coverage either mechanically or with phased array technologies. Of these two, the phased array is considered to be more reliable and possesses more rapid scanning than its mechanical counterpart [7].

However, there is also a major disadvantage of the phased-array concept, as it needs expensive phase control electronics. The costs of the phased array system are somewhat proportional to the directivity of the array: More beams fit into a certain required FoV, requiring more accurate phase control [8]. Furthermore, the shrinking of traditionally used half wavelength element spacing at higher frequencies poses significant constraints on active technology integration and thermal dissipation [5].

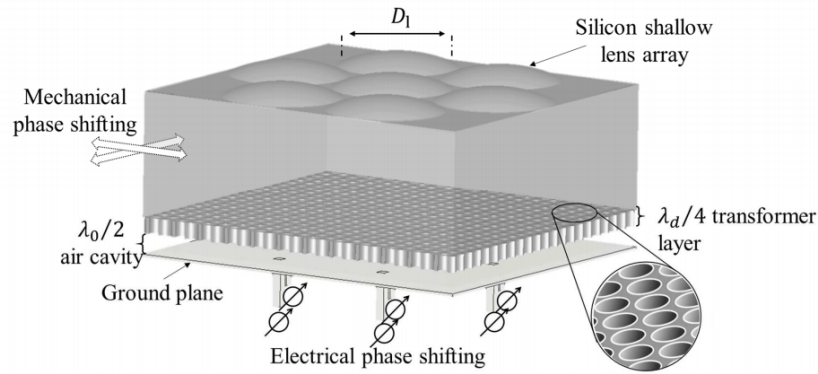


Figure 1.1: (a) Sparse phased-array concept at submm-wave frequencies, as presented in Alonso-delPino et al. ([5], Fig. 1.)

A solution is what is known as 'sparse arrays', where the distances between array elements exceed the half-wavelength grating lobe condition (Fig. 1.1). The subsequent grating lobes are then suppressed by "active element pattern control" [8]. Key to the success of this technique is having high gain element patterns, that offer attenuation at the angular locations of the grating lobes.

Early implementations of sparse arrays can be found in two 'thinned phased arrays' papers [9], [10]. Here, the use of a phased-array below a partially reflective surface allowed for the desired grating lobe suppression with high gain element patterns. Unfortunately, these examples lack in bandwidth ($< 6\%$) and their scanning is limited to the angular region of the element pattern. Thereby they do not meet the FoV and bandwidth criteria of many applications.

Unlike the thinned phased-array elements, a lens element is capable of scanning by electronically or mechanically displacing the feed away from the lens focus point [5]. This displacement is done in a single plane, greatly simplified with respect to azimuthal and elevational mechanical control. A promising novel technique is therefore to combine the agile beam steering of the phased-array with high gain, wide bandwidth and steerable lens antenna elements.

Such new antenna architecture is known as 'scanning lens phased-array' (SLPA). It is presented in a paper by Alonso-delPino et al [5], supported by the ERC LAA-THz-CC starting grant (639749, 2015). Their array geometry is illustrated in Fig. 1.1, showing lens diameters exceeding half a wavelength (10λ). The active element control is achieved by spatially displacing the lens with a piezoelectric motor, forming a (hybrid electro-mechanical) scanning lens (sparse) phased-array system. The advantages of such SLPA approach can easily be observed in the current state of the art in the upcoming section.

State of the art of high frequency phased-arrays

In this section we compare the SLPA system of [5] to the state of the art, summarized in Table 1.1. The brevity of this table is a good indicator of the novelty of the high frequency phased arrays.

With periodicities around 0.5 wavelengths, the first five table entries do not make use of the SLPA technique. The negative implication of this is shown in their directivities that do not exceed 17dBi, despite having up to 16 elements. As introduced in Sec-

Table 1.1: Overview of recent 100GHz+ phased-array implementations

| Author | N_{elem} | f [GHz] | periodicity | D [dBi] | SLL [dB] | scan loss [dB] |
|--------|--------------------|-----------|-------------------------------------|---------|---------------|--------------------|
| [11] | 8×1 | 370-410 | 0.5λ @400GHz | 15 | ≈ -15 | 5 @40° |
| [12] | 1×4 | 530 | 0.52λ | 14.3 | -13 | ≈ 1.5 @30° |
| [13] | 2×2 | 340 | x: 0.52λ , y: 0.89λ | 11.7 | - | - |
| [14] | 4×4 | 276-285 | 0.5λ | 16 | <-10 | ≈ 2 @30° |
| [15] | 4×4 | 108-114 | 0.5λ @110GHz | 17 | - | 2-2.5 @30° |
| [5] | hex-7 ^a | 550 | 10λ | 37.6 | -12.5 | 1.6 @25° |

^a Referring to a hexagonal geometry

Table entries indicated by '-' could not be found.

tion 1.1, the low directivity makes their implementations unsuitable for high-frequency links. Increasing the directivity by simply increasing the number of antenna elements might not be an option, as the additional electronic phase steering complexity could make commercial applications shy away [16].

A recent low frequency (28GHz) SLPA implementation of importance is the work by Zhang et al. [17]. A 4×4 array of lens elements with diameter $D_L = 2\lambda$ was developed, achieving a directivity of 27.4dBi.

A down-side of the SLPA is the achievable FoV that is limited by the steering properties of lenses. In practice, this is limited to around 20-30 degrees. However, it is due to the large directivity advantage that our work will aim to implement the SLPA. The paper by Alonso-delPino et al. [5] will serve as the foundation. However, this thesis will try to go a step further, aiming to create a SLPA prototype with dynamic steering.

1.2. Scanning lens phased-arrays

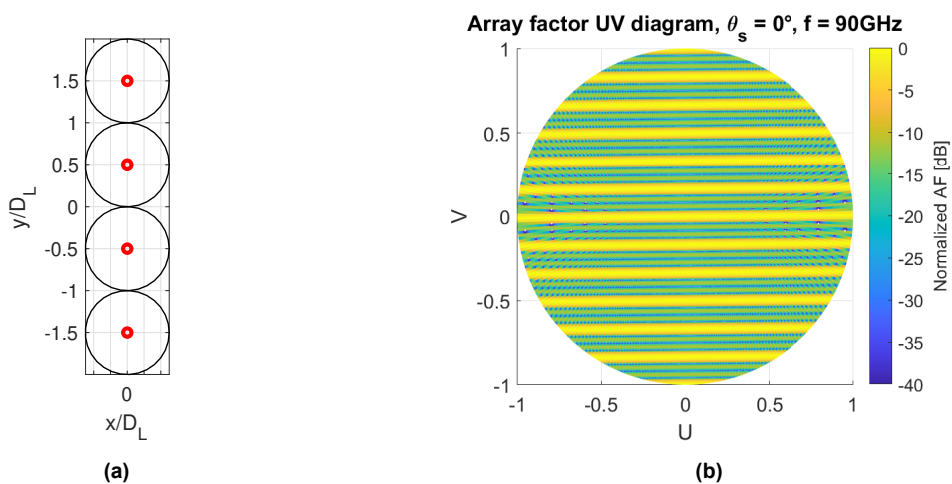


Figure 1.2: Linear array geometry (a) with its analytically derived, normalized AF at 90GHz (b).

To present the reader with the principle of operation of the SLPA, an idealized

example is presented here. Consider the geometry in Fig. 1.2a that involves four elements, each separated by $D_L > \lambda/2$. Its respective 2D Array Factor (AF) at 90GHz is shown in Fig. 1.2b. As expected, accompanying the main lobe are the side lobes as well as grating lobes due to the sparse array. Their locations and magnitudes depend on frequency and array geometry.

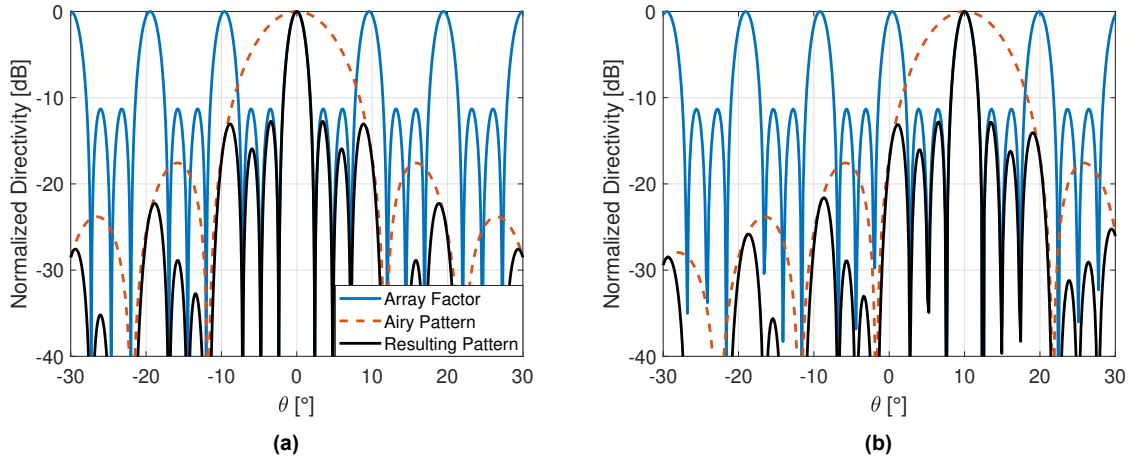


Figure 1.3: (a) E-plane Airy patterns and sparse array factors at 90 GHz including the pattern multiplication results. (a) shows the case for broadside, whereas (b) has both AF and element pattern scanning to 10° .

We can approximate the resulting SLPA pattern of such array geometry by multiplying the AF of Fig. 1.2b with an ideal 90GHz airy element pattern. The result is shown in Fig. 1.3a, where the highly directive element pattern is able to attenuate the grating lobe to a level of -12.7dB. This suppression is important for the functioning of the SLPA.

In order to apply beam steering, both the AF and the element pattern require separate shifting to the desired scanning angle. The former is performed by electronically phase shifting the input signals to each antenna element, whereas the latter is performed using a low power integrated piezoelectric motor. The technique is shown in Fig. 1.3b for a scanning angle of 10° . We can also use one of the grating lobes to scan to one of its integer multiples, as will be discussed later in Chapter 4. Using this technique, the ideal SLPA is able to steer to any desired scanning angle.

In practice, scanning will be limited by the scan losses induced by the lens steering properties via the mechanical displacement, as well as limits in the electronic phase shifting. Both phenomena will require further analysis for successful SLPA design.

Furthermore, practical functioning of the SLPA relies on lenses with high aperture efficiency. To see why, we can replace the ideal airy pattern of Fig. 1.3a with a lens of aperture efficiency less than unity. The result will be a drop in the element pattern grating lobe suppression capability. As stressed by Alonso-delPino et al. [5], it is therefore very important to have a lens design with very high aperture efficiency. The design of such a lens antenna approaching the ideal airy patterns is discussed in the next section.

A lens element with high aperture efficiency

The state of the art of individual lens antennas has been summarized in Arias Campo et al. ([4], Table 1). There, it was found that the use of Fabry-Pérot resonant leaky-wave feeding antennas can significantly increase the lens antenna aperture efficiency. This technique will therefore also be applied in this thesis.

Furthermore, our proposed lens will also use low $\epsilon_r = 2.3$ plastic HDPE material. This has several advantages over high ϵ_r materials, such as low costs and low dielectric loss [4]. The low dielectric constant also eliminates the need for expensive matching layers. The used material is in line with [4], [17] and [18].

However, this thesis diverges from earlier work of aforementioned authors by using special leaky-wave lens antenna elements with annular grooves cut into the antenna ground plane. This new concept will be referred to as a 'leaky-wave feeding antenna with corrugated ground plane' and will play an important role shaping the element patterns. Its design was optimized during an internship [19], but the concept still needs to be verified using measurements. This will be further explored using simulations and measurements in Chapter 3.

The design of corrugated lens antennas is just one of many design iterations required that determine the resulting array pattern. Array geometry type, element spacing and element excitation (phase, amplitude) are amongst the others. This thesis will cover all these aspects to develop a SLPA prototype.

1.3. Thesis objectives

Based on this brief introduction, the scope and objectives of this thesis can now be formulated. This work will focus on demonstrating dynamic beam steering with a lens phased-array for the first time. In close collaboration with the Electronic Circuits and Architectures (ELCA) Group at the TU Delft, their earlier work on phase-steering electronics will be combined with the antenna design expertise of the Terahertz Sensing (TS) Group. Our frequency of interest is 100GHz and above. However, for this work the experimental setup will be made near 100GHz due to the availability of components at the TU Delft.

This thesis will cover the phase steering mechanism, the individual antenna elements as well as the array design. The results of this report led to the creation of an actual array prototype, currently being fabricated at the time of writing. What this thesis will not cover is an integrated design of the above mentioned system. Nor will the thesis present an in-depth comparison of different suitable phase-steering electronics components. Rather, the electronic components were gathered that were at hand in both groups.

The rest of this thesis is structured as follows. Chapter 3 investigates the phased-array electronics architecture. A step-by-step approach is used to arrive at a final high frequency phase that is calibrated and is characterized over time. This system allows us to define the scanning limits and stability of the phased-array system. Then, chapter 3 continues the story by examining the individual antenna elements that constitute the phased-array. The use of corrugations is explained, together with the simulated and measured performance of an antenna that uses the same design principles. Finally, chapter 4 presents an overview of the array performance, combining the results of earlier chapters. Array simulations of the proposed prototype are discussed in this

chapter, together with its CAD development.

2

Electronic steering of array factor

In this chapter, we have developed an active system that can control the amplitude and phase of multiple electronic channels at 100GHz. The system can be used to electronically steer the array factor of the scanning lens phased array. Implementing the electronic steering system requires precise control of the amplitude and (relative) phase fed to each antenna element. The electronic control of amplitude and phase for a four-element array is achieved at low frequency (≈ 15 GHz) using IQ mixers. The frequency of these signals is then multiplied (x6) using frequency extenders to achieve the multi-channel phase and amplitude control in the WR-10 band using vectorized IQ-outputs. The electronic system configuration is described in more detail in section 2.1.

In this configuration, several non-idealities enter the system that degrade the desired vectorized outputs. These errors include amplitude and phase distortions, long-term drifts and short-term noise. Phase errors with certain variance σ^2 result in a loss of gain that is inversely proportional to the number of antenna elements [20]. Since the error analysis is more difficult at higher frequencies, the performance of the system and the analysis of these errors are first evaluated at the low frequency (i.e., without the extenders) in section 2.2 for two signal paths. In section 2.3, the frequency extenders are included and the performance is measured and analysed in the WR-10 band. These two different setups will be later referred to as 'low frequency setup' and 'high-frequency setup.' This chapter, together with the Chapter 3 antenna element, will thereby provide the groundwork for the later future phased array demonstration in Chapter 4.

2.1. Electronics overview

A system-level overview of the proposed electronic phase steering system for the scanning lens phased array, based on work by Visweswaran et al. [21], is shown in Fig. 2.1. Starting from the left, a low frequency local oscillator (LO) signal is generated at 12.5-18.3 GHz. This signal is amplified and split into four signal paths. Next, the LO signals pass through IQ mixers that control amplitude and phase of the output signal. The IQ-controlled signals are amplified once more and attenuated to achieve the required input power for the frequency extenders. The frequency extenders multiply their input signal by a factor 6. The resulting phase-controlled WR-10 signals are finally fed into the individual array antenna elements. Each of the steps in this

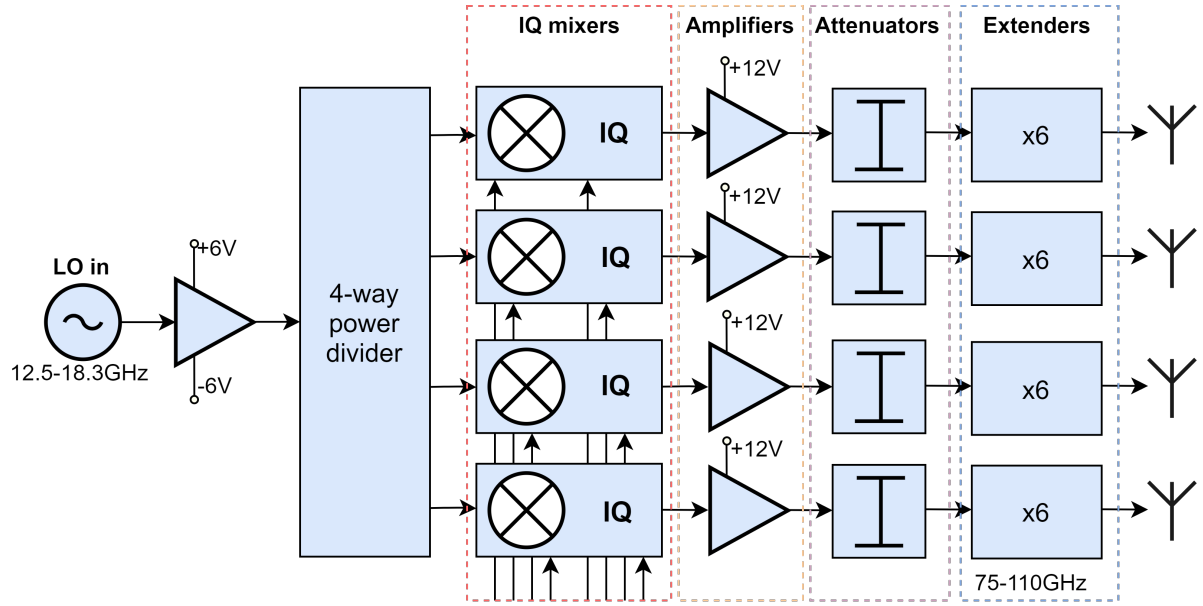


Figure 2.1: System level overview of the involved electronic steering system.

chain are explained in more detail in the next subsections. First, however, the main components are briefly discussed.

2.1.1. Local Oscillators

The $\approx 15\text{GHz}$ LO signal is generated in two different ways. For the low frequency setup, the LO is generated using one of the internal synthesizers of the 'P9374A Keysight Streamline USB Vector Network Analyzer' (VNA). This VNA output power was set to -5dBm . The 'Mini-Circuits ZVA-213-S+' gain block was used to amplify the signal before entering the 'MLDD 4-Way Power Divider 7005180.' This way, the desired $\approx 14\text{dBm}$ input power arrives at the IQ mixers.

Because the high-frequency setup needs a higher LO output power for the first stage amplifier (around 15.7dBm), an 'Agilent E8257D' signal generator was used. Subtracting the cable losses of 1.7dB , $\approx 14\text{dBm}$ of LO power was delivered to the 'Marki microwave A30EQP' first stage amplifier. This amplifier ensures that the IQ mixers are again fed with $\approx 14\text{dBm}$ LO input power.

2.1.2. IQ mixers and DAC

Amplitude and phase control at the low frequency is achieved using the IQ mixers. The operation of one such IR mixer is shown in Fig. 2.2a. An input LO signal is divided into an In-phase (I) and Quadrature phase (Q) path. The DC voltages V_I and V_Q are mixed with the I and Q signals, respectively, and then added to form the RF output. Since the control voltages are DC, the RF output has the same frequency as the LO input. By independently controlling V_I and V_Q , the RF output can be controlled in amplitude and phase. The amplitude can be described mathematically as $A_{IQ} = \sqrt{V_I^2 + V_Q^2}$ and the phase by $\phi_{IQ} = \tan^{-1}(V_Q/V_I)$ [22]. A polar coordinate system is thus used to describe the V_I, V_Q coordinates. For example, an in-phase ($V_I \neq 0, V_Q = 0$) control will result in a RF signal with phase equal to the input LO and amplitude $V_I \cdot V_{LO}$. By contrast,

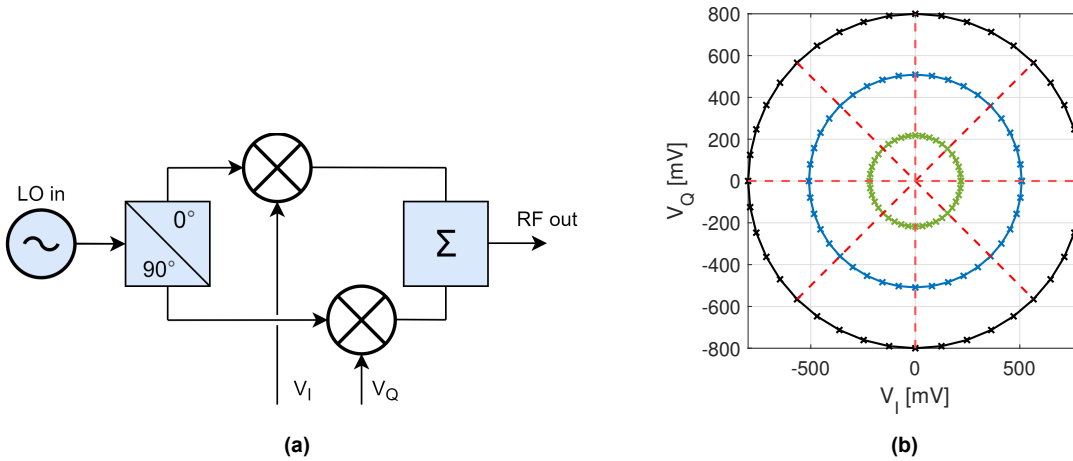


Figure 2.2: Schematic overview of IQ Mixer (a) and IQ diagram of phasor input (b).

the quadrature state ($V_I = 0, V_Q \neq 0$) results in a RF output that is 90° out of phase compared to the LO.

The used IQ mixers were MITEQ-IRM0226MC1Q models. V_I and V_Q are generated using a 16-bit NI PXI 6733 Digital to Analog Converter (DAC). This high number of bits permits us to safely ignore any phase quantization errors ([23], Fig. 7.7). The DAC V_I and V_Q voltages are limited to $\pm 0.8V$ to prevent damage to the mixers. The maximum output power of the mixers lies around -3dBm , which is not enough input power to drive the frequency extenders. Therefore, the high-frequency setup was equipped with amplifiers after the IQ mixing stage. Two ZVA-213-S gain blocks were used, followed by attenuation chains to bring the power to acceptable input levels for the extenders.

2.1.3. Frequency extenders

The conversion from the low frequency to the WR-10 frequency band is achieved using frequency extension modules (extenders), schematically illustrated in Fig. 2.3. The RF input is frequency multiplied by a factor N , in this case $N = 6$, and is passed through a bi-directional coupler before leaving the extender. The MEAS and REF ports, responsible for measuring the transmission and reflection signals respectively, will not be used in our setup. For the moment we are only interested in the frequency multiplication. For this reason the extender LO port will not be driven. The extenders that were used for the setup were 'Anritsu 3740A-EW' WR-10 extenders.

To ensure safe and stable operation of the extender modules, the input-output power relation of the extender modules was characterized. The Agilent LO signal generator is used in continuous wave mode, providing the frequency and power sweep of the input signals for the extenders. Extender output power is subsequently measured using the 'E4419A EPM Series' power meter with a WR-10 sensor.

The resulting input-output relation is shown in Fig. 2.4a and Fig. 2.4b for extenders 1 and 2, respectively. The extenders show different input response, with extender 2 reaching the maximum output saturation region at $\approx +1\text{dBm}$ input power, whereas extender 1 requires $\approx +8\text{dBm}$. To provide the required input power to each extender, amplifiers and attenuators were placed after the IQ mixers, as described in Section

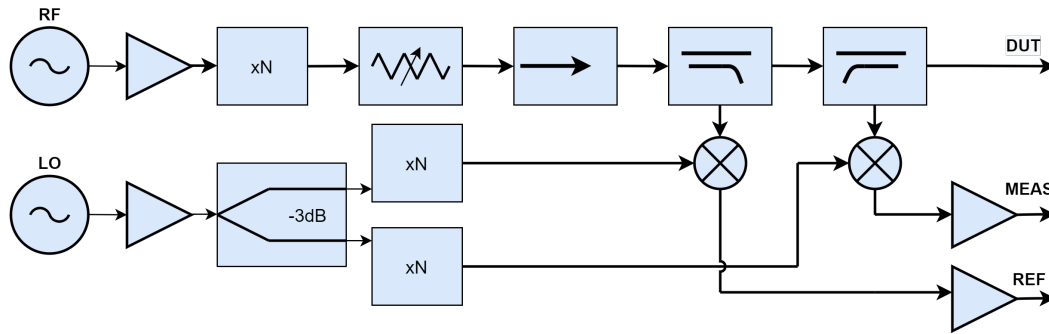


Figure 2.3: Schematical representation of the frequency extension module, as presented in [24].

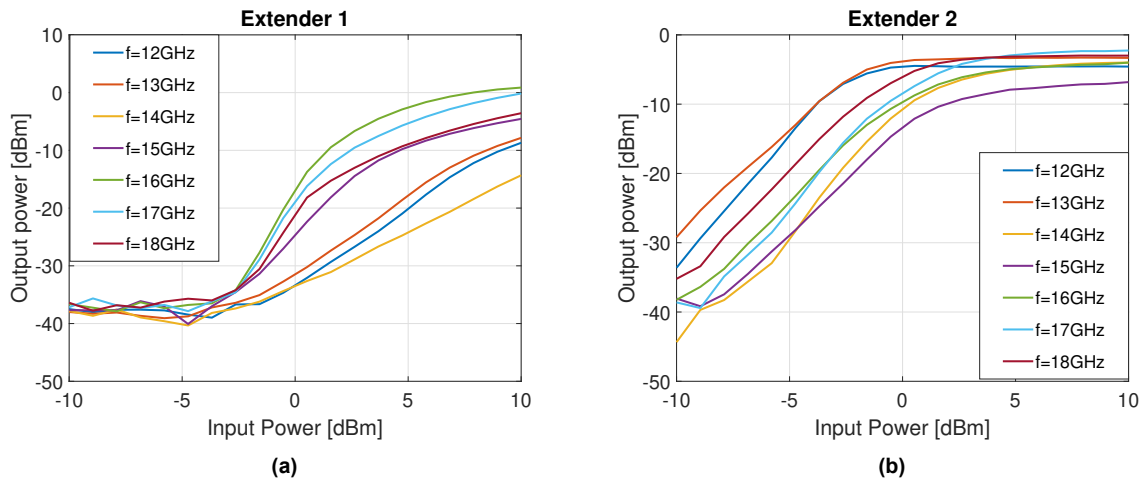


Figure 2.4: Relationship between the extender input power and measured output power. The measurements are repeated for various frequencies for extender 1 (a) and extender 2 (b).

2.1.2. The amount of attenuation was -11dB and -16dB for extenders 1 and 2, respectively.

Another conclusion from Fig. 2.4 is that the input-output power behaviour of the extenders varies greatly with input frequency. The calibration procedure in the next section has been performed at LO frequencies of 15GHz. However, the procedure has to be repeated for several frequencies to cover the full WR-10 band.

2.2. Low frequency measurements

IQ mixer calibration

The first step in the system characterization is to determine the amplitude and phase response of a single vector modulator, for a given V_I and V_Q voltage. With the polar coordinate system, the sweep is performed in circles of increasingly larger input amplitude and uniform phase distribution. This is shown in Fig. 2.2b, where the contours denote the amplitude and the curvatures of equal phase are shown in dashed red lines.

These polar V_I, V_Q sweeps can be used as an input for the IQ modulators. Ideally, the RF amplitude output would be independent of input phase. The output phase should also change uniformly as the input is changed with a fixed step size. In other

words, the output phase should linearly follow the input phase.

To see whether or not this is the case, the RF output of two identical mixers was measured for various V_I and V_Q circles. The used input size was 12 points along A_{IQ} and 41 points along ϕ_{IQ} . The measured S_{21} outputs are shown in Fig. 2.5a for mixer 1 and in Fig. 2.5b for mixer 2. Amplitudes are shown using the colour map and contours, whereas the red dotted lines indicate the curves of constant phase. Several amplitude contours for -7, -9, -15 and -20dBm measured S_{21} output power are shown.

Several observations can be made using the figures. First, the V_I, V_Q location where the output power is minimized is not located at the point $V_I = V_Q = 0V$, as would be expected, but at a position slightly offset from the origin. This offset is due to LO power leaking through the IQ mixer. Finding the location of the leakage minimization point will be important for later analysis. The next observation is that the phase lines are no longer straight but rather curved, indicating that the phase did not change with a fixed amount as the input was uniformly changed. A final observation is that the amplitude contours are no longer circular, suggesting the amplitudes have become distorted.

These non-idealities can be calibrated out via a pre-stored table containing the raw measured outputs for all IQ-values. This way, it maps the V_I, V_Q inputs to the measured outputs. This table then provides a translation between desired output and required V_I and V_Q input voltages. In practice, the contour with the largest common amplitude of all mixer outputs will be chosen to maximize dynamic range. Based on Fig. 2.5a and Fig. 2.5b, -9dBm was selected.

Finally, the phase can be linearized by comparing the input phase to the measured output phase. The phases have been normalized and their absolute value is unknown. The concept is shown in Fig. 2.6a, where the phase distorted output is contrasted to the ideal linear output. The lookup table is able to translate the desired phase output to the required V_I, V_Q input. This calibration process is repeated for all involved mixers, in this simplified case 2. After this calibration process, the amplitude and phase of the IQ mixers is controllable. However, to steer the scanning lens phased array, knowledge of the relative phases between the antenna elements is required. In the next section, this relative phase is investigated.

Relative phase

The calibration scheme proposed by Visweswaran et al. [21] is used to find the relative phase between the IQ mixers. A single IQ mixer is set as a reference and a mixer under test is assigned iteratively. To find the relative phase, the reference mixer is fixed in output power and phase. Then, the mixer under test is set to the same output power, and its input phase is swept from $0 \leq \phi < 2\pi$. The two outputs are combined using a power combiner, this scheme is illustrated in Fig. 2.7. This amounts to vector addition in the complex domain, shown in Fig. 2.8a. Adding two equi-amplitude vectors together will result in output cancellation when their relative phase is exactly 180° . In mathematical terms, this is written as

$$A_1 e^{j\phi_1} + A_2 e^{j\phi_2} = 0. \quad (2.1)$$

Given that A_1 and A_2 are equal, this holds when $\phi_2 = \phi_1 + \pi + k \cdot 2\pi$. The setup that achieves this is shown in Fig. 2.6b. This cancellation of measured output power is

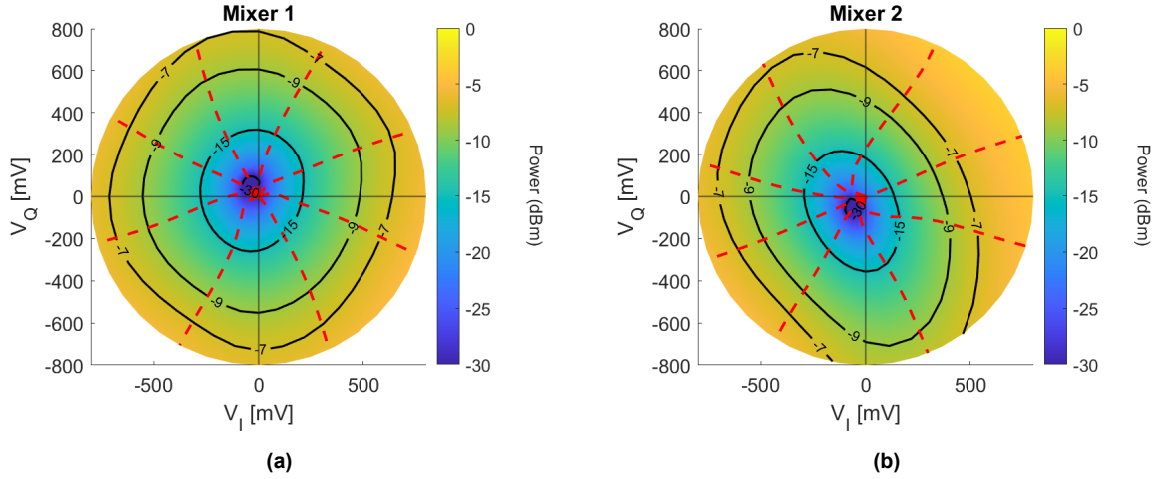


Figure 2.5: 2D overview of the S_{21} outputs for mixer 1 (a) and mixer 2 (b). The color map and contours correspond to the obtained output power and show the cancellation point. The S_{21} phase is shown in red dotted lines

shown in Fig. 2.8b, where the measured output power (normalized by -9dBm) decays to -40dBm as the relative phase approaches 180° . Having identified the cancellation point, other relative phases are obtained using the linearized phase measurements from Fig. 2.6a.

2.2.1. Time drifts of the IQ mixers

We have characterized the drift of the established cancellation point over time in order to investigate the stability of the proposed setups. The S_{21} is measured as it evolves over time, and the amplitude and phase drifts of each individual mixer are extracted. The time tracking is done using a fixed V_I, V_Q input coordinate for each mixer, corresponding to -9dBm of S_{21} magnitude. The mixer under test is evaluated whilst the other is set at the LO leakage minimization point, where its output is minimized. This interleaving is performed over a time span of 24 hours.

The amplitudes $|S_{21}|$ of the individual mixers 1 and 2 are shown in Fig. 2.9a as a function of time. The $|S_{21}|$ drifts away from the original -9dBm value: Mixer 1 shifts to -8.96dBm , whereas mixer 2 has a maximum at -8.95dBm . This asymmetry in amplitude decreases the depth of the cancellation point. However, it does not affect the relative phase as shown by the equation

$$(A_1 + \epsilon)e^{j\phi_1} + A_2e^{j\phi_2} = 0.$$

Here, ϵ represents the (small) amplitude error. The function is still minimized at $\phi_2 = \phi_1 + \pi + k \cdot 2\pi$.

Fig. 2.9b shows the measured phase, $\angle S_{21}$, drift over time. The phase is normalized to time $t = 0$, shown using the blue curves on the left axis. The S_{21} phases drift from 0° to -5° in 24 hours. However, it is the relative phase drift of both mixers that is of interest, shown in red on the right axis. It is observed that the trend of the $\angle S_{21}$ is comparable for mixers 1 and 2, such that the relative phase shift between the mixers is at most 0.6 degrees in a 24h time span. The effect of this relative phase error will be discussed later in Chapter 4.

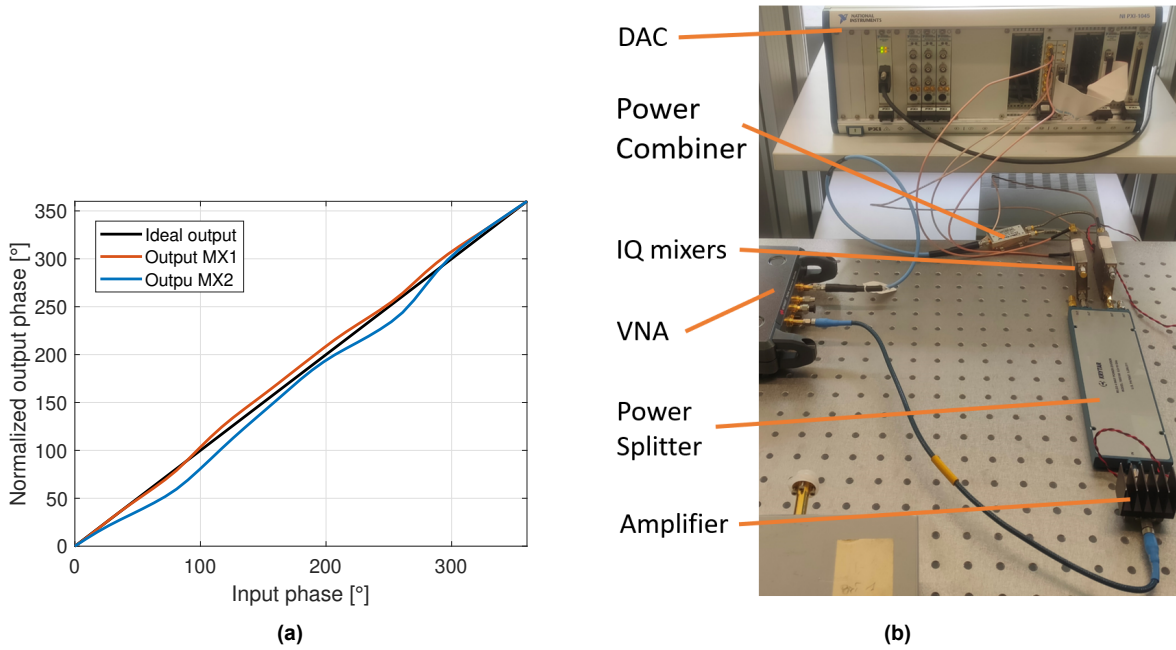


Figure 2.6: (a) Distorted phase output as a function of input phase. (b) Setup for achieving the low frequency cancellation point.

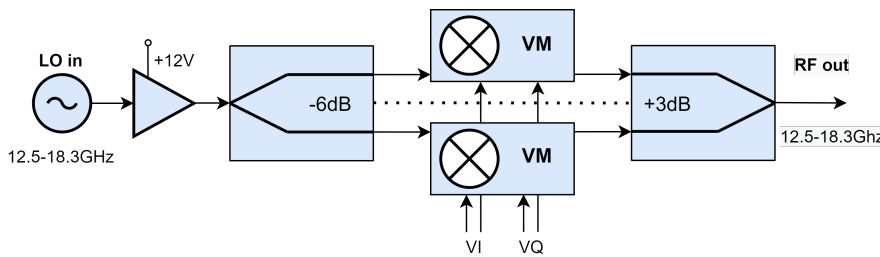


Figure 2.7: Low frequency cancellation scheme, as presented in [21].

2.3. High-frequency measurements

Setup

After investigating the performance at low frequencies, the next step is to turn towards the high-frequency WR-10 domain. The setup is shown in Fig. 2.10. The same architecture is used as in Fig. 2.7, but now the outputs of the two extenders (WR-10 flanges) are combined using a Magic-Tee connected to a matched load. Then, a harmonic mixer is used to down-convert the WR-10 output signals back to the 12-18GHz region, which can be measured using a Spectrum Analyser (SA). The SA, a Rohde & Schwartz FSUP, was used because it was capable of providing enough LO power for the harmonic mixer. The assembled system is shown in Fig. 2.11.

Having properly connected the extenders, the next step was to obtain the extender output power as a function of the V_I and V_Q control voltages. The LO was set to 15GHz. The results, measured with the SA at 90GHz, are shown in Fig. 2.12a for extender 1 and Fig. 2.12b for extender 2. The contours indicate the V_I and V_Q coordinates providing equal output power. The greatest common amplitude contour is chosen to maximize the dynamic range, -20dBm. This time, however, there is no

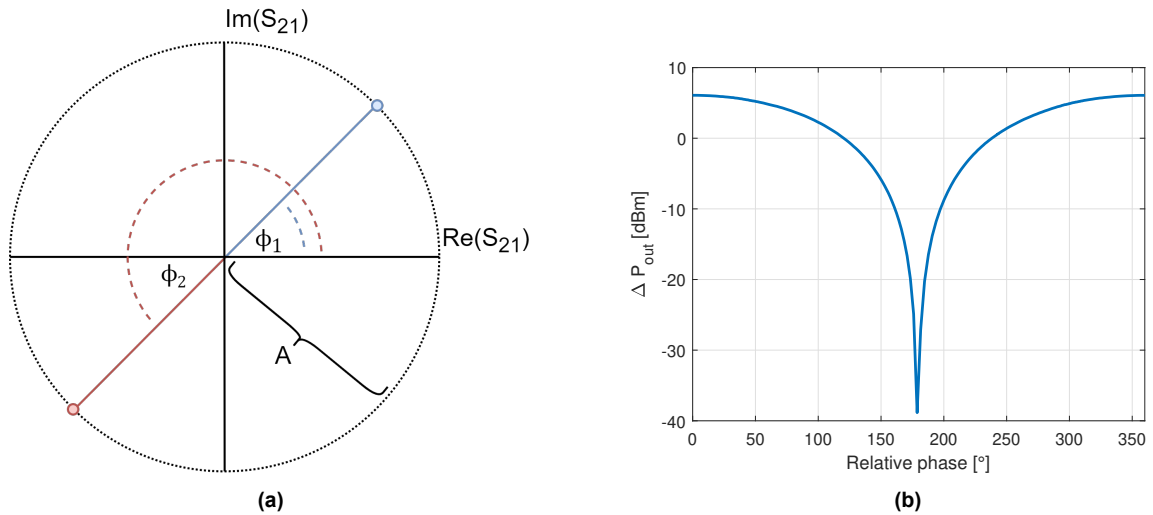


Figure 2.8: (a) Vector cancellation of two vectors with amplitude A and phase ϕ_1 and $\phi_2 = \phi_1 + \pi$. (b) Measured output power as a function of the input phase after combination of the mixer outputs.

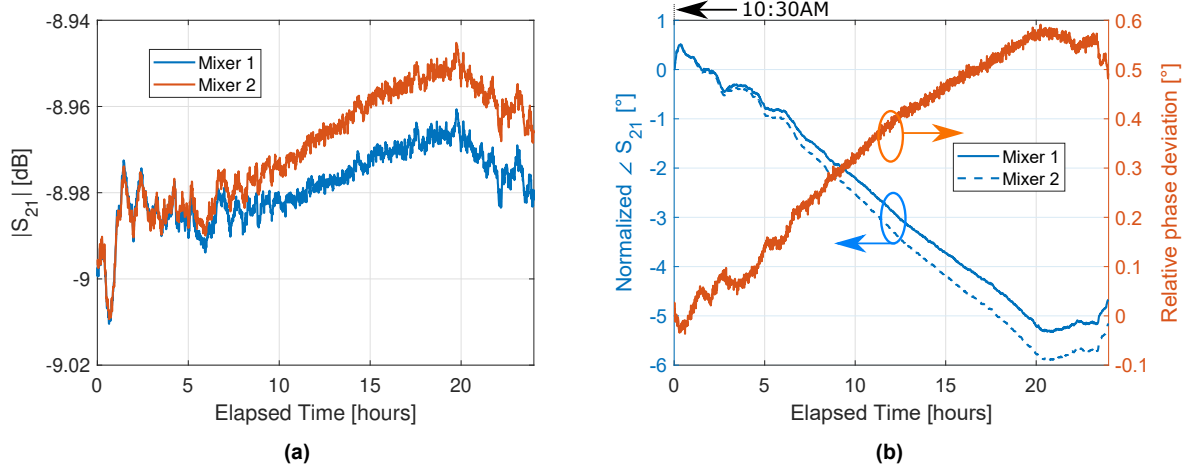


Figure 2.9: Amplitude (a) and phase (b) drifts over a time span of 24 hours using the setup shown in Fig. 2.6b. (b) includes the S_{21} for both mixers in blue, as well as the relative phase drift in red.

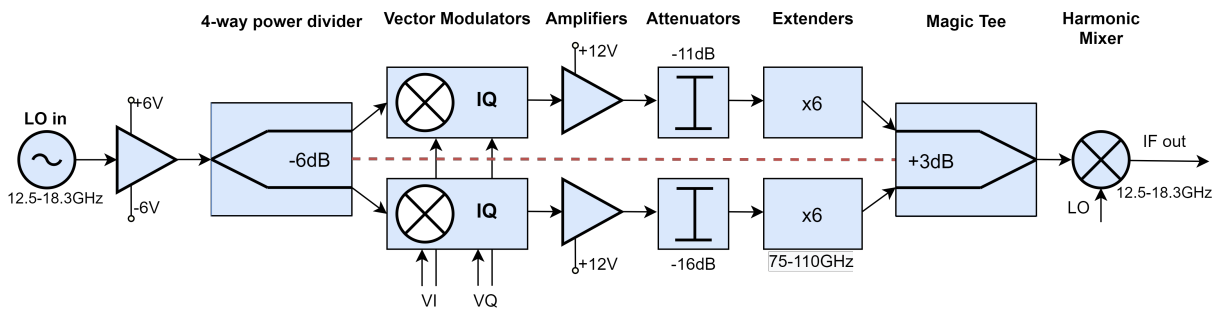


Figure 2.10: High-frequency cancellation scheme.

phase information due to the use of the spectrum analyser to measure power. Another key difference is that the cancellation point has turned into a cancellation disk, a result of the increased input power sensitivity of the extenders at low input powers

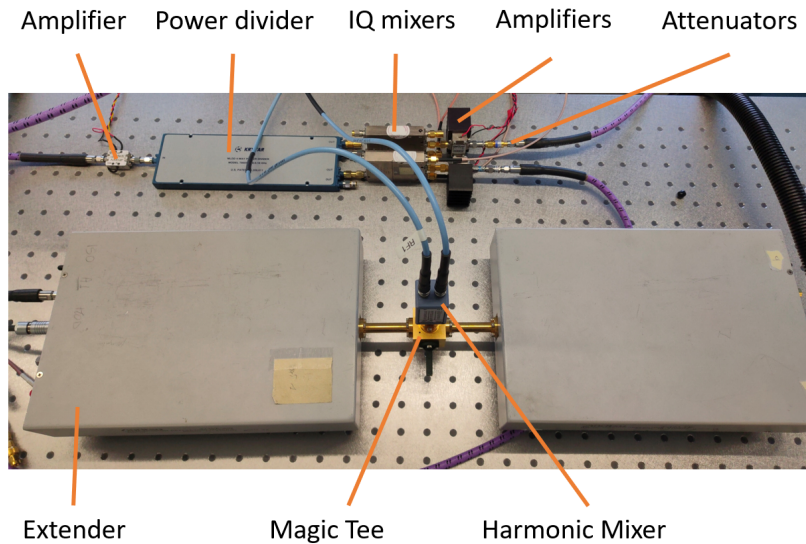


Figure 2.11: High frequency cancellation setup. The two extender outputs are combined at the Magic-Tee output, and subsequently down converted with the harmonic mixer for power measurement.

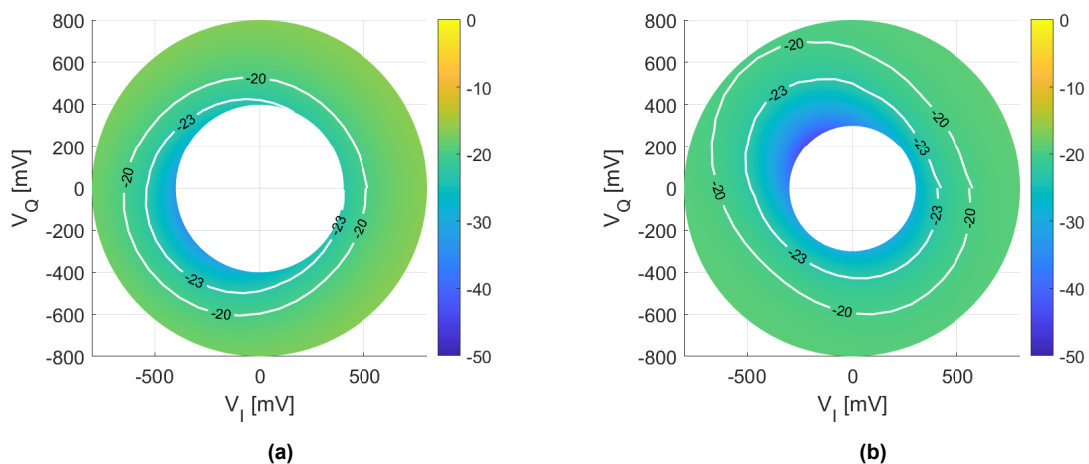


Figure 2.12: Extender output power [dBm] versus V_I and V_Q voltages for extender 1 (a) and extender 2 (b). Contours indicate the bias voltage combinations providing equal output power.

(Fig. 2.4a and Fig. 2.4b).

2.3.1. Relative phases

Knowing the V_I, V_Q voltages corresponding to -20dBm , the relative phase between two extender outputs can be established. This is again achieved using the cancellation point. To understand the cancellation point after frequency multiplication, consider Fig. 2.13. The left hand side shows (mathematically) the 2D cancellation point of the low frequency system. The x- and y-axes represent the variable $V_{I,1}$ and $V_{Q,1}$ of one mixer, the other mixer being fixed at a certain $V_{I,2}, V_{Q,2}$. A single cancellation point is identified, shown in red. After multiplication by factor N , a mixer rotation from $\phi = 0$ to 2π will rotate the extender output from 0 to $2 \cdot N\pi$. The output cancellation condition is denoted analytically by

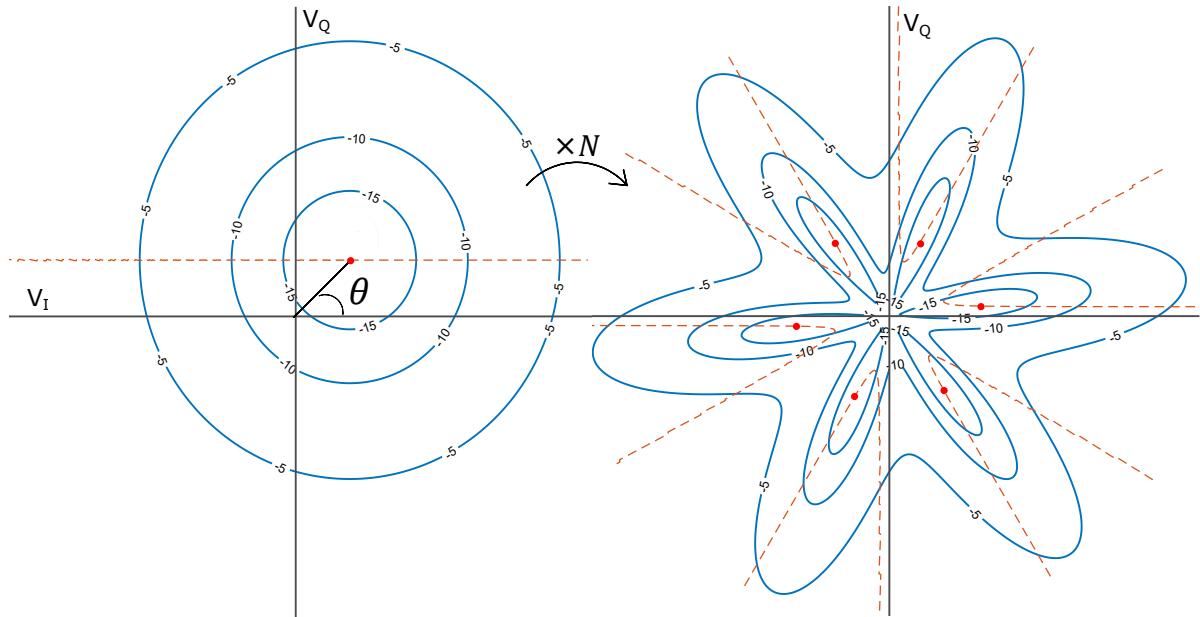


Figure 2.13: In this figure, one mixer is set as a reference (at $\theta + \pi$), the other is controlled by V_I and V_Q . The figure then shows the output amplitude contour plot as a function of input V_I, V_Q before (left) and after (right) multiplication by $N = 6$, showing its effects on the cancellation point. Red dashed lines indicate the 0° and 180° curves of phase.

$$A_1 e^{jN\phi_1} + A_2 e^{jN\phi_2} = 0. \quad (2.2)$$

Again considering $A_1 = A_2$, the condition holds for $\phi_2 = \phi_1 + \frac{\pi}{N} + k \cdot \frac{2\pi}{N}$. This is illustrated on the right of Fig. 2.13 using $N = 6$. A total of six cancellation points are observed as the mixer under test is rotated from $\phi = 0$ to 2π . In red dashed lines are the $0, 180^\circ$ phase curves, indicating that indeed the phase crosses this line six times more often.

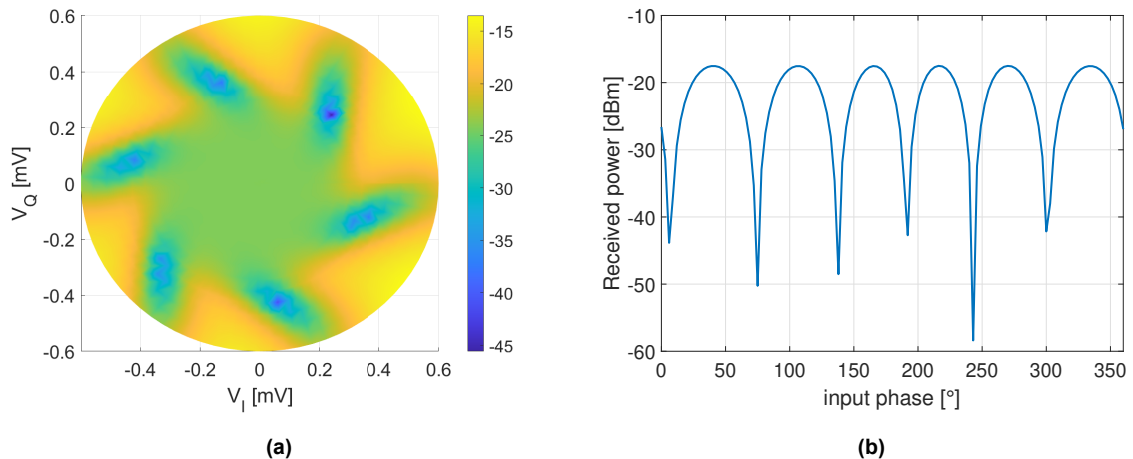


Figure 2.14: Cancellation sequence results in 2D [dBm] (a) and 1D (b).

We now turn again to measuring the cancellation point. Fig. 2.14a shows the measured cancellation points in 2D, where one extender has been fixed and the other has been swept over V_I, V_Q in polar form. Sweeping the V_I, V_Q coordinates that cor-

responded to -20dBm , the 1D results of Fig. 2.14b were obtained. In both figures, the six cancellation points are clearly visible. To obtain the relative phase, only one of these cancellation points has to be located. This limits the search area from 0 to $360/N$ degrees.

2.3.2. Time drifts of the high-frequency setup

Since a time drift of the low-frequency setup has been established in Section 2.2.1, a time drift in the high-frequency setup can also be expected. We have therefore characterized the time-dependence of the cancellation point in the high-frequency setup by recording the output over four hours, shown in Fig. 2.15a. The cancellation point coordinates V_I and V_Q are fixed, and output power is evaluated over a time of four hours. Clearly, long term drifts cause the output power to shift from $\approx -65\text{dBm}$ towards a more or less steady state of $\approx -47\text{dBm}$ after three hours. These drifts are caused by both amplitude and phase errors in each of the extender paths. Both will be investigated separately in the following sections.

The amplitude drifts can be found with a similar method as Fig. 2.9a, where one extender is under test and the other is at the output cancellation point. The results are shown in Fig. 2.15b for a duration of 10.5 hours. The amplitude drift varies between -23.2dBm to -22.4dBm . This range of 0.8dB is greater than the low frequency $|S_{21}|$ amplitude variation of around 0.05dBm . However, the maximum relative difference in amplitude drift between the two extender outputs occurs at time $t=0$ and is around 0.3dB .

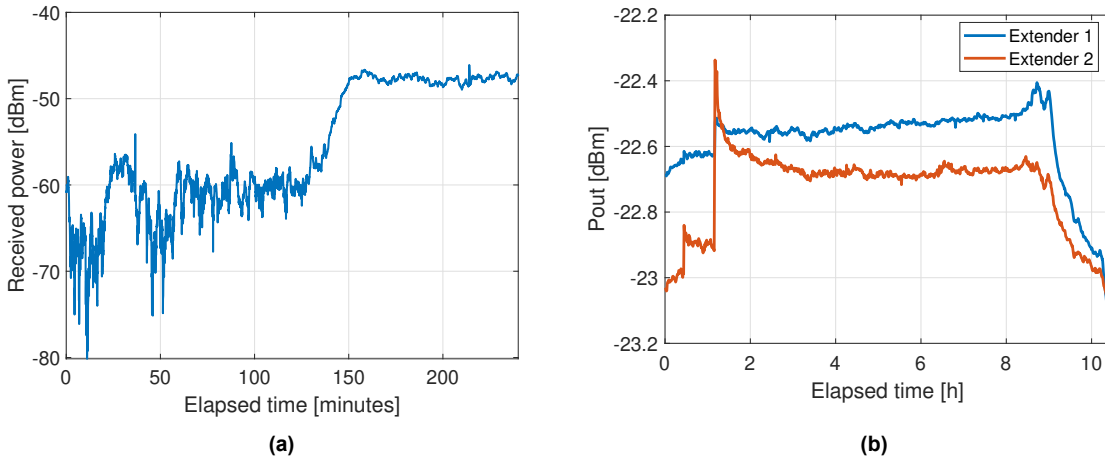


Figure 2.15: Extender output power drift over time for the cancellation point (a) and the interleaved output powers of two separate extender (b).

In order to track the relative phase shift between the two extender outputs over time, the cancellation point has to be tracked. For this purpose, a two-dimensional iterative Golden Section Search (GSS) was used. This method is based on the work in [25], extended to polar coordinates. It allows the determination of the V_I and V_Q voltages of the cancellation point over time. In short, the GSS finds the input voltages V_I' and V_Q' internal to a bounded polar region a_1 , a_2 , b_1 , b_2 (see Fig. 2.16), that minimize the output power. Similar to Section 2.2, one mixer is set as a reference whereas the other mixer is GSS swept for V_I' and V_Q' . The input phase is then derived using

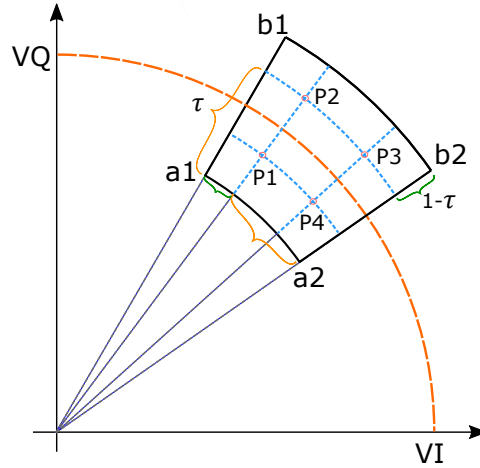


Figure 2.16: Schematic for the 2D golden section search used to find the cancellation point.

$\phi'_i = \tan^{-1}(V'_Q/V'_I)$. Note that this is the input phase before extender multiplication by factor 6.

The GSS algorithm was applied to maintain the cancellation point in the high-frequency setup of Fig. 2.10. The measurement results, taken over a time of 24 hours, are shown in Fig. 2.17. The GSS is usually applied to static cases with no time evolution. However, a single GSS cycle (14 iterations) takes around 80 seconds to complete. It is therefore important that the underlying function that the GSS aims to minimize is not significantly changed during this time. The upper plot of Fig. 2.17 therefore serves as a verification that the iterative method indeed is capable of finding the cancellation point with reasonable accuracy. Remembering Fig. 2.14b, the lower the measured output power, the more accurate will be required input phase.

Within the 24 hour run, the cancellation point input phase seems to be limited to within $\pm 0.5^\circ$. This value will be used in Chapter 4 for analysing the effects of phase errors on array factors. The required V_I and V_Q voltages that keep the high-frequency setup in the cancellation point are shown in the bottom window of Fig. 2.17. The voltages are within $0.425 \pm 0.1V$ for V_I and $0.212 \pm 0.08V$ for V_Q . Thus, the required adjustment of V_I and V_Q is safely within the operating region of the IQ mixers ($\pm 0.8V$, see Section 2.1.2).

2.4. Discussion

A shortcoming of the chapter was that the high frequency measurements were performed using a spectrum analyzer, that could only measure absolute (spectral) power levels. It was therefore not possible to obtain phase information that could have proven invaluable for phase stability knowledge. Only the relative phase could be obtained using the cancellation point.

Here, we discuss the validity of the method of the tracking of the cancellation point input phase of Fig. 2.17. Here, the relative input phase, i.e. the phase given by input voltages V_I and V_Q , was linearly linked to the relative 90GHz output phase. However, the low frequency input-output phase relation was shown in Fig. 2.6a, indicating that the relationship was slightly non-linear.

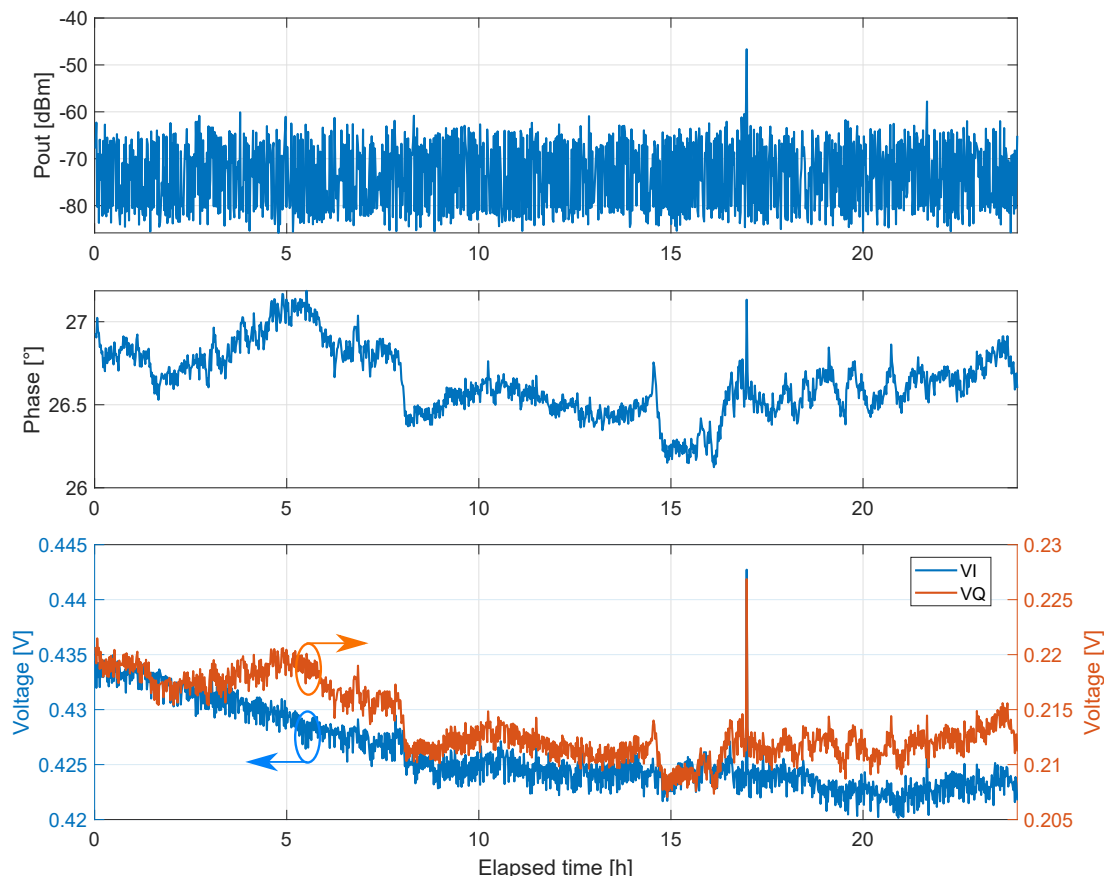


Figure 2.17: Drift of the cancellation point over time, measured using the iterative scheme of Fig. 2.16. The top window provides a measure of the depth of the cancellation point. The middle subplot shows the input cancellation point phase shifting over time, indicating a deviation of $\pm 0.5^\circ$. Finally, the bottom window shows the input V_I and V_Q required to arrive at the cancellation point over time.

Nevertheless, for the high frequency setup, mixer one was used as a reference, mixer 2 was fixed. The input phase range was swept from 0° to 60° . Fig. 2.6a indicated that the low frequency mixer 1 phase output was near linear to the input phase. This implies that we can directly link the change in input phase to the change in output phase. Whether or not this still holds for the high frequency setup is open for debate. A future study with PNA phase measurements could provide more answers.

Another limitation in this work is that the analysis of this chapter was performed at 90GHz only. This frequency together with the pre-multiplied 15GHz are near the bandwidth centre frequencies of all involved components. Moving to 70GHz or 110GHz, could result in errors exceeding the ones observed at 90GHz. Future work would therefore include the discussed calibration technique at the other frequencies in the WR-10 band.

2.5. Summary

This chapter explained the steps taken to arrive at a high frequency phase steering system. Starting with the low frequency setup, the mixers were calibrated and charac-

terized over time. Then, the extenders were introduced to move to the higher frequencies. Further analysis was performed at 90GHz. The final setup achieved a relative phase stability of $\pm 0.5^\circ$ over a time span of 24h. The amplitude shifted over a range of around 0.8dBm over a time span of 10.5h, with relative amplitude differences between extender outputs of at most 0.3dBm. This stability was quantified using two mixers and two extenders. For the proposed 4×1 array, the same calibration is to be performed for the other two signal paths.

3

Lens antenna based on a corrugated LW feed

In this chapter a novel leaky-wave lens antenna concept is proposed for the scanning lens phased array architecture. Its performance is compared to the current state of the art, represented by the earlier work by Arias Campo et al. [4], where a double-slot 'iris' antenna was implemented. The chapter begins with a brief introduction to the concept of Leaky-wave (LW) feeding antennas and the use of corrugated ground planes in Section 3.1. Subsequently, the performance of such corrugated LW design is analyzed with simulations in Section 3.2. Lastly, a prototype of our antenna with corrugated ground-plane has been fabricated and measured at WR-5 frequencies, validating the design procedure. This is presented in Section 3.3.

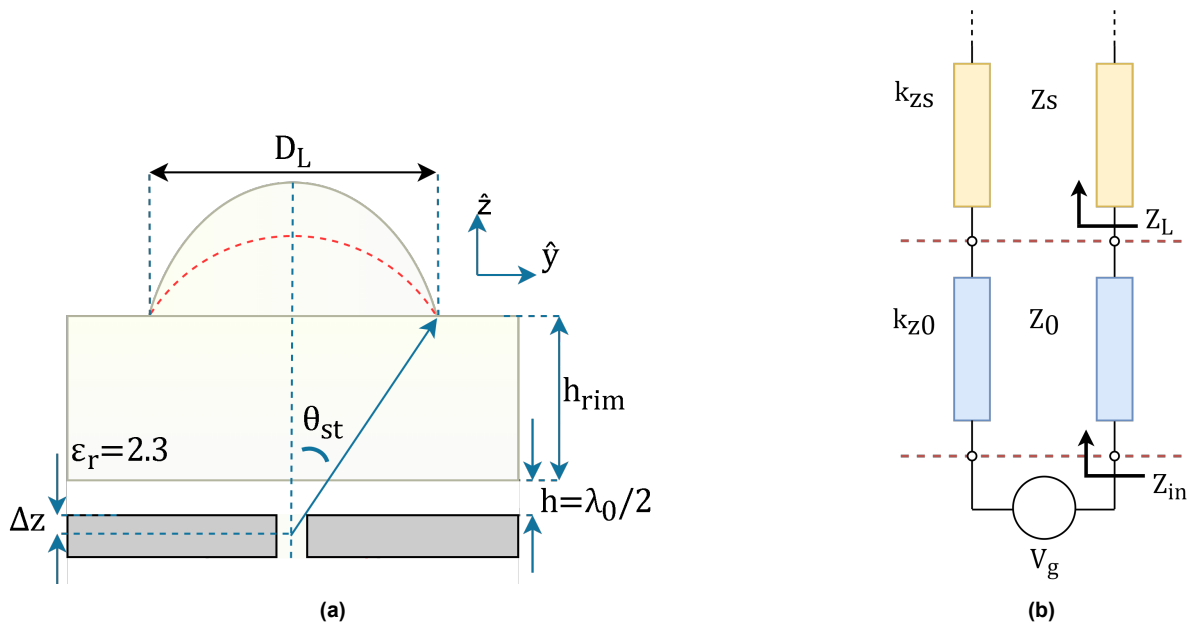


Figure 3.1: (a) Cross-sectional schematic of the LW lens element and (b) transmission line model for the semi-infinite dielectric lens above the air gap and ground plane.

3.1. Leaky-wave feed with corrugated ground-plane: Dispersion equation

In order to achieve high aperture efficiency, the primary pattern of the antenna must couple well to the incident GO field. As shown in [4], resonant leaky-wave feeds radiate patterns that achieve this goal. The geometry of the resonant leaky-wave feed is shown in Fig. 3.1a, including the coordinate system that will be used throughout this work. The z-axis is considered to be the 'vertical' direction. The lens block is positioned on top of an air gap with height h . This air gap that is layered between the aluminium waveguide block and the lens material, acts as a Fabry-Pérot Resonance (FPR) cavity. The phase-center of such FPR antenna is shifted by Δz below the ground plane [26]. Such a geometry supports the propagation of leaky-wave modes in the cavity.

The leaky-wave modes can be found by finding the poles of the appropriate dispersion equation that results from the TE or TM transmission line equivalent network. This network is shown in Fig. 3.1b and the resulting dispersion equation is given by

$$D(k_\rho) = Z_s + jZ_0 \tan(k_{z0}h_0) = 0 \quad (3.1)$$

where Z_0 and Z_s are the free space and dielectric impedances, respectively. k_{z0} is the vertical propagation constant in the air gap, given by $k_{z0} = \sqrt{k_0^2 - k_\rho^2}$. This equation can be solved numerically or can be approximated [27]. The poles are complex numbers given by $k_\rho^{LW} = \beta_{LW} - j\alpha_{LW}$. In a resonant leaky-wave antenna, with an air cavity of $\lambda/2$, a pair of nearly-degenerate TM1/TE1 leaky-wave modes and a non-dispersive TM0 mode propagate [28]. For a semi-infinite medium with $\epsilon_r = 2.3$, the leaky-wave poles are shown in Fig. 3.2 as a function of frequency. The leaky-wave pointing angle in the semi-infinite medium is derived according to $\theta_{LW} = \sin^{-1}(\beta_{LW}/k_d)$.

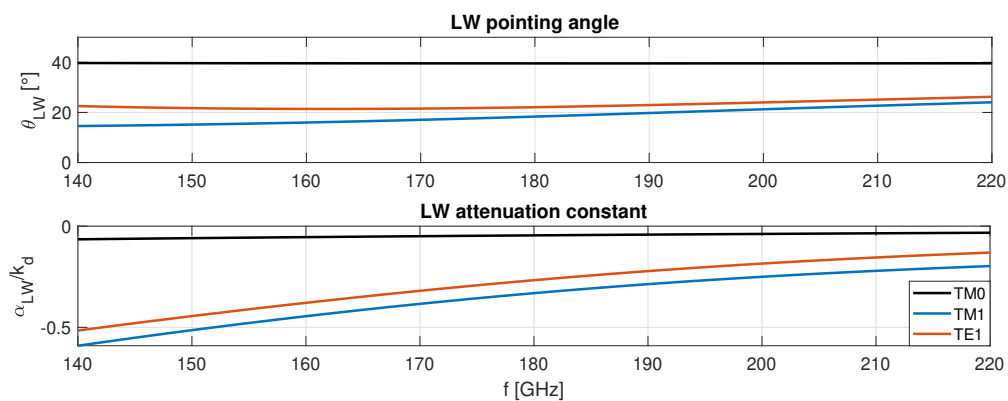


Figure 3.2: Leaky-wave propagation constants as a function of frequency, using numerical solving of the dispersion equation.

The TM1/TE1 modes provide the desired directive beam around broadside in the semi-infinite medium. Furthermore, these two modes possess relatively large α_{LW} leakage constants, spreading their effects over a larger beam width [29]. The TM0 mode, however, is a spurious mode that radiates towards large angles and therefore decreases the aperture efficiency. The mode bolsters a vertical electric E_z field, causing

high cross-polarization in the primary pattern. Therefore, this mode should be suppressed.

The suppression of the TM₀ mode can be achieved by using a double-slot iris [28], [4]. However, the iris is manufactured on a thin metallic sheet, which is one of the most challenging parts of the antenna fabrication process. Furthermore, the cross polarization suppression is limited in the D-plane. For example, the primary patterns of a double-slot iris radiating into $\epsilon_r = 2.3$ are shown in Fig. 3.6. The cross-polarization is above -14dB in the D-plane.

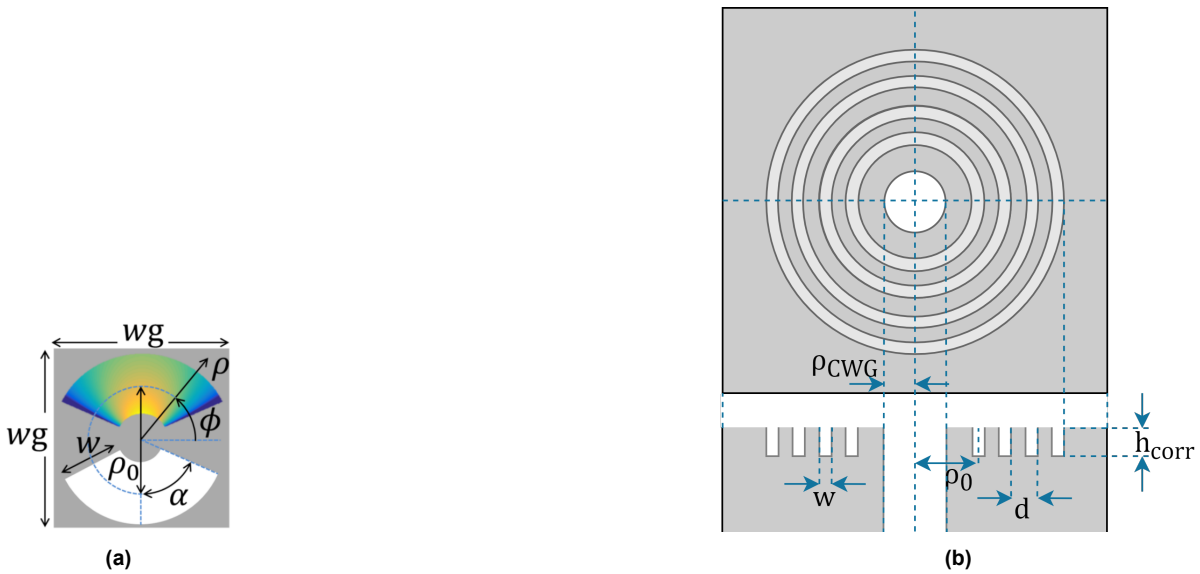


Figure 3.3: (a) Geometry of the double slot iris ([4], Fig. 2b) and (b) the geometry of the corrugated ground plane.

Therefore, we have introduced a new method of TM₀ attenuation which uses annular corrugations in the ground plane [30]. Fig. 3.3b shows an enlarged overview of the corrugated geometry. The corrugations are circularly symmetric around the center of the waveguide, with radius ρ_{CWG} . The corrugations are rectangular in cross section with width w and depth h_{corr} . The corrugations can be repeated N times with period d in between. The optimal geometry was investigated during the internship [19] and summarized in table 3.1.

Table 3.1: Overview of parameters to construct the corrugated geometry.

| Parameter | Value [mm] | Value [λ_0] |
|---------------|------------|-----------------------|
| ρ_0 | 0.795mm | $\lambda_0/2.1$ |
| ρ_{CWG} | 1.145mm | $\lambda_0/1.5$ |
| d | 0.376mm | $\lambda_0/4.4$ |
| h_{corr} | 0.55mm | $\lambda_0/3.0$ |
| w | 0.176mm | $\lambda_0/9.5$ |
| θ_{st} | 36.5° | n.a. |
| Δz | -1.2mm | $-\lambda_0/1.6$ |

To validate the TM₀ suppression achieved by this corrugated leaky-wave antenna (CLWA), the leaky-wave poles were extracted from full-wave simulations. First, a structure without corrugations was simulated to extract the TM₀ pole as a function of frequency. The procedure to extract these poles was explained in more detail in the internship report [19]. This was compared to the leaky-wave poles calculated using the dispersion equation. The result is shown in Fig. 3.4 where we see a good match between the two methods. The leaky-wave pointing angle is a near 40°, the normalized attenuation constant is around -0.05Np/m. Then, a FW simulation of the corrugated structure was performed and the LW propagation constants were extracted from this simulation using the same approach. The LW now points to angles closer to broadside (30°-38°) and has an attenuation constant of a factor 1.5-2.3 higher than the case without corrugations. These results indicate that the corrugations indeed help attenuate the TM₀ mode.

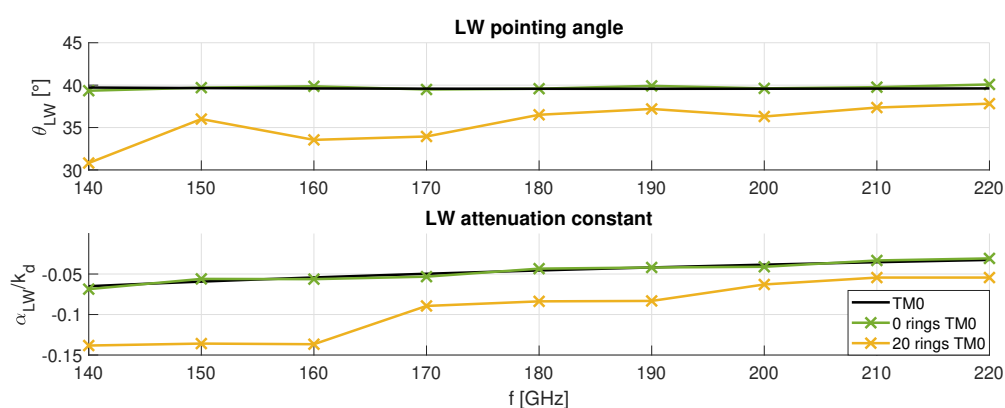


Figure 3.4: Leaky-wave propagation constants as a function of frequency, comparing the TM₀ mode of the open-ended Waveguide with the case of 20 corrugations.

3.2. Leaky-wave feed with corrugated ground-plane: Radiation performance

The corrugated leaky-wave feed is now analyzed together with a plastic lens, using the GO-FO GUI [31] and FW CST 2020 [32] simulations. The semi-infinite model is shown in Fig. 3.5a. The corrugated design will be compared with the double-slot iris, its dimensions provided by Arias Campo et al. [4]. An open-ended waveguide without any corrugations will be used as a final geometry for comparison. These three geometries will be compared based on input reflection coefficient S_{11} , primary patterns, aperture efficiency and, finally, the secondary patterns. All simulations in this section will be performed using Perfect Electric Conductor (PEC) materials and lossless dielectrics ($\tan\delta = 0$).

3.2.1. Input reflection coefficient

The reflections at the input port are captured in the S_{11} parameter. The antenna is considered to be 'well matched' when the condition $S_{11} < -10dB$ is satisfied for a desired frequency. Fig. 3.5b shows this S_{11} , simulated in CST with the semi-infinite

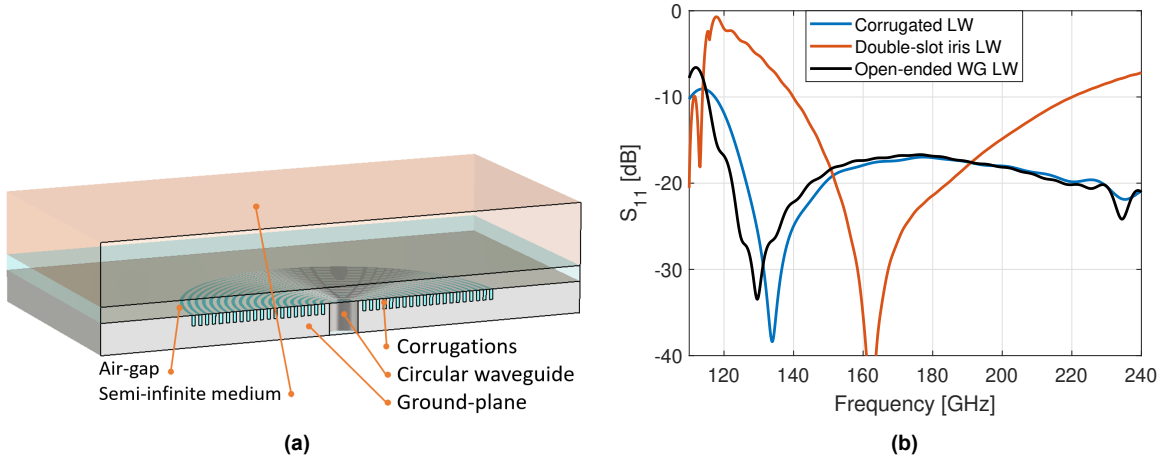


Figure 3.5: (a) FW model using the semi-infinite medium replacing the lens. 20 corrugations were added. (b) The semi-infinite FW simulated S_{11} parameter compared to the double-slot iris and open-ended waveguide. All geometries are excluding any waveguide tapering.

medium case, and indicates that the antenna is matched over the 120-240GHz frequency range. This is roughly comparable to the open-ended WG, implying that the corrugations do not greatly affect the S_{11} . By contrast, the double-slot iris of Arias Campo et al. was matched only over the WR-5 bandwidth, 140-220GHz.

3.2.2. Primary patterns

The patterns radiated by the corrugated LW feed into an infinite medium provide information on how efficiently the lens FO sphere is illuminated. A detailed look on this primary pattern analysis is given in Appendix A. The more these primary patterns resemble the GO fields, shown in Fig. 3.6a, the higher will be the η_{ap} (Eq. A.3) and subsequent antenna gain. The resulting corrugated patterns are shown in 3.6 and compared to the double slot iris. Several conclusions can be drawn on the results. First, the iris has overall larger TM₀ mode influence at $\approx 40^\circ$ compared to the corrugated design, visible especially in the D- and E-plane. Next, the CX-pol is significantly reduced using the corrugations. Its level is now more in agreement with the GO fields. Finally, the patterns have a steeper roll-off at angles $> 40^\circ$, which helps decrease the loss due to η_t and η_{sp} in the vicinity of that region.

3.2.3. Aperture efficiency

The primary patterns were then exported with the far-field approximation in CST and used as an input to the GO-FO GUI of [31] (See Appendix A). The tool is able to convert these primary patterns into the secondary patterns, η_t and η_{st} . These data can be converted to antenna directivity and gain. θ_{st} and Δz are optimized for η_{ap} every time a new primary pattern is generated. The η_{ap} versus frequency is shown in Fig. 3.7a for the three discussed antenna geometries. Overall, the corrugated design has much higher η_{ap} bandwidth than its two counterparts, with $>80\%$ from 120-240GHz.

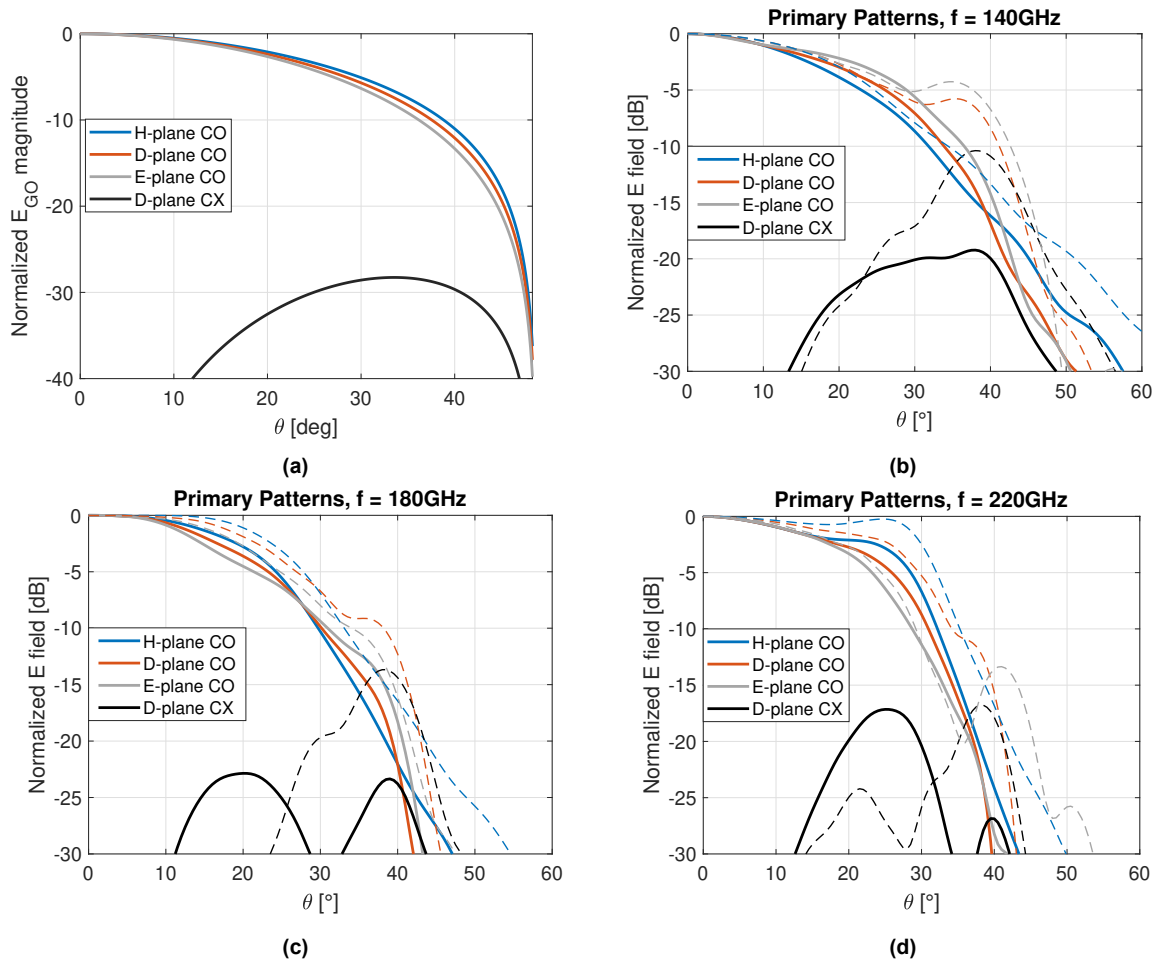


Figure 3.6: GO fields for the lens with $\epsilon_r = 2.3$ (a). Primary patterns for 140GHz (b), 180GHz (c) and 220GHz (d). Solid lines indicate the results with corrugations using the CST model shown in 3.5a. Dashed lines represent the double-slot iris as used in Arias Campo et al. [4].

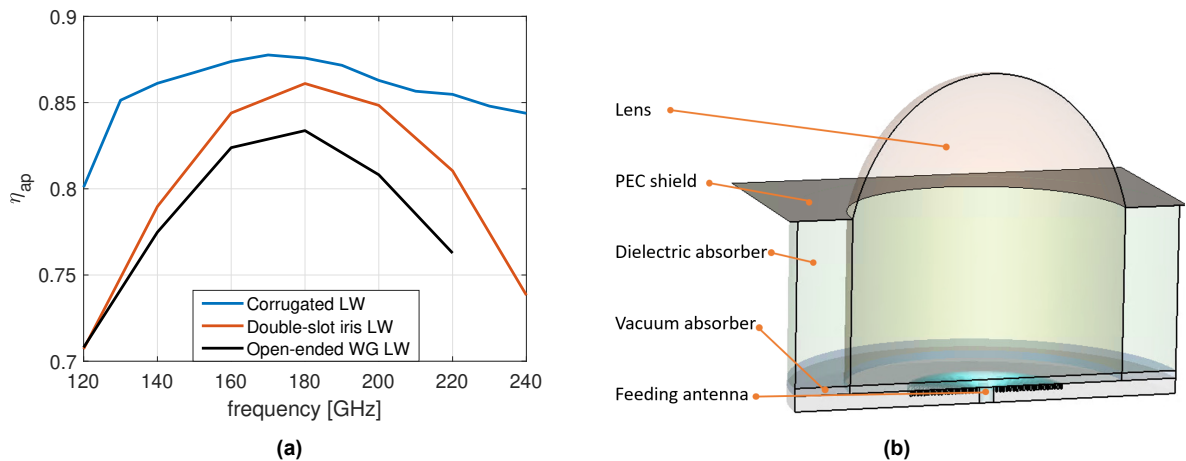


Figure 3.7: (a) Aperture efficiency as a function of frequency for three different geometries: the Corrugated ground-plane LW antenna, the LW Double slot iris from [4] and, finally, the open-ended LW waveguide. (b) The FW single pulse CST model used for comparison to the GO-FO tool.

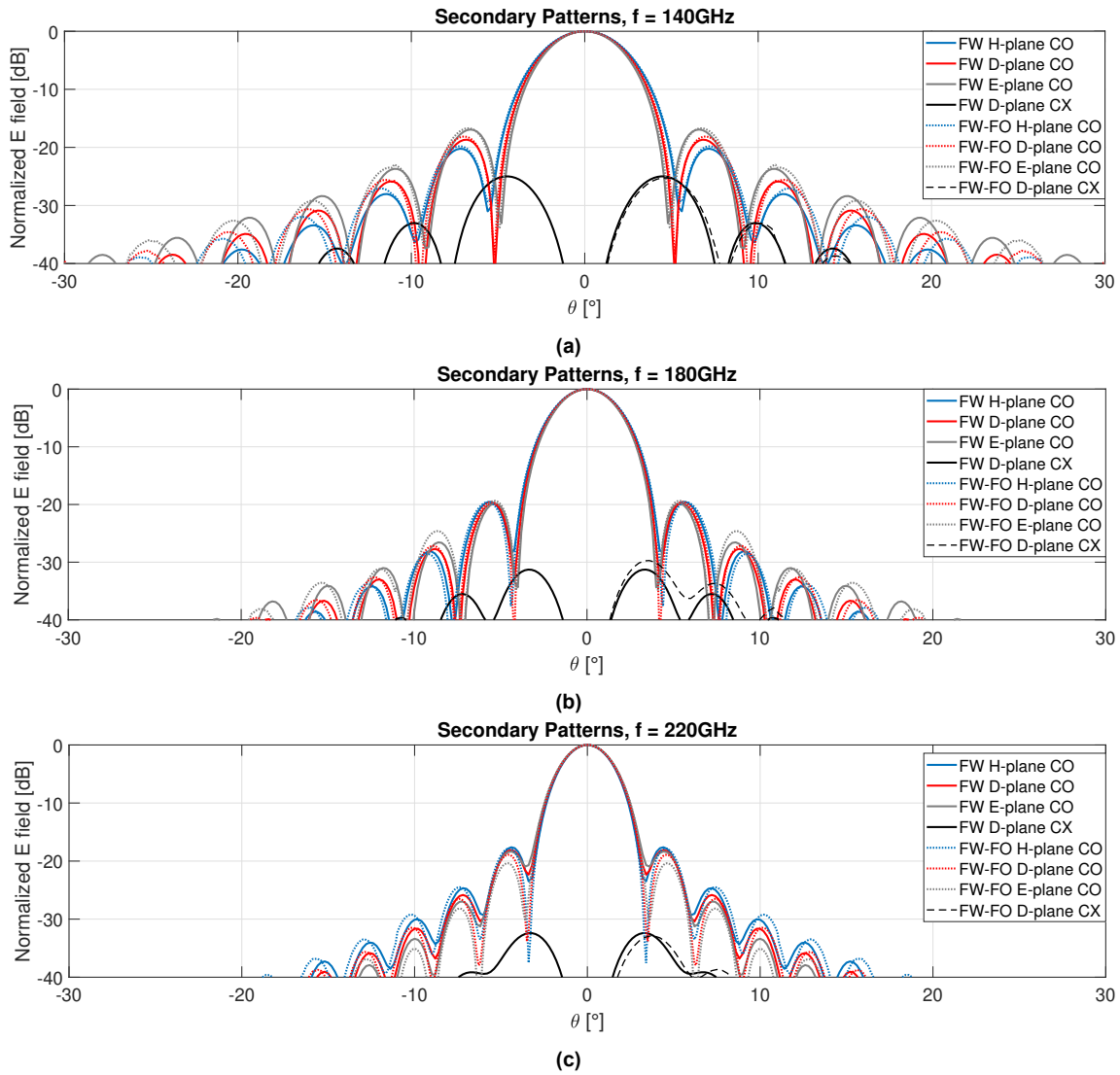


Figure 3.8: Secondary patterns simulated using the GOFO tool [31] (dotted line) and FW simulations (solid line). Three frequencies are presented, 140GHz (a), 180GHz (b) and 220GHz (c).

3.2.4. Secondary Patterns

The GO-FO GUI is able to convert the primary patterns of Fig. 3.6 to the lens secondary patterns. These patterns could then be compared to the FW CST model that includes the lens, shown in Fig. 3.7b. A time domain FW solver was used, using the geometry of Table 3.1. A PEC shield with absorbing materials is introduced to prevent multiple reflections from interfering with the resulting patterns. The simulation time was also stopped after a single pulse ($\approx 0.3\text{ns}$), again to avoid multiple reflections. The secondary patterns can then be compared to the ones obtained from the GO-FO tool, this is shown in Fig. 3.8 for three frequencies in the WR-5 band. FW simulations and the GO-FO tool show excellent agreement. Especially at 180GHz, there is a high degree of symmetry along ϕ visible. GO-FO CX-pol analysis is limited to positive θ only. The secondary pattern CX-pol as a function of frequency, derived from the FW simulations, is shown in Fig. 3.9a. It is compared to the double-slot iris, indicating that the CX-pol in the secondary pattern is significantly reduced by up to

10dB by implementing the corrugations.

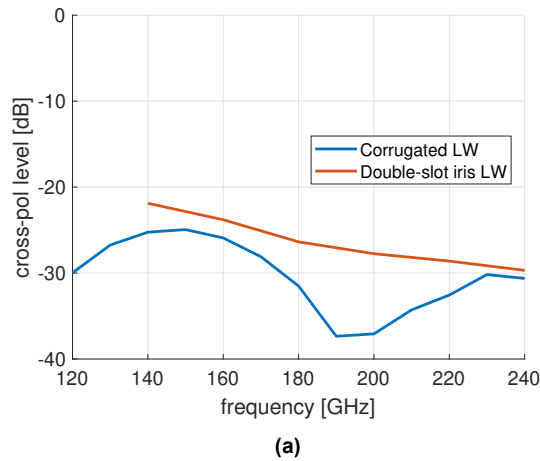


Figure 3.9: Simulated CX-pol magnitude versus frequency, comparing the double slot iris to the corrugated ground-plane leaky-wave antenna.

3.3. WR-5 Prototype

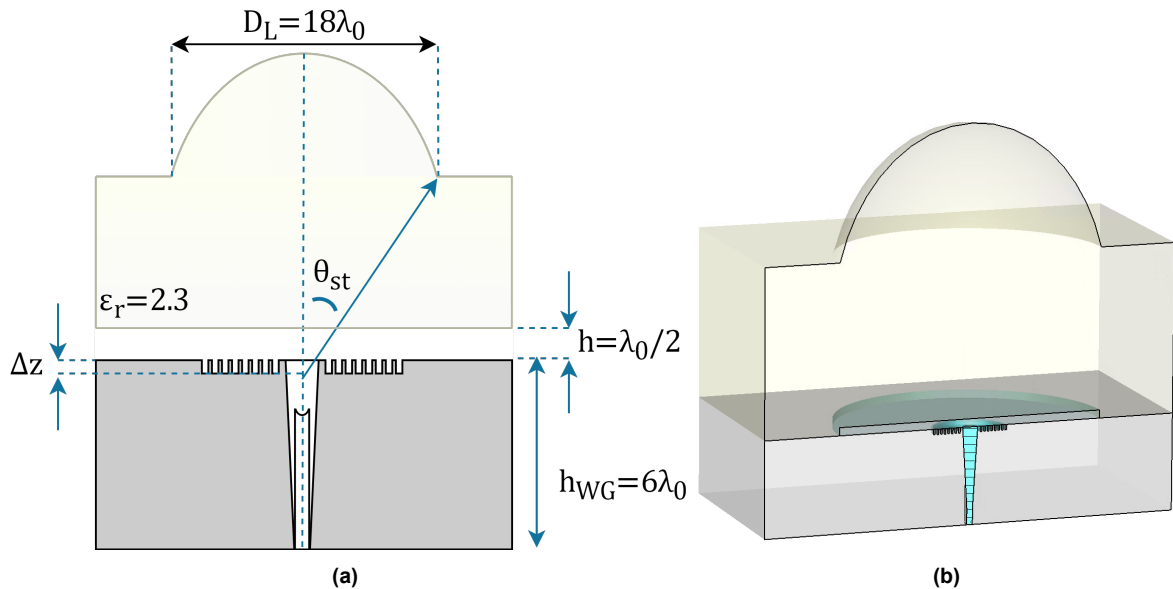


Figure 3.10: Cross-sectional schematic of the LW lens element With corrugations and $D_L = 18\lambda_0$ (a) and corresponding cross-sectional view of the CST model (b).

Based on the performance of the CLWA in Section 3.2, two identical antennas were fabricated by DEMO at the TU Delft. The centre frequency f_c lies at 180GHz ($\lambda_0 = 1.67mm$). This prototype features a $D_L = 18\lambda_0$ lens with $\theta_{st} = 36.5^\circ$. The number of corrugations was set to 8. The design has been scaled up by a factor of 12/11 in order to have higher performance at low frequencies. This allowed the design, based on simulations of Fig. 3.7a, to also have $> 80\% \eta_{ap}$ at 110GHz. This way, both the WR-5 and the WR-7 could be covered in a single design. The prototype includes

a waveguide tapered transition to the WR-5 extender band (140-220GHz). One of the prototypes is shown in Fig. 3.12.

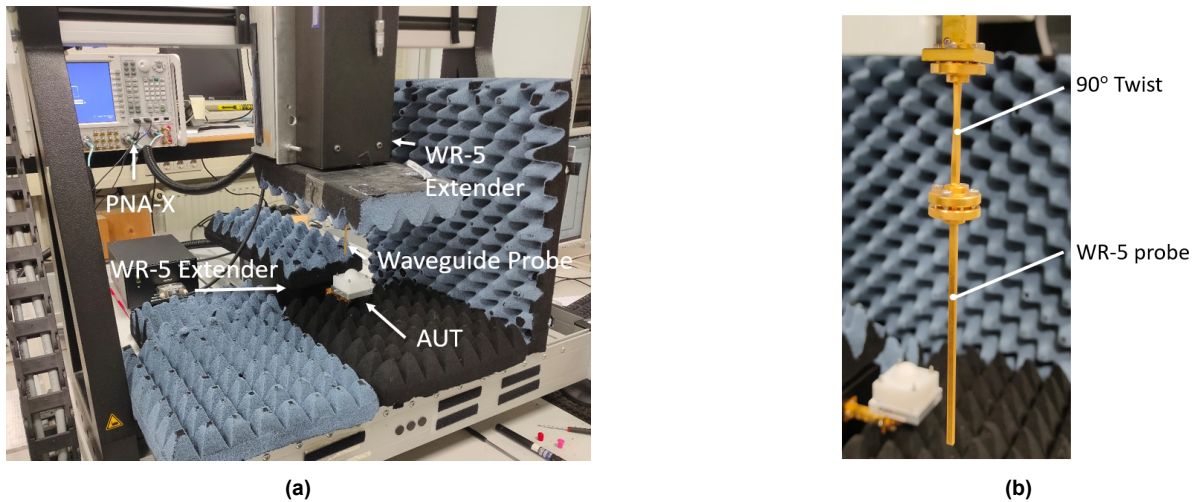


Figure 3.11: (a) Near-field measurement setup and (b) WR-5 probe attached to the 90° twist to measure the CX-pol.

The prototype has a $47 \times 47\text{mm}$ HDPE lens block and is placed on a $53 \times 53\text{mm}$ aluminium ground plane. This ground plane includes the corrugations along the circular waveguide and multiple sets of holes for the alignment pins (Fig. 3.12b). These alignment pins, located along both the E- and H-plane, are displaced by a distance $\Delta x = \Delta y = 1.67\text{mm}$. This results in a discrete scanning capability towards broadside, 5° , 10° and 15° along both planes. The prototype has a $h_{WG} = 13.76\text{mm}$ long tapering from the WR-5 rectangular waveguide that terminates in a circular waveguide with radius $\rho_{CWG} = 0.87\text{mm}$.

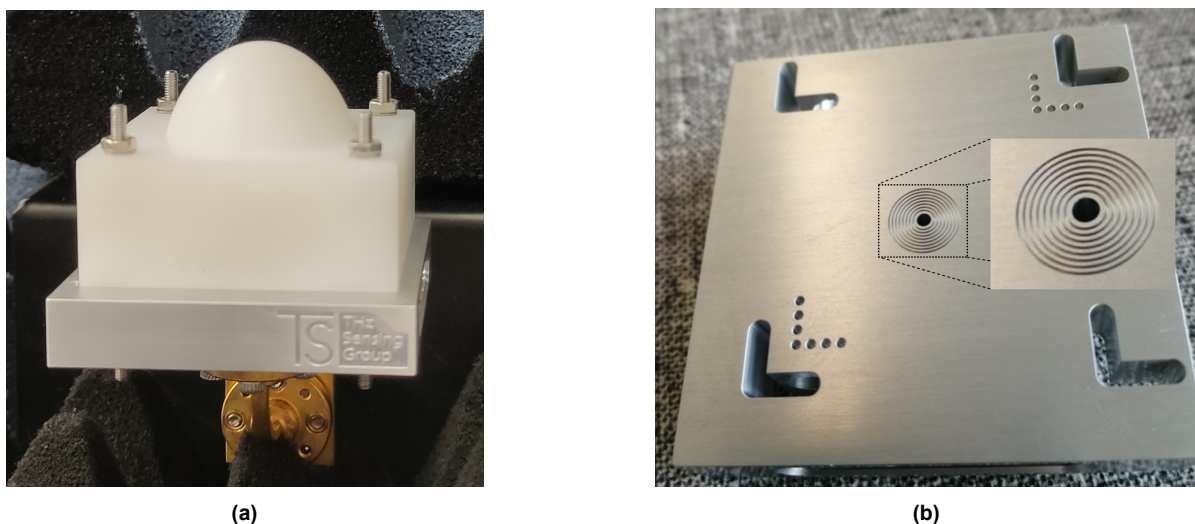


Figure 3.12: Fabricated WR5 prototype including the $D_L = 20\lambda_0$ lens (a) and corrugated aluminium ground plane (b).

3.3.1. Simulated and measured performance

The following section compares the FW simulation results with the results obtained by measurements on the WR-5 prototypes. The simulations were performed in CST using the time-domain solver and includes multiple reflections at the air-lens interface. The FW model is shown in cross-sectional view in Fig. 3.10b. Dielectric losses are approximated using $\tan\delta = 0.00033$, in line with [4]. For the HDPE material. $\sigma_{alu} = 4e5$ S/m was chosen for the aluminium conductivity (was $3.6e5$ S/m in [4]), taking into account the surface roughness.

Input reflection coefficient measurements

Input reflection coefficients were measured first, using the setup of Fig. 3.13a. Two VDI WR5.1 VNA extenders were used that extend the 12-18GHz PNA output to the high frequency WR-5 band. The PNA-X supplies the two extenders both their respective LO and RF power of +10dBm. It also analyzed the 2-port S -parameter matrix containing S_{11} , S_{21} , S_{22} and S_{12} . Further components include the standard WR-5 components and of course the two Antennas Under Test (AUT). The measurement setup is S -parameter calibrated before use. This S -parameter calibration was performed up to the extension module output plane (see Fig. 3.13a red dashed line). The two AUTs were then connected each to an individual extender, and directed towards free-space to minimize ambient reflections. S -parameter measurements were performed with a total of 6.000 frequency points, ranging from 140GHz to 220GHz.

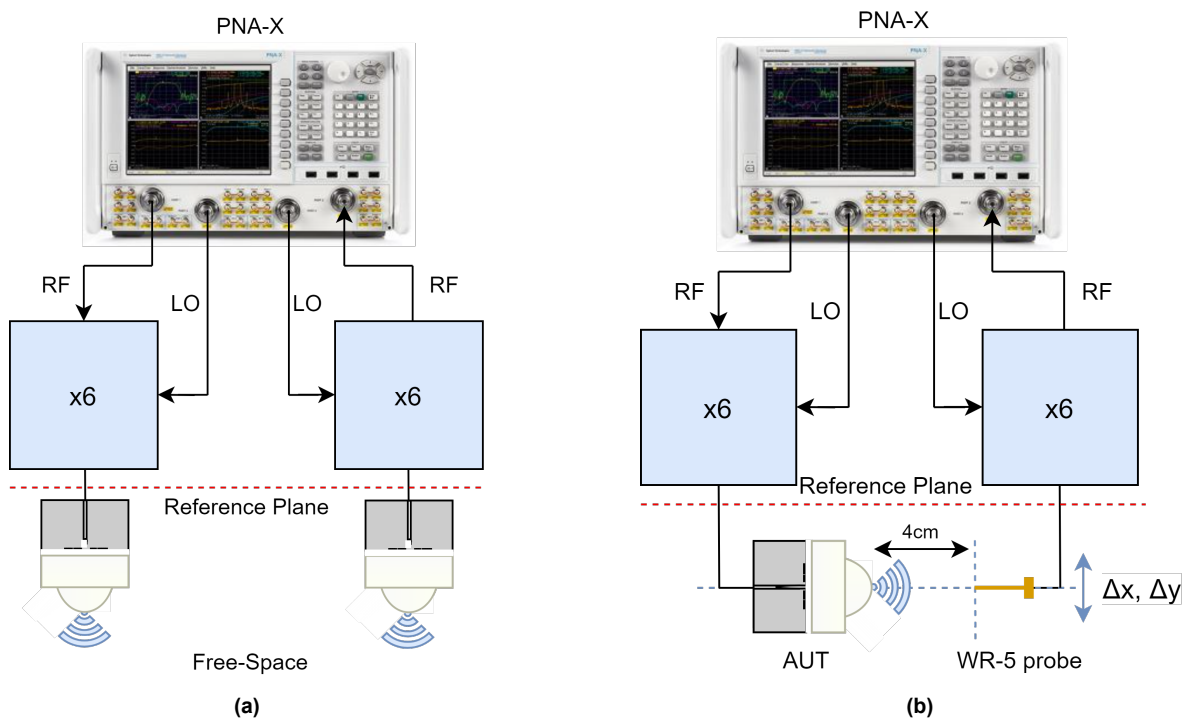


Figure 3.13: S_{11} measurement scheme (a) and near-field measurement scheme (b). The S -parameter calibration reference planes have been included in both figures.

The measurement results are shown in Fig. 3.14. The S_{22} shows very good agreement with FW simulations. However, there is a discrepancy between the measured and simulated S_{11} for one of the two antennas at the beginning of the band. This is

possibly an AUT fabrication problem, as the mismatch persisted even after changing the setup. Unfortunately, this antenna rather than the S_{22} one has been used for the rest of the measurements. However, the error appears to be in a small bandwidth region around 140GHz. The rest of the bandwidth shows good agreement with FW simulations with good matching.

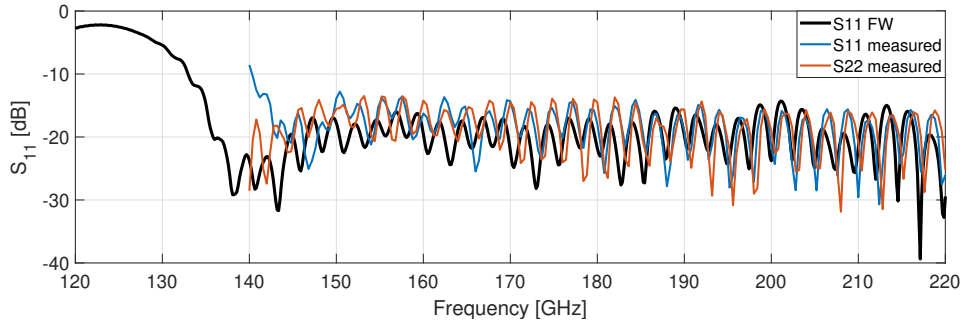


Figure 3.14: S_{11} measurement results (blue and orange) compared to the FW results (black). The FW simulations include multiple reflections.

Near-field measurements

The next measurements were the radiation patterns using the near field setup, shown schematically in Fig. 3.13b. The radiated fields of the AUT were sampled using a scanner with a WR-5 probe. The Near field (NF) method was chosen over the FF method out of practicality: At 220 GHz the FF distance is at 1.32mm ($2D^2/\lambda$), requiring a large setup. Instead, the NF measurements require the use of a CNC machine to scan the probe over the AUT in its reactive fields. This is illustrated in Fig. 3.11a. A new S-parameter calibration was performed with again the reference plane indicated in red dashed line in Fig. 3.13b. In between the two reference planes, the three remaining elements were the AUT, the WR-5 probe and the channel between the two. Due to the latter two elements, absolute gain G cannot be derived from these measurements. Instead, the patterns will be normalized to their maxima and the absolute G will be derived later in section 3.3.1. For the NF method, probe correction has not been applied, as it was found in Arias Campo et al. [4] to have little effect on the measured outcome. Their measurement technique is the same as the one used in this work.

The Modern Antenna Handbook by Balanis [33], is used to derive the probe height, measuring grid, and angular region of validity. The probe is scanned in the xy -plane over a rectangular grid. The distance between measurement points fixed to $0.5\lambda = 0.68\text{mm}$ at 220GHz to avoid aliasing. The probe height of 4cm was chosen as a compromise between the required scan area and standing wave effects by the probe and AUT. The scan area in particular is important as it sets the validity angle, the angle up to which the far field results can be considered reliable. This validity angle is given by

$$\theta_v = \arctan\left(\frac{L - a}{2d}\right) \quad (3.2)$$

where L is the measurement grid length, a is the lens antenna diameter and d is the height of the probe above the lens. The scan area also sets the domain upon which

the FT is taken; the Handbook recommends that measurement data at the edges are ≈ -30 to -40 dB below the main lobe.

Based on Eq. 3.2, a grid size of 80×80 mm was chosen for broadside. Another parameter of importance was the IF bandwidth, where generally a larger (lower) IF bandwidth will give shorter (longer) measurement time but also an increase (decrease) in measured noise power. The broadside IF was set to 300Hz. Depending on the probe orientation, the CO-pol or CX-pol can be measured. The latter is obtained by simple 90° rotation of the E-plane orientated probe using a WR-5 waveguide twist, as shown in Fig. 3.11b.

The NF is then translated to the FF using the surface integral

$$\vec{E}^{ff}(r, \theta, \phi) \approx \iint_S jk \hat{R} \times \hat{I} \frac{e^{-jkR}}{4\pi R} \vec{M}_{eq} d\vec{S}' \quad (3.3)$$

where \vec{M}_{eq} is the Fourier transformed equivalent magnetic current distribution, derived from the S_{21} measurement grid. $\hat{R} \times \hat{I}$ represents the orthogonal projection of the electromagnetic fields to far-field observation direction \hat{R} . Finally, the term $\frac{e^{-jkR}}{4\pi R}$ takes into account the spreading over a spherical surface. Because \vec{M}_{eq} has an x- and y-component, its value is obtained by superimposing the CO- and CX-pol, respectively.

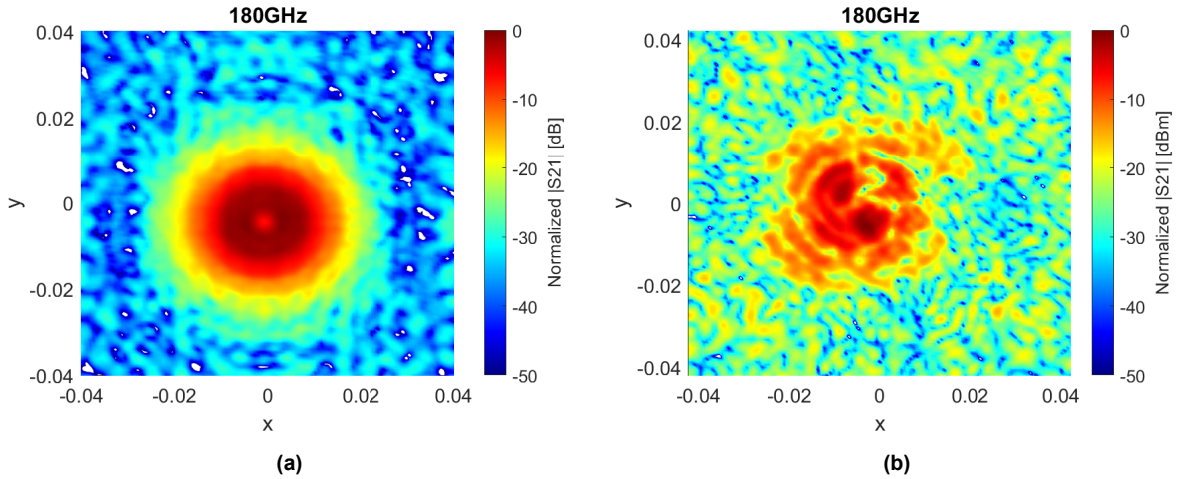


Figure 3.15: Two-dimensional near field results for the CO-pol (a) and CX-pol (b) broadside measurements. Shown 2D results are measured at 180GHz. Measurements are performed in 80×80 mm grids and IF of 300Hz for CO-pol and 70Hz for CX-pol.

Fig. 3.15a and 3.15b show the 180GHz NF broadside patterns for CO and CX, respectively. In both cases the 80×80 mm grid was used. However, the CO-pol was measured with an IF bandwidth of 300Hz, the CX-pol with 70Hz. The CO-pol results appear to satisfy the requirements of [33], with -30 to -50 dB at the edges. Results at other frequencies are shown in Appendix C.

The CX-pol, on the other hand, has proven to be more difficult to measure. Its results are shown in Fig. 3.15b, and fail to meet the NF requirements. This is due to multiple effects:

- The measured CX-pol S_{21} power is the result of AUT CX-pol coupled to the CO-pol of the probe as well as AUT CO-pol coupled to the probe CX-pol. This creates an uncertainty in the measurements [34].

- The CX-pol directivity is very sensitive to orientational errors. A slight rotational shift in the probe means that the probe will measure a combination of CO- and CX-pol.
- The nature of the CX-pol being >20 dB below the CO-pol means that the measurements will require a lower noise floor and additional measures against multiple reflections [33].

The CX-pol measurements will therefore be repeated in the near future. Additional measures to avoid multiple reflections and orientational errors will be taken accordingly.

The normalized broadside results of the FT transformation (Eq. 3.3) are shown in Fig. 3.16 for 140, 180 and 220GHz. Only the CO-pol measurements are taken into account, the CX-pol measurements are not reported here. As a reminder, the validity angle of this measurement is 32.2° (Eq. 3.2). The patterns are compared to FW simulations, showing overall agreement. Some discrepancy is observed around the side lobes of around 2dB difference. The patterns also appear to have shifted by $\approx 1^\circ$ in the E- and H-plane. This could be due to an elevation angle misalignment in the probe, causing a tilt in the measurement orientation. It could also be related to the a misalignment between the lens and the waveguide block. At 180GHz, the measured side lobe levels (SLL) are around -17dB, with a -3dB beam width of $\approx 3.6^\circ$.

Measurement of scanned beams

Using the alignment pins shown in Fig. 3.12a, the scanning patterns can also be measured and compared to FW simulations. The same procedure as the broadside case is performed, but now at scanning angles of 5° , 10° and 15° in both the E- and H-plane. A grid size of 80×80 mm was chosen for broadside. However, when measuring the scanning patterns, a larger NF scanning plane is required to accommodate the increased beam width and uncertainty in scan angle.

NF measurement results for $+15^\circ$ E-plane scanning are shown in Fig. 3.17a for 180GHz. The grid size has been increased to 80×93 mm with the same $\Delta x = \Delta y = 0.68$ mm. This brings the validity angle to $\pm 38.2^\circ$, according to Eq. 3.2. The same procedure was applied for the 5° and 10° angles in the E-plane. A summary of the NF results is presented in Appendix C

The resulting E-plane scanning FF, shown in Fig. 3.18, shows good agreement with its related FW plot. At a scanning angle of 15° , a -3dB beam width of $\approx 4^\circ$ is observed, together with a SLL of -11dB at 180GHz. These represent an increase of 0.4° and 6dB with respect to broadside, respectively. This increase in beam width and SLL cause deterioration of antenna directivity, something that will be discussed in section 3.3.1.

NF 180GHz $+15^\circ$ H-plane scanning results for NF measurements are shown in Fig. 3.17b. The grid size is only 70×75 mm, giving a validity angle of 26.2° in the H-plane. This grid size is admittedly too small, as some of the edges do not satisfy the -30dB relative to the main lobe condition. Grid sizes differed for other scanning measurements, see Appendix C for the results for H-plane 5° and 10° scanned beams.

The H-plane scanning FF is shown in Fig. 3.19. Again, the FW simulations and measurements show a nice match within the validity angle. This completes the measurements of radiation patterns.

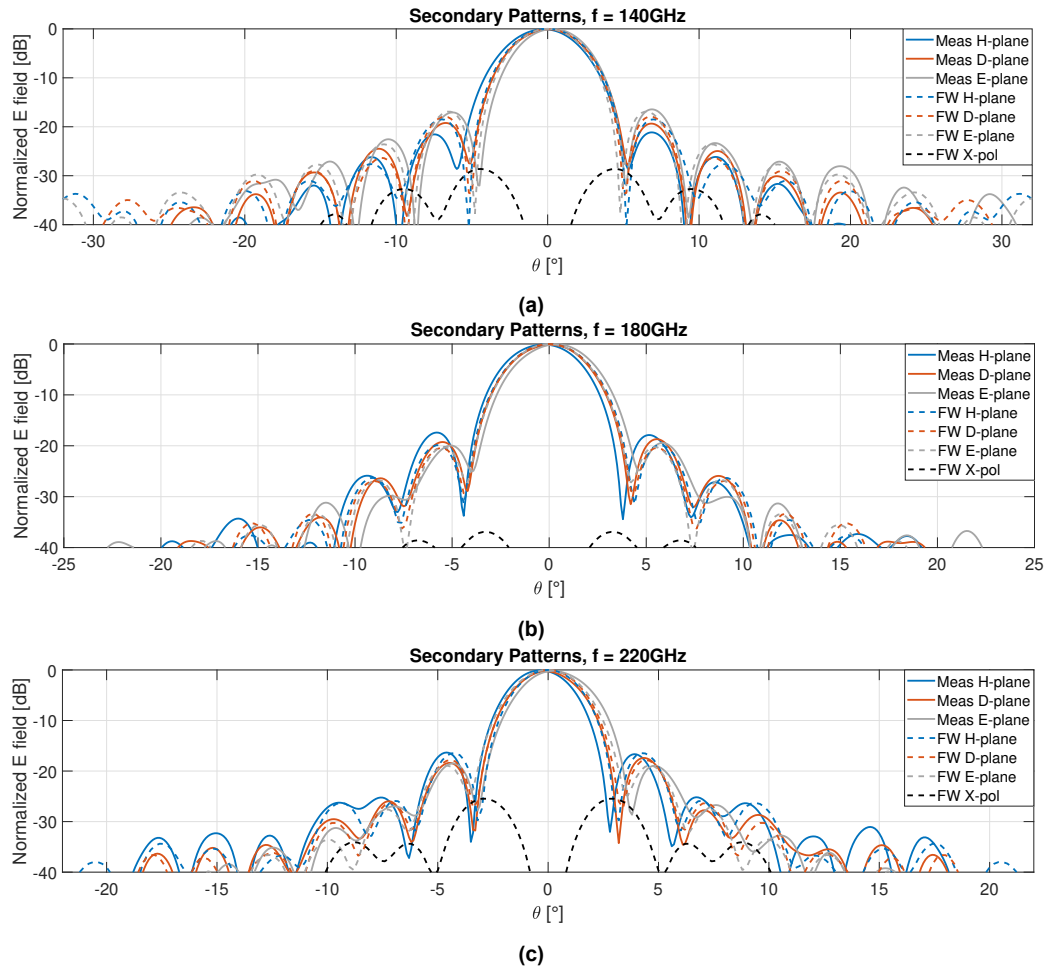


Figure 3.16: Broadside FF results, comparing the measurements (solid) to the FW results with multiple reflections and ohmic losses (dashed).

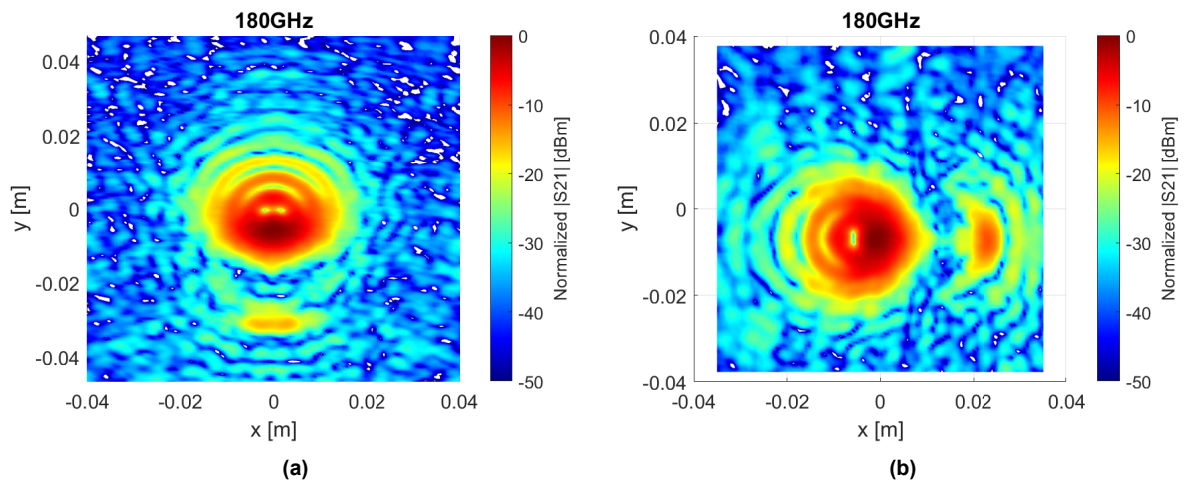


Figure 3.17: NF results for 15° at 180GHz in the E-plane (a) and the H-plane (b).

Directivity

Based on the measurement results of the secondary patterns, the Directivity D can be derived from the aforementioned results, according to

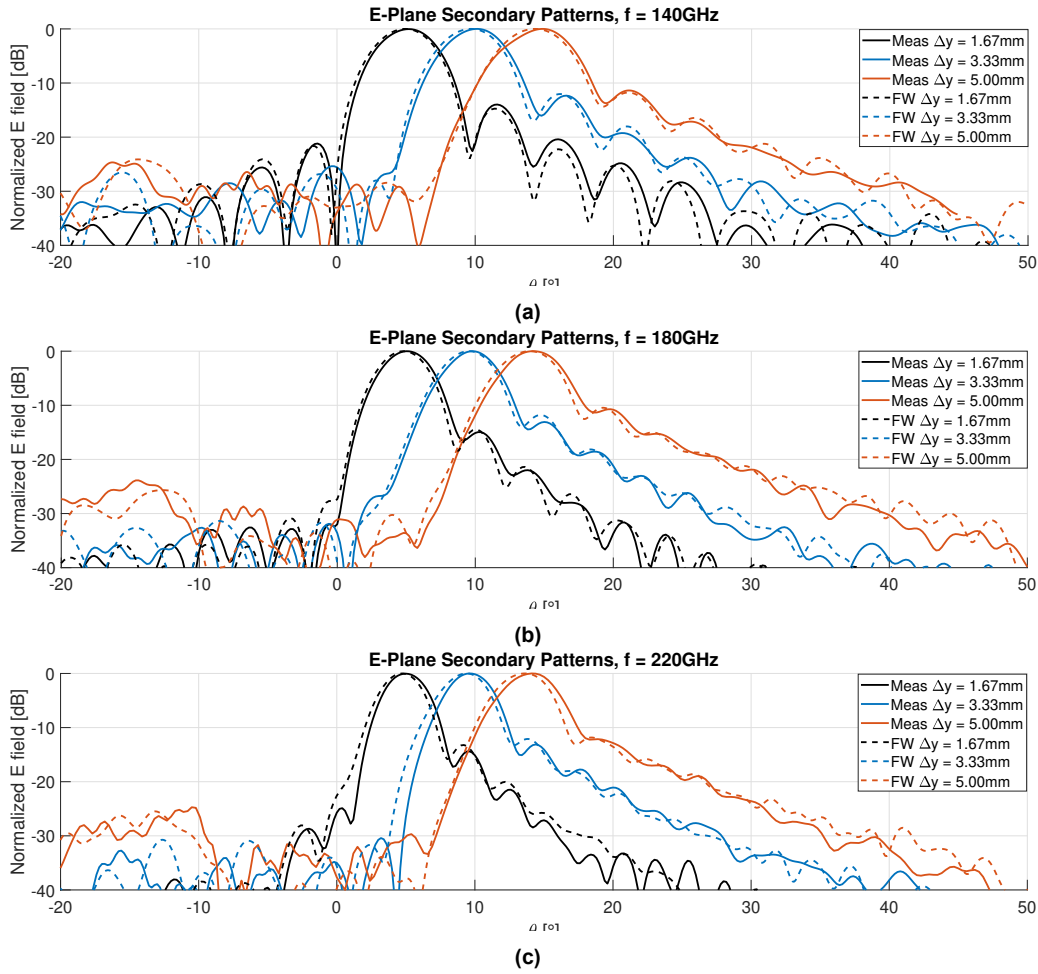


Figure 3.18: E-plane scanning pattern results, obtained from the near-field measurements.

$$D = \frac{4\pi U}{P_{rad}}, \quad (3.4)$$

where U is the radiation intensity for a given azimuthal and elevation angle [35]. P_{rad} is obtained by integrating the NF measured grid for both CO-pol and CX-pol, then summing both contributions. Repeating Eq. 3.4 for frequency, the results of Fig. 3.20 are obtained. Note that these data include the erroneous CX-pol measurements. However, because the CX-pol has relatively little radiated power compared to the CO-pol, the results do offer some reliability. The comparison to the FW simulations is made, and provides a close match to the measured data.

As observed in Fig. 3.17a, scanning the lens induces an increase in beamwidth and thus a loss in directivity. The scanning directivity is obtained using Eq. 3.4, but using the $P_{rad}(f)$ of the broadside measurements. This broadside P_{rad} does now not include the CX-pol power, as only the CO-pol has been measured for the scanning angles. The assumption here is that the ratio of CX-pol power and CO-pol power is independent of scanning angle. This procedure is done in Fig. 3.21 for the E-plane and the H-plane, and compared to FW CST simulations.

Several interesting conclusions can be drawn based on the results. Unsurprisingly, the act of beam scanning comes at the cost of a loss in directivity. This loss amounts

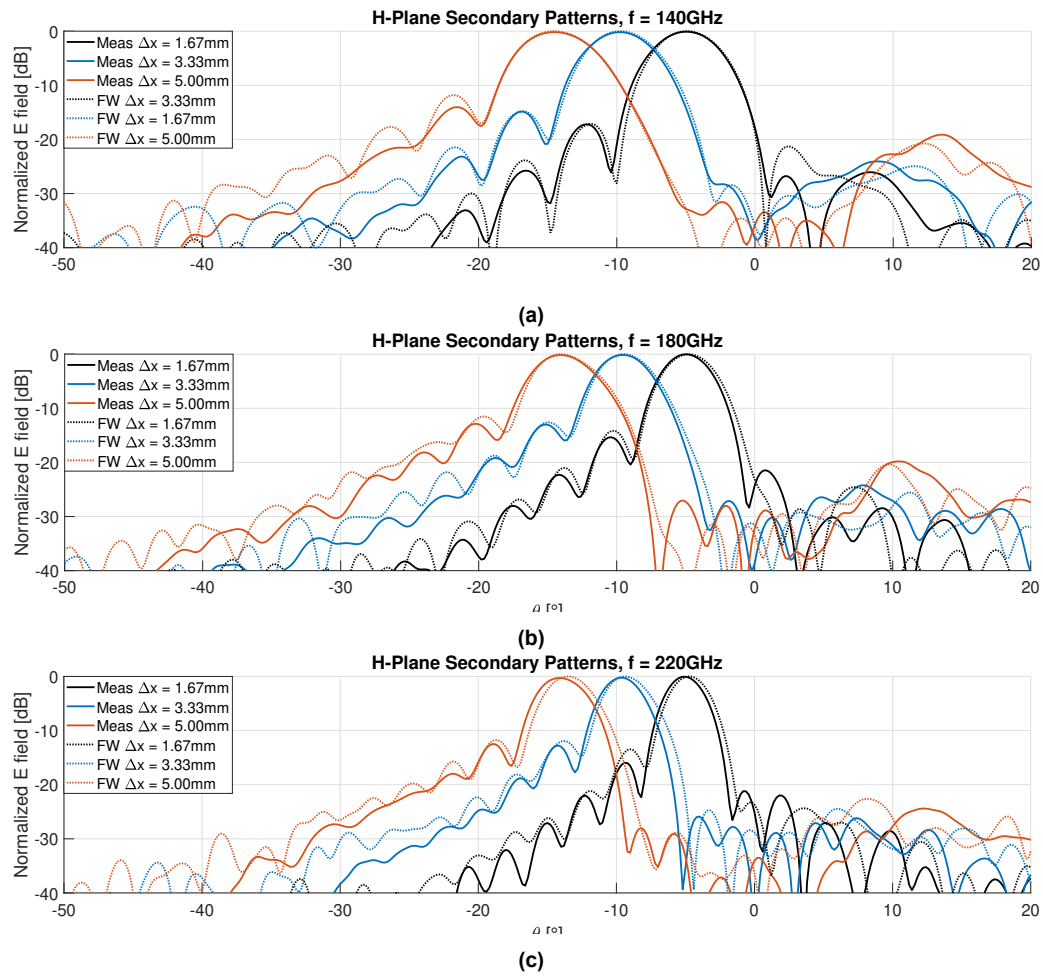


Figure 3.19: H-plane scanning pattern results.

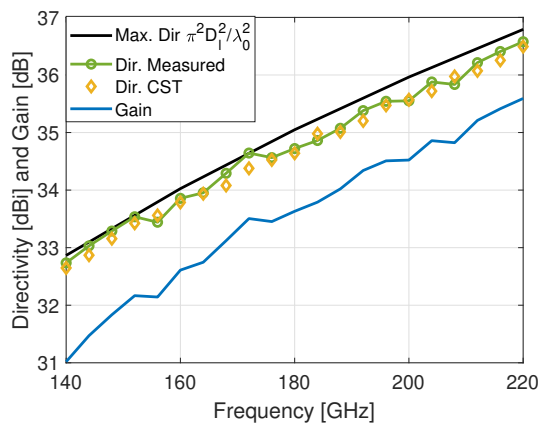


Figure 3.20: Measured broadside Directivity and Gain as a function of frequency.

to $> 3dB$ at 15° . The E-plane results are generally in agreement with the FW results. However, some discrepancy at largest scanning angles occur (max 0.8dB). The 5° and 10° H-plane measurements and FW results are relatively comparable. However, at 15° the differences are significantly larger ($> 1dB$). This is in large part due to the NF scanning domain that was too small, as discussed earlier in Section 3.3.1. This

smaller domain reduces radiation intensity U in Eq. 3.4, causing a loss in directivity. This is confirmed by the reduced discrepancy at higher frequencies, where the NF scanning domain is electrically larger.

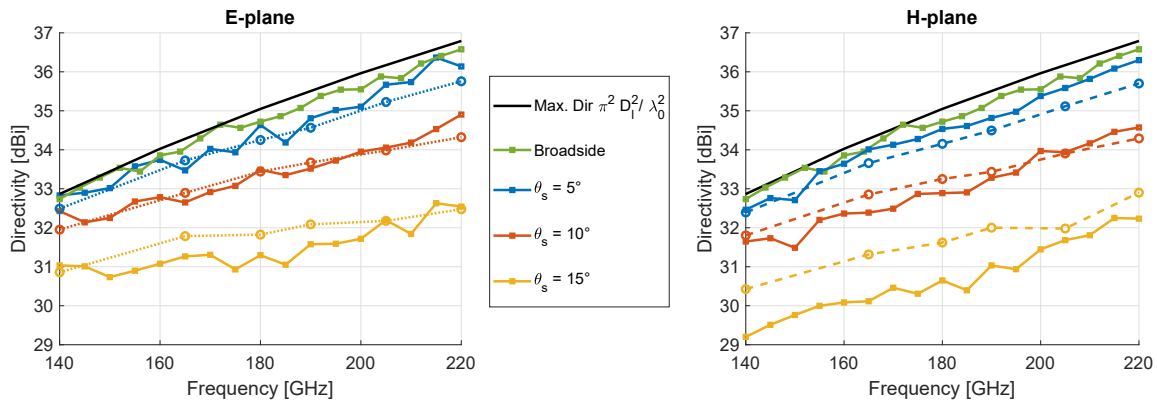


Figure 3.21: Measured directivity as a function of frequency for various E-plane (left) and H-plane (right) scanning angles. Maximum theoretical directivity is shown in black. FW simulations are indicated with the dotted lines, whereas the measurements are shown in solid.

Lens to lens coupling

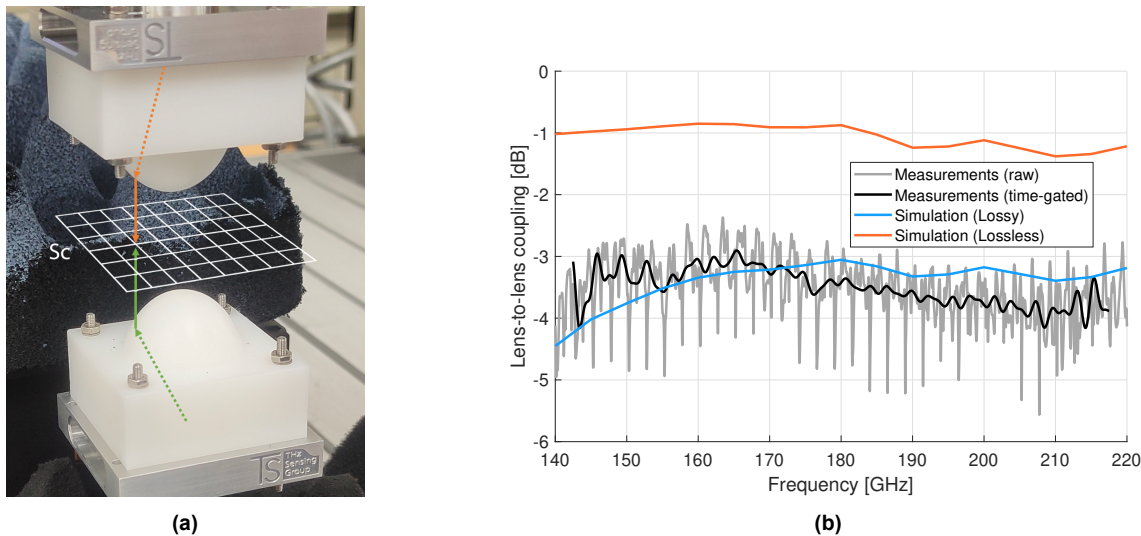


Figure 3.22: Lens to lens coupling setup (a) with the obtained measurement and analytical results (b).

The previous section was concerned with obtaining the normalized radiation patterns of the AUT. This normalization was necessary because the probe has not been characterized, thus providing no information for the absolute AUT gain. However, another method that involves two identical AUTs facing each other in the near field can be used to derive absolute gain. It provides a measure of the 'lens-to-lens' coupling, and can be determined both analytically and experimentally. This method, as presented in [4], is described in more detail in Appendix B. It takes into account the metallic, dielectric and reflection losses.

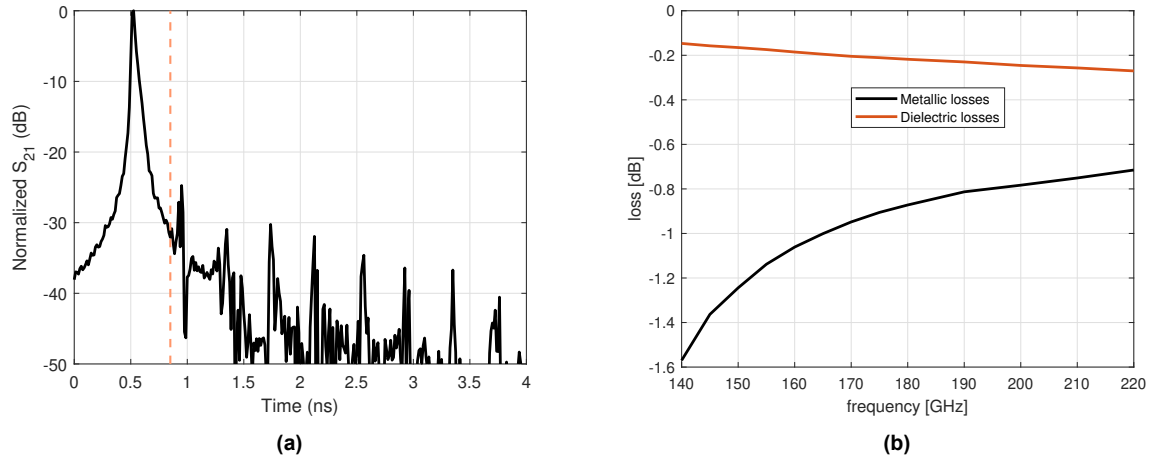


Figure 3.23: Time domain received S_{21} pulse, time gated at 0.85ns (a) and overview of ohmic losses as a function of frequency (b). For the metallic losses, $\sigma_{alu} = 4e5$ is used, whereas the dielectric is represented by a $\tan\delta = 0.00033$.

Consider the setup shown in Fig. 3.22a, where the two lenses are opposed at a distance of 15mm. Measuring the S_{21} as a function of frequency provides a measure of the combined antenna gain. This frequency is selected between 140GHz and 220GHz with 6k points. The IF bandwidth was set to 30Hz. The results are shown in Fig. 3.22b in gray. Multiple reflections from the ambience and AUT ground planes cause oscillatory behaviour. However, ample frequency points allow for time gating the results by means of an inverse FT, thereby transforming the frequency results to time domain. This result is visualized in Fig. 3.23a, and has been time gated after the first pulse at 0.85ns. The rest of the time signal is zero-padded. Performing the FT on this time gated signal, the result in black of Fig. 3.22b is obtained, indicating a reduced effect of oscillations. These results provide the degree of lens-to-lens coupling, and is found to be in between -3 and -4dB. This includes losses in both lens antennas.

These results can be compared to the analytical case, introduced in Appendix B. The analytical result is shown in Fig. 3.22b using the orange curve, expressed in dBs. Lossless Lens-to-lens coupling is thus estimated to be around -1dB. Dielectric and waveguide losses were included in the FW simulations. Loss parameters chosen were $\tan\delta = 0.00033$ for the HDPE material and $\sigma_{alu} = 4e5$ S/m for the aluminium conductivity (compared to $\sigma_{alu} = 3.6e5$ S/m of [4]). The latter is estimated by fitting the blue loss curve to the Measurement results, thereby accounting for the surface roughness of the material. Fig. 3.23b presents an overview of the losses as a function of frequency.

Finally having obtained an estimation of the losses, the antenna gain G can now be derived from the directivity. This is shown in blue in Fig. 3.20. The gain is 1.8dB to 1.2dB below the maximum attainable directivity, providing a radiation efficiency in the range of 66% to 75%.

3.4. Summary

This section presented the reader to our novel novel leaky-wave lens antenna concept for our proposed scanning lens phased array. The design has been compared to the

state of the art with simulations and measurements, indicating an overall higher aperture efficiency ($> 80\%$) and larger S_{11} bandwidth (1:2). Scanning behaviour was also measured, with acceptable ($< 3\text{dB}$ scan loss) performance at up to 15° of scanning. The lens-to-lens coupling method was used to derive the antenna gain, indicating radiation efficiencies between 66% and 75%. The high aperture efficiency makes the antenna suitable for use in the sparse array, that will be discussed in the next section.

Not every measurement has proven to be a success; The CX-pol and 15° H-plane scanning will require a revisit in the near future. Apart from these two cases, an overall good agreement was found between simulations and measurements. This concludes our study on the antenna element.

4

Scanning lens phased-array

The goal of this chapter is to develop a prototype of a scanning lens phased-array. This work is based on the newly proposed corrugated leaky-wave antenna from Chapter 3, combined with the electronic system design of Chapter 2. The frequency band was selected to be the WR-10 band (70-110GHz), with centre frequency of 90GHz. This due to the availability of multiple frequency extenders at the TU Delft.

In Section 4.1, we start with a brief discussion of the array's geometry. In Section 4.2, a full-wave solver is used to derive the performance of the lens array at broadside and scanning angles up to 20 degrees. Limitations due to maximum phase shifting (Chapter 2) are investigated and the scan loss of the array is presented. In Section 4.3, we present the CAD prototype that is currently being fabricated to corroborate the simulations. Finally, section 4.4 contains a summary of the Chapter.

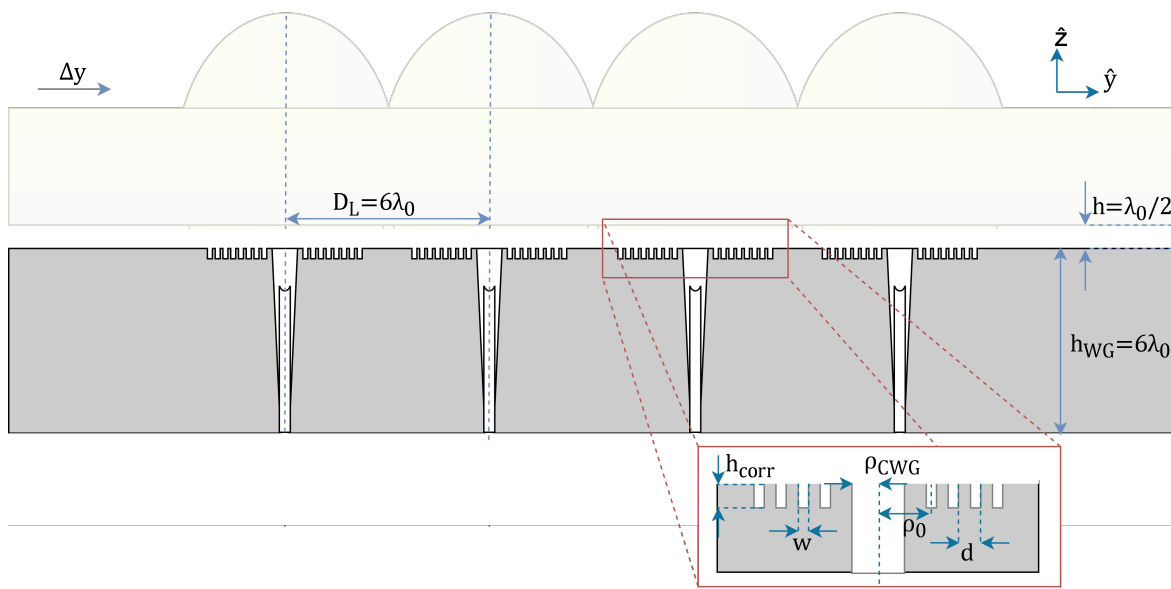


Figure 4.1: Geometry of 4×1 Array consisting of four WR-10 antenna elements. The $D_L = 6\lambda_0 = 20\text{mm}$ elements are merged on a ground plane with thickness $h_{WG} = 6\lambda_0 = 20\text{mm}$. Inter-element distances are equal to D_L . Finally, the air gap intersecting the dielectric lens structure and the ground plane has height $h = \lambda_0/2 = 1.67\text{mm}$.

4.1. Geometry

A cross-section of the 4×1 scanning lens phased-array is shown in Fig. 4.1. The array operates in the WR-10 bandwidth (70-110 GHz) with the central frequency of 90 GHz ($\lambda_0 = 3.33\text{mm}$). The array consists of four leaky-wave lens antenna elements that are fed by the leaky-wave stratification with annular corrugations in the ground plane, discussed in Chapter 3. The dimensions of the phased-array are summarized in Table 4.1. Each lens antenna element has a diameter of $D_L = 20\text{mm}$ ($= 6\lambda_0$). The lenses are fed by four circular waveguides in an aluminium block that is below the lenses. Each circular waveguide is tapered in the waveguide block to a rectangular WR-10 waveguide at the bottom, which is compatible with the Anritsu 3740A-EW waveguide frequency extenders. These extenders have the same functionality as the VDI WR5.1 VNA extenders (Chapter 2), but operate at the WR-10 band instead of the WR-5 band.

Table 4.1: Geometrical parameters for the 4×1 scanning lens phased-array.

| Parameter | Value [mm] | Value [λ_0] |
|---------------|--------------|-----------------------|
| ρ_0 | 2.3mm | $\lambda_0/1.4$ |
| ρ_{CWG} | 1.6mm | $\lambda_0/2.1$ |
| d | 0.75mm | $\lambda_0/4.4$ |
| h_{corr} | 1.1mm | $\lambda_0/3.0$ |
| w | 0.35mm | $\lambda_0/9.5$ |
| θ_{st} | 36.5° | n.a. |
| Δz | -2.2mm | $-\lambda_0/1.6$ |
| D_L | 20mm | $6\lambda_0$ |
| h_{WG} | 16.7mm | $5\lambda_0$ |
| h | 1.67mm | $0.5\lambda_0$ |

4.2. Performance of the Array

4.2.1. Broadside

A full-wave CST model was created to determine the broadside performance of the scanning lens phased-array. The model is shown in Fig. 4.2a. Simulations have been performed using the time-domain solver that stops when the power in the model is $\approx 30\text{dB}$ below the starting input power (roughly 1.9ns). The four antenna elements are excited simultaneously with equal phase and amplitude.

The lenses are modeled with a dielectric material with $\epsilon_r = 2.3$. Dielectric and metallic losses are simulated using the same conductivity and loss tangent are used as in Chapter 3; $\sigma_{alu} = 4e5\text{S/m}$ and $\tan\delta = 0.00033$, respectively.

The broadside active S-parameters, obtained by simultaneous excitation of all four antenna ports, are shown in Fig. 4.2b. The figure indicates that all four elements are matched below -14dB. Furthermore, there is hardly any variation between the individual active S parameters, indicating that the edge elements perform as well as the central elements.

The simulated ohmic losses are shown in Fig. 4.3a. These are the total losses

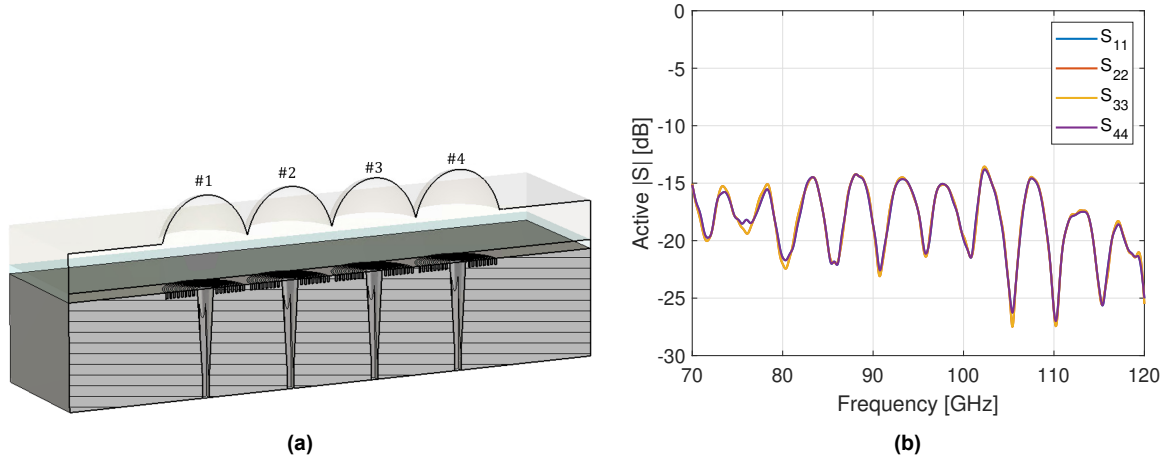


Figure 4.2: (a) Cross-section view of FW model with WR-10 4×1 Array and (b) active S-parameter magnitude as a function of frequency for all four antenna elements. The ports are numbered as defined in of (a)

obtained with all four antenna elements. Dielectric losses are very low at $\approx -0.08\text{dB}$, whereas the metallic losses are in the range of -1.2dB to -0.5dB . For the remainder of this chapter, the metal block is considered lossless (PEC) to limit the simulation time.

The broadside radiation patterns from this array model are shown in Fig. 4.8. The sidelobe level is plane- and frequency dependent: At 90GHz being -12dB , -14dB and -21dB along the E-, D-, and H-planes respectively. The cross-polarization levels are between -25dB and -32dB . This completes the analysis for broadside radiation. The next section will look at the phased-array performance during scanning.

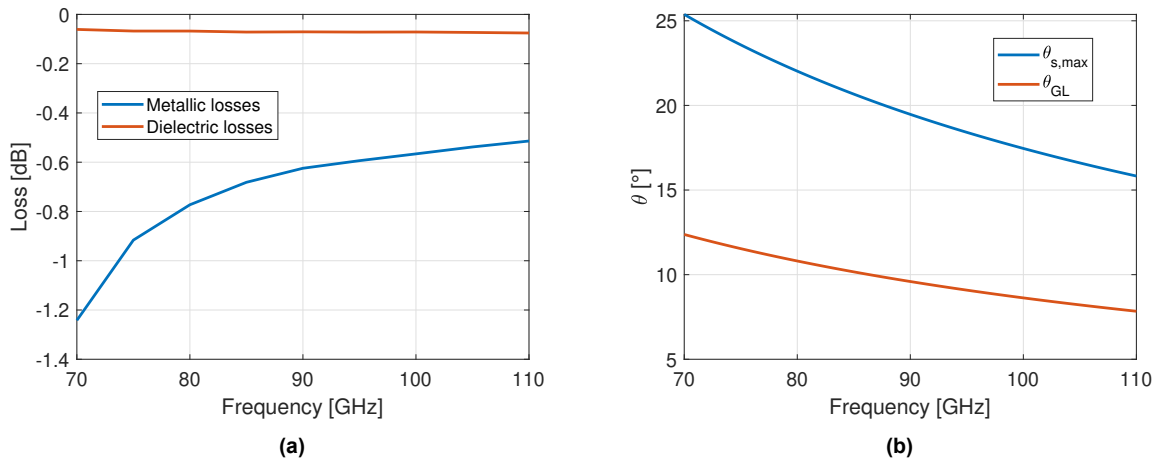


Figure 4.3: (a) the simulated array losses for the 4 × 1 array with $\sigma_{alu} = 4e5 \text{ S/m}$ and $\tan\delta = 0.00033$. (b) Maximum scanning angle and first grating lobe location as a function of frequency.

4.2.2. Scanned beam performance

Beam scanning of the lens phased-array is achieved by displacing the lens array along \hat{y} with respect to the metal block using a piezoelectric motor (Q-521 Q–Motion), combined with electronic phase steering of the sparse array factor.

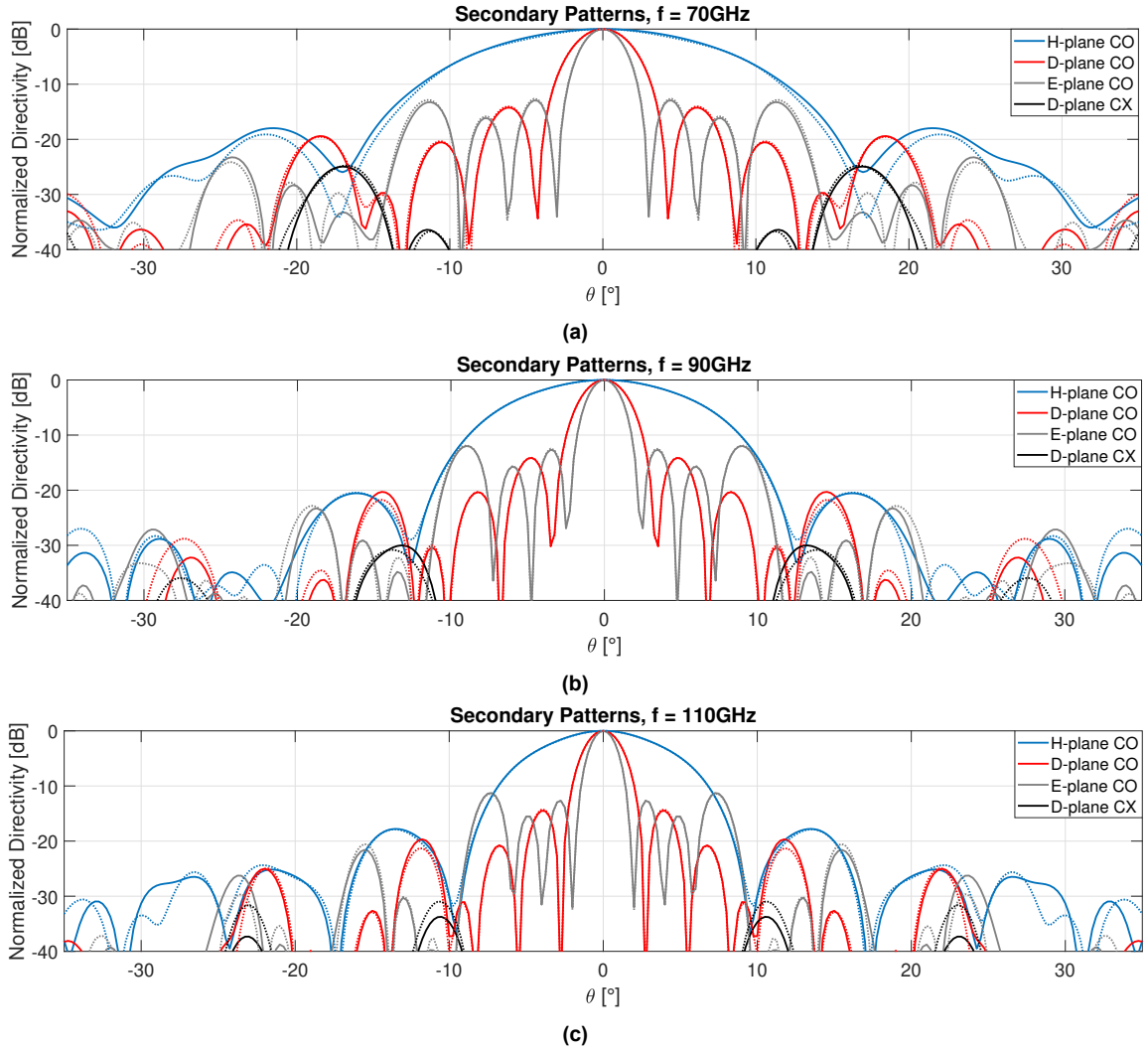


Figure 4.4: Full-wave secondary broadside patterns for the WR-10 frequency band. Solid lines indicate the 4×1 FW simulations, whereas the dotted lines represent the FW lens element multiplied by the corresponding AF.

The AF of a general array is given by [36]. Introducing to each element a uniform progressive phase shift β , main beam scanning towards θ_0 is obtained by setting the progressive phase shift to [35]

$$\beta = -kd_{x,y} \cos \theta_0, \quad (4.1)$$

where d is the phase constant and $d_{x,y}$ is the element spacing. The lenses are separated by $d_y = D_L$. The geometry of this array and its 90GHz AF were shown in Chapter 1. Due to the condition $d_y > \lambda_0/2$, grating lobes appear in this AF. Their angular positions θ_g are given by [35]

$$kd \sin \theta_g + \beta = \pm 2m\pi \text{ for } m = 1, 2, \dots, \quad (4.2)$$

and occur at integer multiples of 9.6° at 90GHz. Using this theory we can analyze the SLPA steering. The electrical phased-array AF steering is investigated first, followed by the mechanical steering of the element patterns.

The maximum possible electronic phase shift of 12π was derived in Chapter 2, leading to a maximum progressive phase shift per antenna element of $\beta_{max} = 4\pi$. The maximum scanning angle is then frequency-dependent and defined as [35]:

$$\theta_{s,max} = \sin^{-1}\left(\frac{\lambda\beta_{max}}{2\pi d}\right), \quad (4.3)$$

The maximum scanned angle using the provided β_{max} are shown in Fig. 4.3b versus frequency. For instance, at 90GHz and 110GHz the maximum scanning angles are 19.45° and 15.81° , respectively. This limits the scanned angle of the main beam of the array factor. However, the scanning range can be increased by scanning the element pattern to a grating lobe of the array factor. Since $\theta_{s,max}$ is strictly larger than the angle of the first grating lobe (Fig. 4.3b), the scan range is not limited by the array factor scanning. Instead, it is limited by the scan loss associated to the mechanical displacement of the array element. An example of the progressive phase shift values β_y , required for scan angle θ_s , is shown in Fig. 4.5a. The horizontal line indicates the maximum progressive phase shift of 4π . This is only one possible combination, as the same scan angle θ_s can be obtained using alternative grating lobes. These phase shifts can be inserted into the FW CST simulation when scanning. However, for our analysis this grating lobe method will not be used for the remainder of this work. This is done so that the wideband behaviour of the array can be captured, despite exceeding the maximum electronic phase shifting capability.

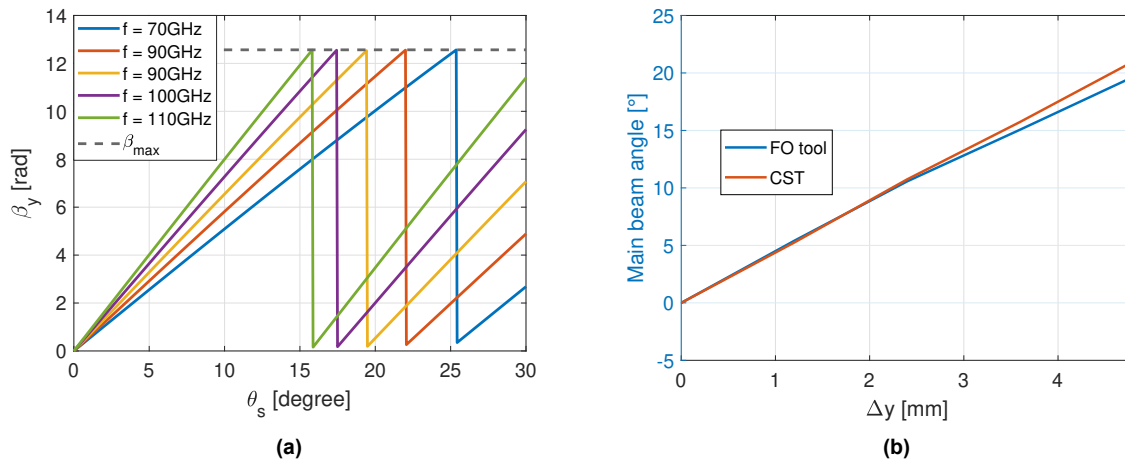


Figure 4.5: (a) the required progressive phase shifts β_y as a function of scanning angle for various frequencies. Black dashed line indicates the maximum progressive phase shift that can be obtained using the current WR-10 setup. (b) 90GHz lens element shift Δy versus scanning angle for the FO tool and FW simulations.

This electronic scanning is combined with the mechanical scanning by a corresponding Δy of the lens block of Fig. 4.2a. Fig. 4.5b shows the scanning angle as a function of mechanical steering for a single lens element, obtained using the GO-FO GUI and FW solver. The amount of mechanical Δy shifting required for 5° , 10° , 15° and 20° scan angle is roughly 1.2, 2.4, 3.6 and 4.5mm respectively. The actual scanning direction is slightly different when using FW simulations, caused by a GO current approximation limitation near the critical angle. This deviation is approximately 1 degree at $\Delta y = 4.8$ mm.

One way to visualize the scanning is by plotting the cross-sectional E-field. This is done at 90GHz for broadside and $\theta_s = 10^\circ$ in Fig. 4.6a and Fig. 4.6b, respectively.

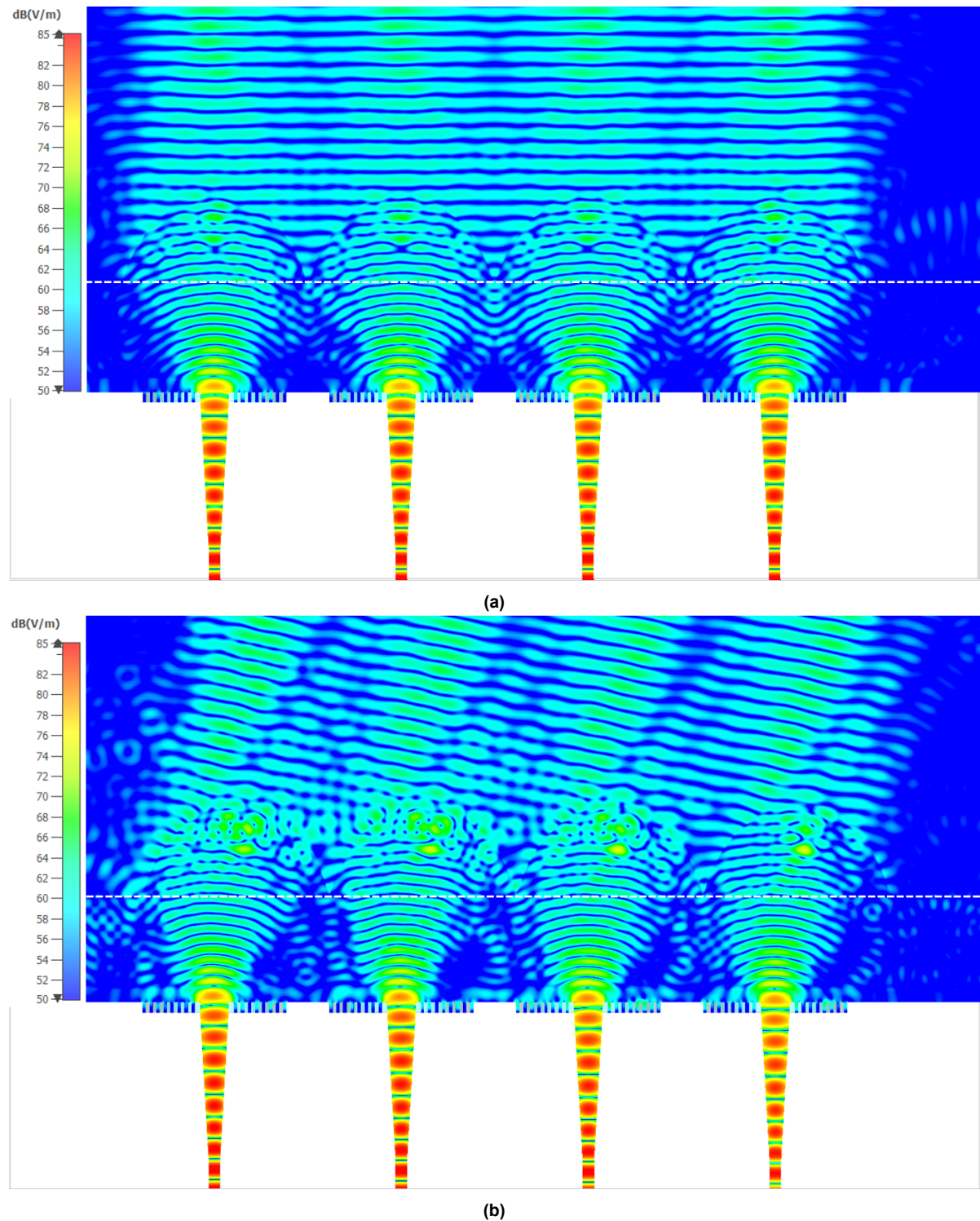


Figure 4.6: Cross-sectional ($x=0$) E-field of (a) broadside and (b) 10° scanning. The figure shows the electric field propagation from the waveguide (bottom) towards the lens-air interface and finally the free space medium on top. The white dashed line indicates the edge of the lens block.

Fig. 4.7 shows the E-plane patterns for three different scanning angles, with fre-

quency ranging from 70GHz (a) to 110GHz (c). It can be difficult to symmetrically balance the SLL around the main lobe. A trial- and error approach would have to be taken, with a single trial (simulation) taking up to 20 hours. With that being said, the 20° scan shows a significant increase in SLL: -9.5dB compared to -12dB at broadside 90GHz. Furthermore, the SLL is also largely dependent on frequency. The 70 and 110GHz have respectively lower and higher SLL compared to broadside, with highest SLL of -8dB at 110GHz 20°.

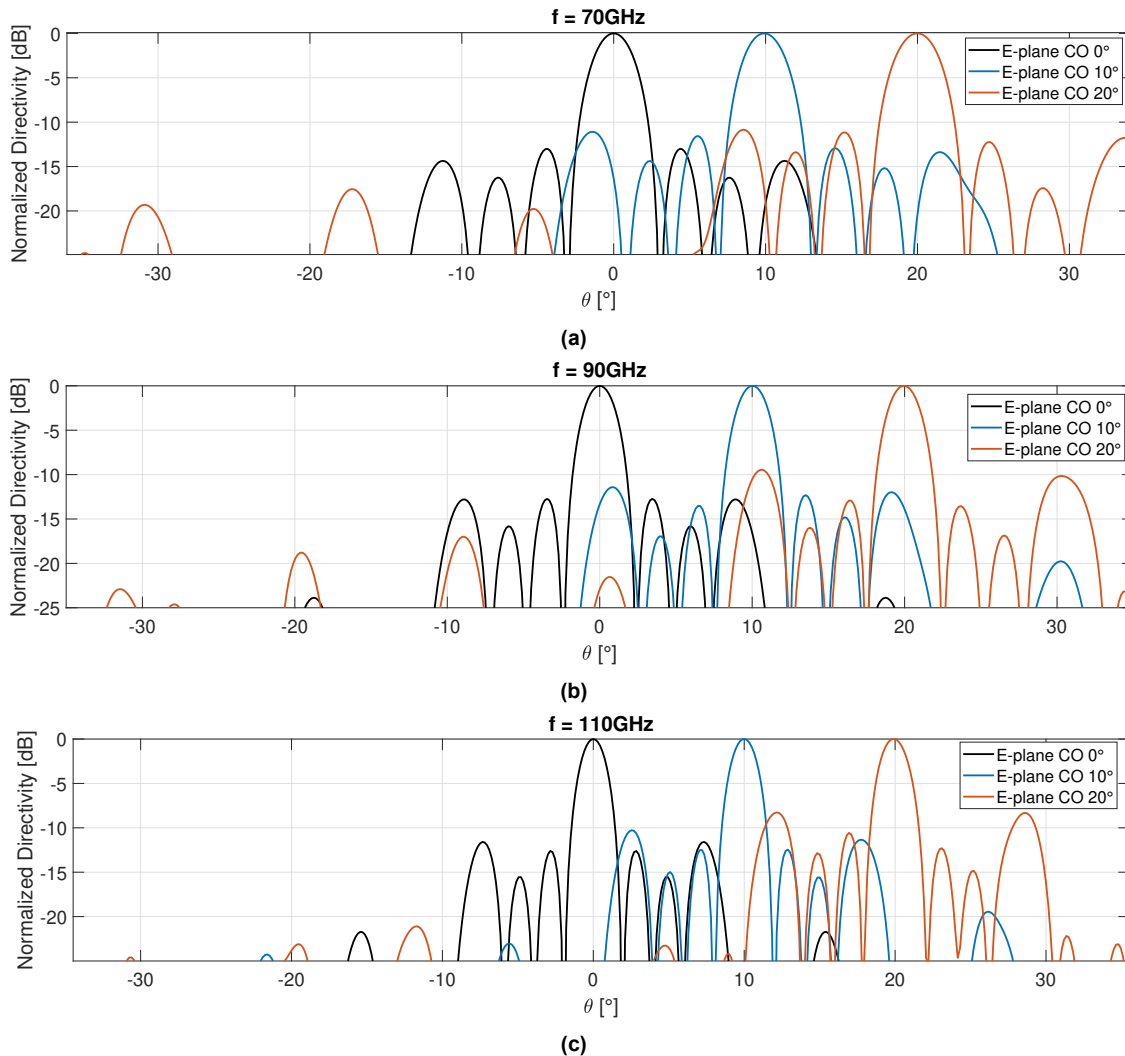


Figure 4.7: E-plane patterns at 70GHz (a), 90GHz (b) and 110GHz (c) for different scanning angles. Results are obtained using the FW CST 4×1 model of Fig. 4.2a.

Fig. 4.8a and Fig. 4.8b show the 90GHz CO-pol scanning along the H-plane and the D-plane, respectively. The scanning patterns have been spherically rotated in order to observe these planes. The H- and D-plane SLLs stay relatively constant around -20dB and -15dB, respectively. It is at angles $> \pm 10^\circ$ where the change in scanning angles lead to an increased variation in patterns. Finally, the D-plane CX-pol magnitude is plotted in Fig. 4.8c. The CX-pol increases significantly by up to 5dB as the beam is scanned.

To observe the negative scanning effects more clearly, the array directivity is shown

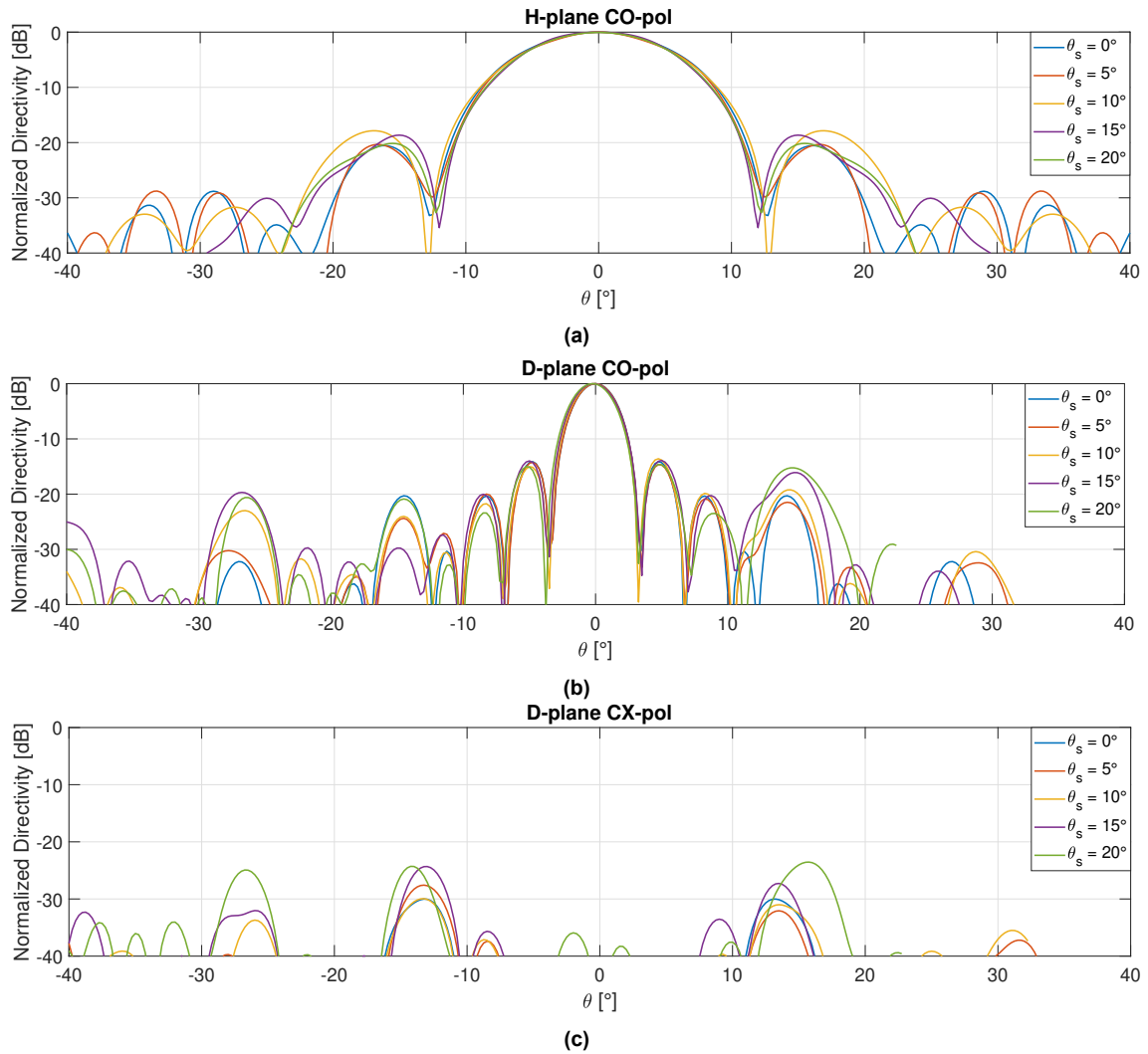


Figure 4.8: 90GHz FW 4×1 array patterns for the H-plane CO-pol (a), D-plane CO-pol (b) and D-plane CX-pol (c).

in Fig. 4.9a. Scan losses of around 3dB are observed for scanning angles of 20° . Likewise, the CX-pol magnitude for various scanning angles is shown in Fig. 4.9b. Scanning towards 20° results in an increase of CX-pol of at least 7dB. This can be explained partially due to the decrease in CO-pol directivity, as well as an increase in unnormalized CX-pol.

Scanning will also negatively effect the (Active) S-parameters. This is shown in Fig. 4.10a for 10° scanning and in Fig. 4.10b for 20° scanning. Comparing these figures to the original broadside case (Fig. 4.2b), we observe that the 10° scanning had very little impact on the active S-parameters. The act of 20° scanning caused an increase in asymmetry in the active S-parameters, but nevertheless remain well matched below -10dB.

4.2.3. Performance under phase and amplitude errors

Above mentioned results are obtained using ideal phases for all four elements. However, as discovered in Chapter 2, phase errors are present in the electronic system

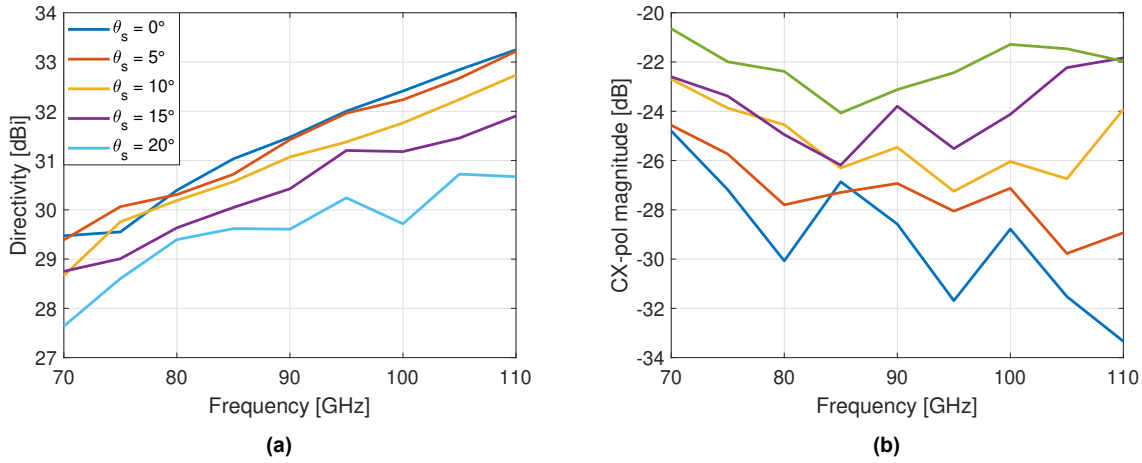


Figure 4.9: Simulated array directivity (a) and cx-pol (b) as a function of frequency for various scanning angles.

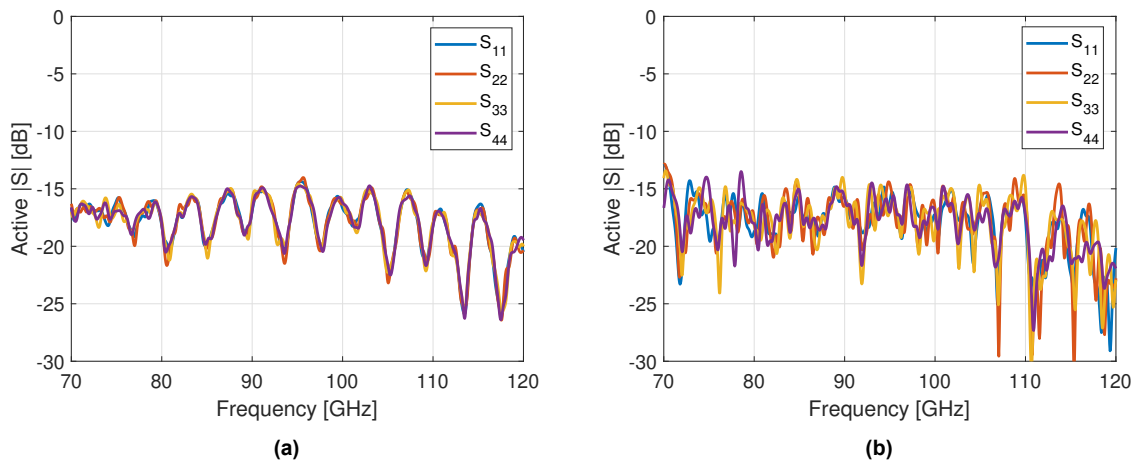


Figure 4.10: Active S-parameter results for 10° (a) and 20° (b) scanning.

due to drifts and noise. In Chapter 2, a relative input phase drift of $\pm 0.5^\circ$ around the mean ($\pm 3^\circ$ after frequency multiplication), and a relative amplitude drift of at most ± 0.15 dB were observed. The data set was limited to 24 hours, making it difficult to derive the most accurate statistical distribution. A Gaussian distribution will be used here, taking into account that the errors could increase beyond the current observation time.

A Monte Carlo approach was implemented to see the effects of these errors on the AF. The errors were added according to [23]: The phase shift errors ϕ_n for element $n = 1 \dots 4$ are incorporated onto the ideal progressive phase shifts by $e^{j\phi_n}$. The amplitude error δ_n is included in the ideal amplitude A_n by $(1 + \delta_n)A_n$. The standard deviations used for phase and amplitude are 3° and 0.15 dB, respectively. The process is repeated 5,000 times, resulting in the red curves in Fig. 4.11a. To make more sense of the data, the standard deviation of a total of 50,000 runs is shown in Fig. 4.11b, added and subtracted over the ideal AF. The phase and amplitude errors result in a maximum standard deviation at the sidelobes of 0.63 dB, shown by the red dotted line.

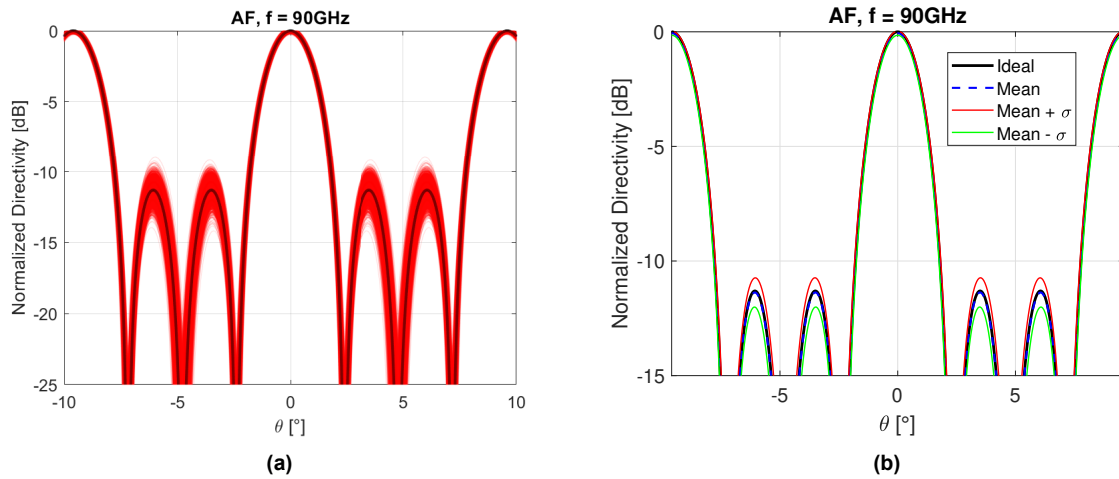


Figure 4.11: (a) Monte Carlo approach with 5.000 runs to determine the variation in SLL as phase and amplitude errors are introduced into the 90 GHz AF. The AF is described by the geometry of Fig. 4.1. (b) The 50.000 run standard deviation added (red) and subtracted (green) from the AF in red and green, replacing the red lines of (a).

4.2.4. Discussion

In this section, we presented the use of grating lobes to extend the scanning range of our SLPA. However, a downside of using the grating lobes for scanning is their frequency dependent location, requiring continuous wave operation. The solution could be increasing the multiplication factor, thereby achieving larger progressive phase shifts. These larger phase shifts could increase the maximum scanning angle, and thereby circumvent the need to scan with grating lobes. However, the increased multiplication factor also implies an increased multiplication of phase errors and, most likely, an increase in amplitude errors. Further research could focus on the validity of the current approach as the frequency is made increasingly higher.

4.3. Prototype development

A CAD model was designed using the commercially available software Solidworks [37]. An overview of the model is shown in Fig. 4.12. The parts that constitute the array prototype are each discussed in the following sections. The prototype is currently awaiting completion of fabrication by DEMO at the TU Delft.

4.3.1. Waveguide split block

The aluminum split-block contains the circular waveguides and the transition to the WR-10 rectangular waveguides. Shown in Fig. 4.13, the bottom contains the WR-10 waveguide flange adaptor that is compatible with the anritsu 3740a-ew frequency extenders. Pins are fitted between the two blocks for alignment and screws on one side of the waveguide block keep the split blocks together. The split block is fabricated from two solid blocks of aluminium using standard milling techniques.

Starting point in the design process was the WR-10 flange, which has a diameter of 19.05mm, shown in Fig. 4.13. It is for this reason that the distance between two flanges was set to 20mm, this to accommodate some fabrication margin and round the lens design to $6\lambda_0$.

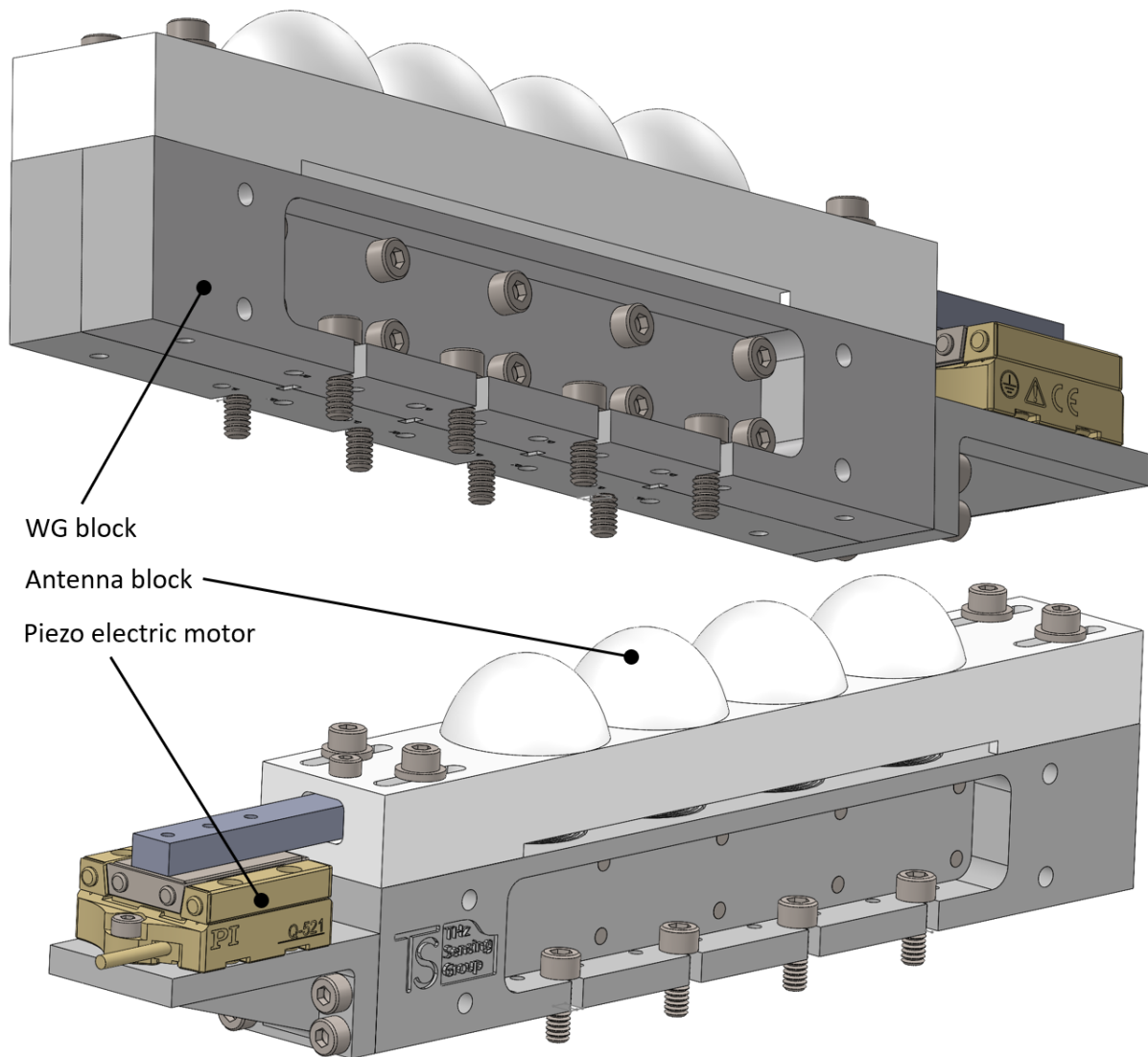


Figure 4.12: CAD model of the WR-10 array.

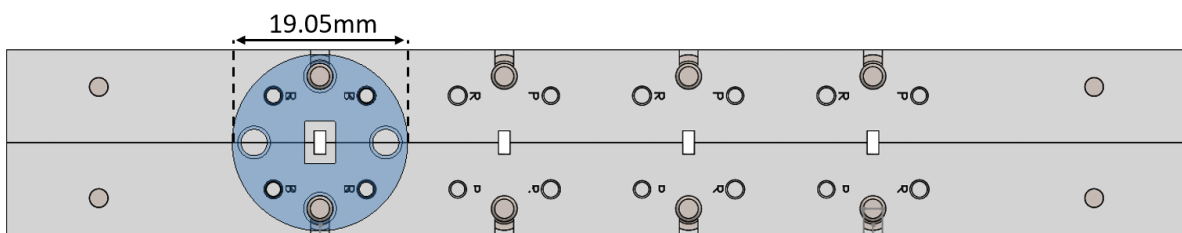


Figure 4.13: Bottom view orientation of the prototype. The WR-10 waveguide flange is overlaid in transparent blue.

The waveguide block is then formed, including the waveguide taperings, corrugations and the WR-10 flange adaptors. The width of the metallic block is the same as the lens diameter (20mm). This was done to save HDPE and aluminium material, but also for future-proofing: N identical arrays could be positioned alongside the 4×1 array to create a joined $4 \times N$ array.

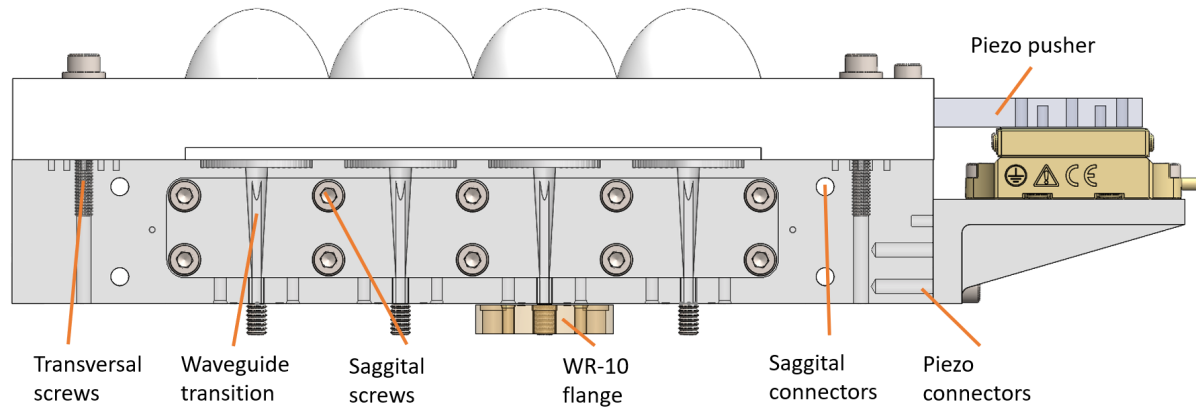


Figure 4.14: Frontal view orientation of the prototype where different the different screws are annotated.

4.3.2. Lens structure

Once the waveguide block had its basic shape, the lens array was designed to fit on top, see Fig. 4.14. The lens block was lengthened to 128mm to have ample clearance between the outer antenna elements and the connector screws. The height of the rectangular HDPE block housing the lenses is 11.28mm. The top of the lenses protrude only 23.22, significantly smaller than using a single lens with equal directivity.

The $\lambda_0/2$ air gap between the lens and metal blocks was cut out, leaving an opening as visible on the bottom of Fig. 4.12. This was imperative due to the reduced block width. A downside of this is that the sides are now left exposed to the elements and dust can accumulate in the corrugations or the waveguide. This problem can, however, easily be avoided by sealing the sides with a material of choice.

4.3.3. Piezoelectric motor

The next component to discuss is the piezoelectric actuator. This is a 'Q-521 Q-Motion', capable of displacing a mass of 300g horizontally. The lens is estimated to have a mass of around 31g. The actuator should therefore be powerful enough to move the lens, provided the friction is not too great. The lens and piezoelectric actuator are connected by a metallic block bridging the two components.

4.3.4. Screws and connectors

A variety of screws (mostly M2.5) are required to connect the different components together. These are indicated in frontal (semi-transparent) view in Fig. 4.14. The saggital connectors are left unthreaded and allow multiple arrays to be connected to each other. The waveguide block has been hollowed such that the flange screws can be mounted from both the upper and lower directions, making assembly easier. This is also shown in Fig. 4.12. The lens block is connected by transversal screws that will be tightened using springs. The lens block can slide along these transversal screws over a length of $\Delta y_{max} = \pm 6\text{mm}$. The longitudinal friction between the ground-plane and lens block is controllable by adjusting the spring constants and/or tightening of screws. The springs should provide enough transversal force to keep the lens in place, but also be loose enough for the piezoelectric actuator to push the lens to different positions.

The piezo-motor is connected to the waveguide block by an aluminium support, tightened with four M2 screws as well as two alignment pins. The reason for this separation of waveguide block and piezo-motor support block is because the piezo motor has its connecting screws along the split-line of the waveguide block. Splitting the piezo-motor support block would therefore interfere with the threading of the piezo-motor screw holes. It also saves space when the array is used without the piezoelectric motor.

The final component that will be discussed is the metallic 'lens pusher' that connects the piezoelectric actuator to the lens structure, as shown in Fig. 4.12. The lens has a cutout, allowing the lens pusher to be connected top-wise.

All components are combined using alignment pin and hole pairs. For every interface, two such pins are placed. Additional alignment pins are located on the ground-plane and lens block to allow for the discrete steering. This way, the array can be used without the piezoelectric actuator. These steering pins come in two pairs for added redundancy.

4.4. Summary and outlook

In this chapter the array performance using earlier obtained results from Chapter 2 and Chapter 3 was presented. The results show good performance with active S-parameter matching over the entire WR-10 band. Scanning behaviour was also analyzed, with -3dB scan loss at angles larger than 15° . CX-pol and SLL at broadside were less than -25dB and -12dB, respectively. The effects of phase and amplitude errors were evaluated on SLLs using a Monte Carlo approach, indicating a standard deviation of 0.63dB. The prototype is currently under development at DEMO workshop at the TU Delft.

5

Conclusion

The aim of this work was to demonstrate for the first time the dynamic steering of a high frequency scanning lens phased-array. In this thesis, the main challenges for this demonstration have been the following.

First, the development of a high frequency electronics architecture with enough accuracy and stability to provide beam steering with acceptable performance. Second, the design of lens antenna elements based on low ϵ_r materials that constitute the array with high aperture efficiency and bandwidth. The final challenge was designing an array prototype using the input from the two previous parts.

In chapter 2, an electronic steering system at 90GHz was designed and characterized using available frequency extenders. The phase steering is achieved by using IQ-mixers at 15GHz and $\times 6$ frequency extenders. A relative input phase drift of $\pm 0.5^\circ$ was observed, together with a relative amplitude drift of around 0.3dB. The relation between this input phase and the output phase was briefly discussed, arguing why this input phase could be a good indicator that the output phase drifts by $\pm 3^\circ$.

Chapter 3 presented the architecture and validation of the individual array elements. A lens antenna prototype based on a novel corrugated LW feed was developed in the WR-5 band. This prototype was measured with excellent agreement using FW simulations. This antenna has a S_{11} bandwidth of 1:2, aperture efficiency above 80%, low cross-pol and scanning capabilities up to 15° . The cross-polarization level could not yet be measured accurately, and will be remeasured in the upcoming months.

The success of the WR-5 element prompted the further development of the phased-array. Although the array has not yet completed its fabrication stage, its performance has been predicted using simulations in Chapter 4. Its radiation patterns, directivity, cross-polarization and side-lobe levels have been characterized for various scanning angles. For broadside, the active input reflection coefficients are matched over a 1:2 bandwidth. The antenna has a 31.5dBi directivity at 90GHz, with a 3dB scan loss near 20° . The effects of amplitude and phase errors on the array factor were analyzed using a Monte Carlo approach, where the standard deviation in side lobe level was found to be 0.63dB. Finally, a CAD model was developed for the array prototype, leading to its current fabrication by DEMO.

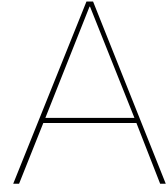
Bibliography

- [1] T. S. Rappaport, S. Sun, R. Mayzus, H. Zhao, Y. Azar, K. Wang, G. N. Wong, J. K. Schulz, M. Samimi, and F. Gutierrez, "Millimeter wave mobile communications for 5g cellular: It will work!" *IEEE Access*, vol. 1, pp. 335–349, 2013.
- [2] T. S. Rappaport, Y. Xing, O. Kanhere, S. Ju, A. Madanayake, S. Mandal, A. Alkhatteeb, and G. C. Trichopoulos, "Wireless communications and applications above 100 ghz: Opportunities and challenges for 6g and beyond," *IEEE Access*, vol. 7, pp. 78 729–78 757, 2019.
- [3] W. Roh, J.-Y. Seol, J. Park, B. Lee, J. Lee, Y. Kim, J. Cho, K. Cheun, and F. Aryanfar, "Millimeter-wave beamforming as an enabling technology for 5g cellular communications: theoretical feasibility and prototype results," *IEEE Communications Magazine*, vol. 52, no. 2, pp. 106–113, 2014.
- [4] M. Arias Campo, D. Blanco, S. Bruni, A. Neto, and N. Llombart, "On the use of fly's eye lenses with leaky-wave feeds for wideband communications," *IEEE Transactions on Antennas and Propagation*, vol. 68, no. 4, pp. 2480–2493, 2020.
- [5] S. Bosma, M. Alonso-delPino, C. Jung-Kubiak, D. Blanco, and N. Llombart, "Scanning lens phased array for submillimeter wavelengths," in *2019 44th International Conference on Infrared, Millimeter, and Terahertz Waves (IRMMW-THz)*, 2019, pp. 1–2.
- [6] B. Schoenlinner, X. Wu, J. Ebling, G. Eleftheriades, and G. Rebeiz, "Wide-scan spherical-lens antennas for automotive radars," *IEEE Transactions on Microwave Theory and Techniques*, vol. 50, no. 9, pp. 2166–2175, 2002.
- [7] D. Parker and D. Zimmermann, "Phased arrays - part 1: theory and architectures," *IEEE Transactions on Microwave Theory and Techniques*, vol. 50, no. 3, pp. 678–687, 2002.
- [8] R. Mailloux, L. Zahn, and A. Martinez, "Grating lobe control in limited scan arrays," *IEEE Transactions on Antennas and Propagation*, vol. 27, no. 1, pp. 79–85, 1979.
- [9] D. Blanco, E. Rajo-Iglesias, A. Montesano Benito, and N. Llombart, "Leaky-wave thinned phased array in pcb technology for telecommunication applications," *IEEE Transactions on Antennas and Propagation*, vol. 64, no. 10, pp. 4288–4296, 2016.
- [10] R. Gardelli, M. Albani, and F. Capolino, "Array thinning by using antennas in a fabry-perot cavity for gain enhancement," *IEEE Transactions on Antennas and Propagation*, vol. 54, no. 7, pp. 1979–1990, 2006.

- [11] Y. Yang, O. D. Gurbuz, and G. M. Rebeiz, "An eight-element 370–410-ghz phased-array transmitter in 45-nm cmos soi with peak eirp of 8–8.5 dbm," *IEEE Transactions on Microwave Theory and Techniques*, vol. 64, no. 12, pp. 4241–4249, 2016.
- [12] K. Guo, Y. Zhang, and P. Reynaert, "A 0.53-thz subharmonic injection-locked phased array with 63- μ w radiated power in 40-nm cmos," *IEEE Journal of Solid-State Circuits*, vol. 54, no. 2, pp. 380–391, 2019.
- [13] H. Jalili and O. Momeni, "A 0.34-thz wideband wide-angle 2-d steering phased array in 0.13- μ m sige bicmos," *IEEE Journal of Solid-State Circuits*, vol. 54, no. 9, pp. 2449–2461, 2019.
- [14] K. Sengupta and A. Hajimiri, "A 0.28 thz power-generation and beam-steering array in cmos based on distributed active radiators," *IEEE Journal of Solid-State Circuits*, vol. 47, no. 12, pp. 3013–3031, 2012.
- [15] W. Shin, B. Ku, O. Inac, Y. Ou, and G. M. Rebeiz, "A 108–114 ghz 4 \times 4 wafer-scale phased array transmitter with high-efficiency on-chip antennas," *IEEE Journal of Solid-State Circuits*, vol. 48, no. 9, pp. 2041–2055, 2013.
- [16] B. Avser, J. Pierro, and G. M. Rebeiz, "Random feeding networks for reducing the number of phase shifters in limited-scan arrays," *IEEE Transactions on Antennas and Propagation*, vol. 64, no. 11, pp. 4648–4658, 2016.
- [17] H. Zhang, S. Bosma, A. Neto, and N. Llombart, "A dual-polarized 27-dbi scanning lens phased array antenna for 5g point-to-point communications," *IEEE Transactions on Antennas and Propagation*, pp. 1–1, 2021.
- [18] A. Mozharovskiy, A. Artemenko, O. Soykin, and R. Maslennikov, "Lens array antenna for 71–76/81–86 ghz point-to-point applications," in *2016 46th European Microwave Conference (EuMC)*, 2016, pp. 1560–1563.
- [19] N. van Rooijen, S. Bosma, M. Alonso-delPino, and N. Llombart Juan, "Corrugated circular waveguide feeds for elliptical lens antenna phased-arrays (internship report)," 2020.
- [20] L. D'Addario, "Combining loss of a transmitting array due to phase errors," *Interplanetary Network Progress Report*, pp. 1–, 11 2008.
- [21] A. Visweswaran, C. de Martino, E. Sirignano, and M. Spirito, "An iq-steering technique for amplitude and phase control of mm-wave signals," in *2015 86th ARFTG Microwave Measurement Conference*, 2015, pp. 1–4.
- [22] S. Sabah and R. Lorenz, "Design and calibration of iq-mixers," in *6th European Particle Accelerator Conference 98, Stockholm, Sweden, 98'*, 1998, p. 1589.
- [23] R. J. Mailloux, *Phased Array Antenna Handbook*, 3rd ed. USA: Artech House, Inc., 2017.

- [24] Virginia Diodes Inc. (2021) Vna extension modules operational manual. [Online]. Available: https://www.vadiodes.com/images/Products/VNA/Product_Manual/VDI-707.1-VNAX-Product-Manual.pdf
- [25] G. S. Rani, S. Jayan, and K. V. Nagaraja, "An extension of golden section algorithm for n-variable functions with MATLAB code," *IOP Conference Series: Materials Science and Engineering*, vol. 577, p. 012175, dec 2019. [Online]. Available: <https://doi.org/10.1088/1757-899x/577/1/012175>
- [26] P. Burghignoli, "Phase centre of fabry-pérot cavity antennas: Leaky-wave model and analytical formulas," in *2012 6th European Conference on Antennas and Propagation (EUCAP)*, 2012, pp. 239–242.
- [27] A. Neto and N. Llombart, "Wideband localization of the dominant leaky wave poles in dielectric covered antennas," *IEEE Antennas and Wireless Propagation Letters*, vol. 5, pp. 549–551, 2006.
- [28] N. Llombart, G. Chattopadhyay, A. Skalare, and I. Mehdi, "Novel terahertz antenna based on a silicon lens fed by a leaky wave enhanced waveguide," *IEEE Transactions on Antennas and Propagation*, vol. 59, no. 6, pp. 2160–2168, 2011.
- [29] D. R. Jackson, P. Burghignoli, G. Lovat, F. Capolino, J. Chen, D. R. Wilton, and A. A. Oliner, "The fundamental physics of directive beaming at microwave and optical frequencies and the role of leaky waves," *Proceedings of the IEEE*, vol. 99, no. 10, pp. 1780–1805, 2011.
- [30] M. Alonso-delPino, N. van Rooijen, S. Bosma, and N. Llombart, "A wideband corrugated leaky-wave feed with low cross-pol for high efficiency lens illumination," 2020.
- [31] H. Zhang, S. O. Dabironezare, G. Carluccio, A. Neto, and N. Llombart, "A go/fo tool for analyzing quasi-optical systems in reception," in *2019 44th International Conference on Infrared, Millimeter, and Terahertz Waves (IRMMW-THz)*, 2019, pp. 1–2.
- [32] Cst microwave studio 2020. [Online]. Available: <https://www.3ds.com/products-services/simulia/products/cst-studio-suite/>
- [33] C. A. Balanis, *Near-Field Scanning Measurements: Theory and Practice*, 2008, pp. 929–976.
- [34] A. C. Newell, "Cross-polarization uncertainty in near-field probe correction [amta corner]," *Antennas and Propagation Magazine, IEEE*, vol. 51, 10 2009.
- [35] C. A. Balanis, *Antenna theory: analysis and design*. Wiley-Interscience, 2005.
- [36] H. Visser, *Array and phased array antenna basics*. United States: Wiley, 2005.
- [37] Dassault Systèmes. Solidworks 2017. [Online]. Available: <https://www.solidworks.com/>

-
- [38] M. Born, E. Wolf, A. B. Bhatia, P. C. Clemmow, D. Gabor, A. R. Stokes, A. M. Taylor, P. A. Wayman, and W. L. Wilcock, *Principles of Optics: Electromagnetic Theory of Propagation, Interference and Diffraction of Light*, 7th ed. Cambridge University Press, 1999.



Modeling techniques for lens antennas

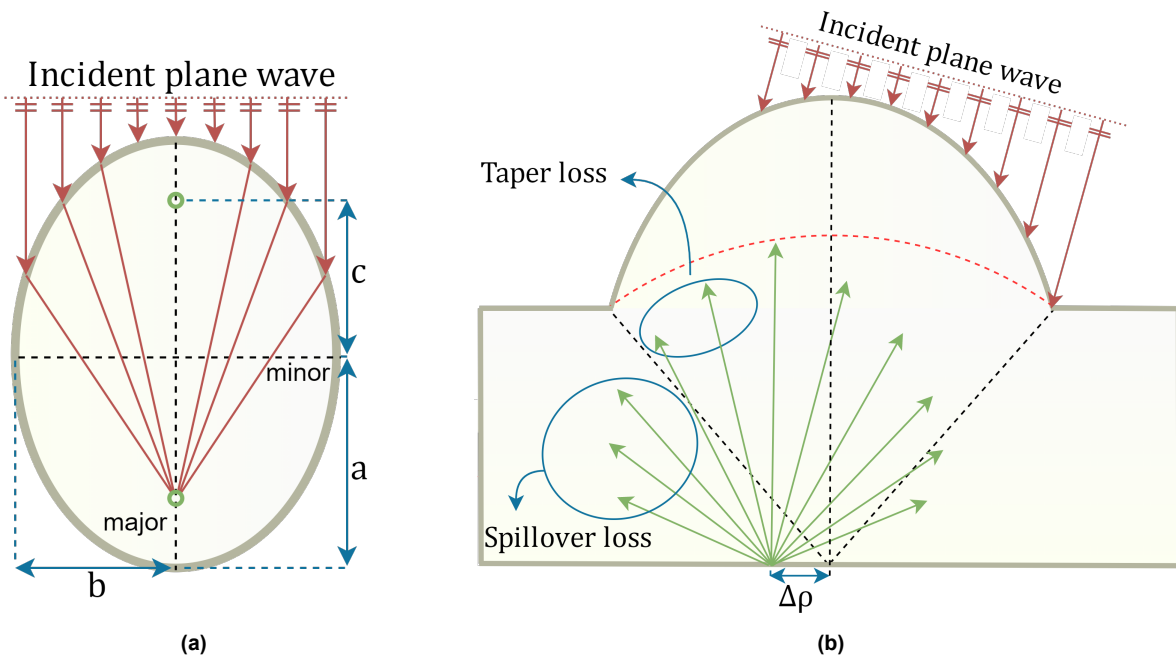


Figure A.1: (a) Elliptical geometry with two focal points indicated in green. (b) Truncated elliptical lens with oblique incident plane wave. The focal point is now shifted by $\Delta\rho$. Green arrows exemplify the feed radiation patterns including its taper- and spillover losses. Finally, the lens FO-sphere is shown in red dashed line.

In this section we describe the analysis and design procedure for integrated elliptical, dielectric lenses. The geometry of such a lens is shown in Fig. A.1a. Ellipsoids have two focal points, F_1 and F_2 , which are located on the major axis. The focal points are located at a distance $2c$ from each other. The ratio between the focal distance and the semi-major axis is the eccentricity of the lens, given by $e = \frac{c}{a}$. For dielectric lenses with permittivity ϵ_r , an eccentricity of $e = 1/\sqrt{\epsilon_r}$ [38] focuses rays from the lower focal point to parallel rays outside the lens. Ellipsoidal parameter b is given by $b^2 = a^2(1 - e^2)$. To avoid problems related to the critical angle (where total reflection occurs), not the entire ellipsoidal surface is used. Instead, the lens is truncated at a subtended angle θ_{st} , seen from the lower focus. This subtended angle is included in Fig. A.1b.

Lens focusing is not limited to broadside. Impinging Plane waves with oblique angles shift the focus point, as shown in Fig. A.1b. This shift, represented by a certain feed displacement ρ_s allows the antenna to scan to a desired direction θ_s, ϕ_s . Scanning is, however, limited due to scan losses. A practical displacement limit is given by $\Delta\rho_{s,max} = D_L/4$ [5].

To analyze such structures, we adopt the Fourier Optics (FO) methodology, as described in [31]. In this method, a plane wave incident on the lens with propagation vector \vec{k}_0 is propagated towards the FO-sphere, using Geometrical Optics (GO). This FO-sphere has a radius R_{FO} , centered at the lower focus of the lens and intersecting the edge of the lens, shown in Fig. A.1b. These incident fields intersecting the FO-sphere are named \vec{E}_i^{GO} . The patterns radiated by the feed antenna, \vec{E}^{TX} , are calculated in transmission over this FO-sphere. These primary patterns can be obtained using the Spectral Green's Function (SGF) approach or can be simulated using FW software.

A correlation integral between these two fields, \vec{E}_i^{GO} and \vec{E}^{TX} , can be used to determine the lens aperture efficiency, η_{ap} , and radiation pattern. The following equations are taken from [4]. Using a Thevenin equivalent circuit, the power received at a load (conjugately matched to the antenna input impedance), is given by

$$P_L = \frac{|V_{oc}I_{tx}|}{16P_{rad}} \quad (\text{A.1})$$

where P_{rad} is the total radiated power by the antenna feed and $V_{oc}I_{tx}$ is obtained using the spherical integral

$$V_{oc}I_{tx} = \frac{2}{\zeta_d} \int_0^{2\pi} \int_0^{\theta_{st}} \vec{E}_i^{GO} \cdot \vec{E}^{TX} e^{jk_0\Delta z \cos\theta} dS. \quad (\text{A.2})$$

ζ_d is the dielectric wave impedance. Finally, this allows for obtaining the η_{ap} with

$$\eta_{ap} = \frac{P_L}{P_{in}}, \quad (\text{A.3})$$

where P_{in} is the plane-wave power incident on the lens surface, $P_{in} = 1/(2\zeta_0) |E_0^{PW}|^2 A$, with A being the lens projected area seen by the incident plane wave [4].

The aperture efficiency can be split into two terms: The taper efficiency η_t and the spillover efficiency η_{sp} . The two are visualized in Fig. A.1b. The taper efficiency is a measure of the uniformity of the lens illumination in terms of amplitude and phase. The spillover efficiency in turn describes the ratio of feed radiated power over radiated power captured by the FO sphere. This also includes reflections at the air-lens interface. A GUI tool was developed by Zhang et al [31] to rapidly obtain the lens antenna performance, including antenna Gain G and η_{ap} , based on the primary patterns. The patterns radiated by the lens, the so called secondary patterns, are also derived using the GUI.

B

Lens-to-lens coupling

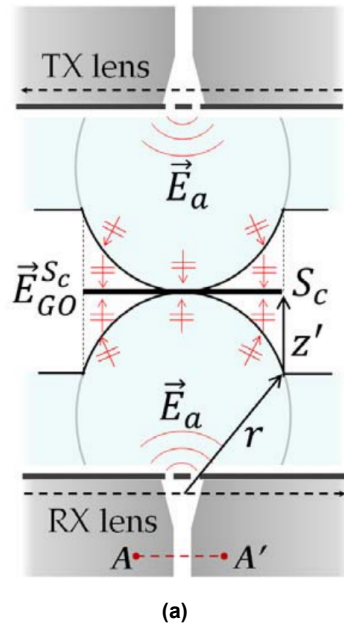
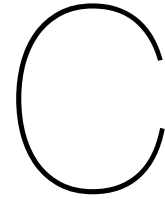


Figure B.1: Lens to lens coupling technique geometry, as presented in [[4], Fig. 16a]

Another lens analysis method that is used in this report is the lens-to-lens coupling, described by [4]. Two lenses are placed opposing each other in the near field, shown in Fig. B.1a. The FW primary E-field patterns are exported, referred to as E_{GO} . Using the reflection and transmission coefficients at the lens-air interface, E_{GO} is propagated towards S_c , the mutually shared x-y plane halfway between the two lenses. Naming the result $E_{GO}^{S_c}$, the coupling efficiency is given by the cylindrical reaction integral as

$$\eta_c = \frac{\left| \frac{2}{\zeta_0} \int_0^{2\pi} \int_0^{D_L/2} E_{GO}^{S_c}(\rho, \phi) \cdot E_{GO}^{S_c}(\rho, \phi) \rho d\rho d\phi \right|^2}{16P_{rad}^2}, \quad (\text{B.1})$$

where ζ_0 is the free-space impedance of 377Ω .



Additional near-field measurement results

A complete overview of the near-field measurements is presented here. The scanning setup is summarized in Table C.1. Fig. C.1 to Fig. C.4 show the normalized NF measurement results at for all scanning planes. The figures show the 140GHz results because this has the widest patterns. Therefore, the condition of having at least -30dB below the main lobe at the measurement edges is more strict.

Table C.1: Near field scanning parameter summary

| Scanning plane | IF BW [Hz] | Grid Size [mm×mm]^a | Validity angle [°]^b |
|-----------------------|-------------------|--------------------------------------|---------------------------------------|
| 0° broadside CO-pol | 300 | 80×80 | ±32.0 × ±32.0 |
| 0° broadside CX-pol | 70 | 80×80 | ±32.0 × ±32.0 |
| 5° E-plane CO-pol | 70 | 70×80 | ±26.6 × ±32.0 |
| 5° H-plane CO-pol | 300 | 80×80 | ±32.0 × ±32.0 |
| 10° E-plane CO-pol | 70 | 70×80 | ±26.6 × ±32.0 |
| 10° H-plane CO-pol | 50 | 88×88 | ±35.9 × ±35.9 |
| 15° E-plane CO-pol | 50 | 80×90 | ±32.0 × ±36.9 |
| 15° H-plane CO-pol | 70 | 70×75 | ±26.6 × ±29.4 |

^a In x- and y-direction, respectively

^b H- and E-plane, respectively

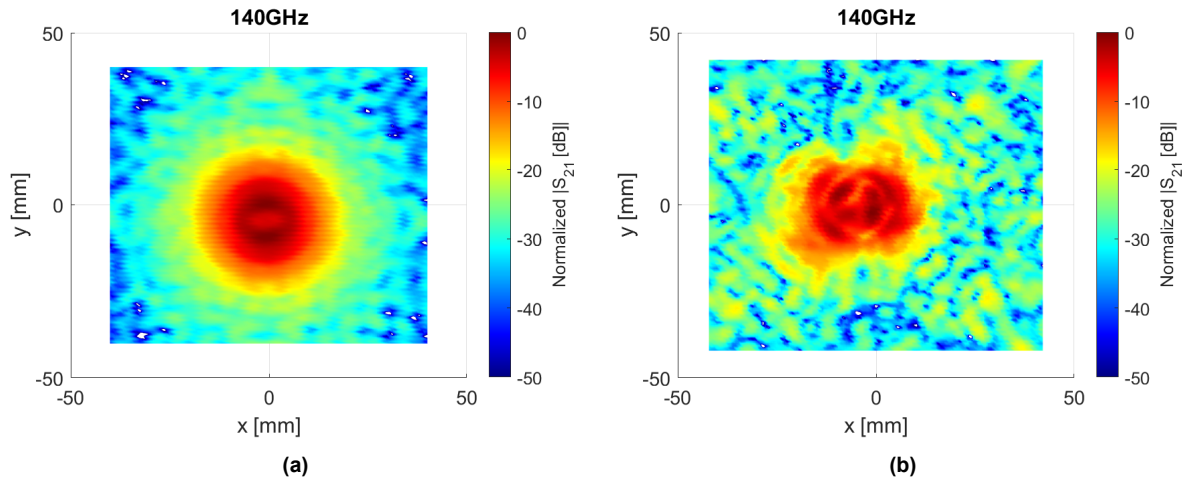


Figure C.1: (a) 140GHz CO-pol for broadside and (b) 140GHz CX-pol for broadside

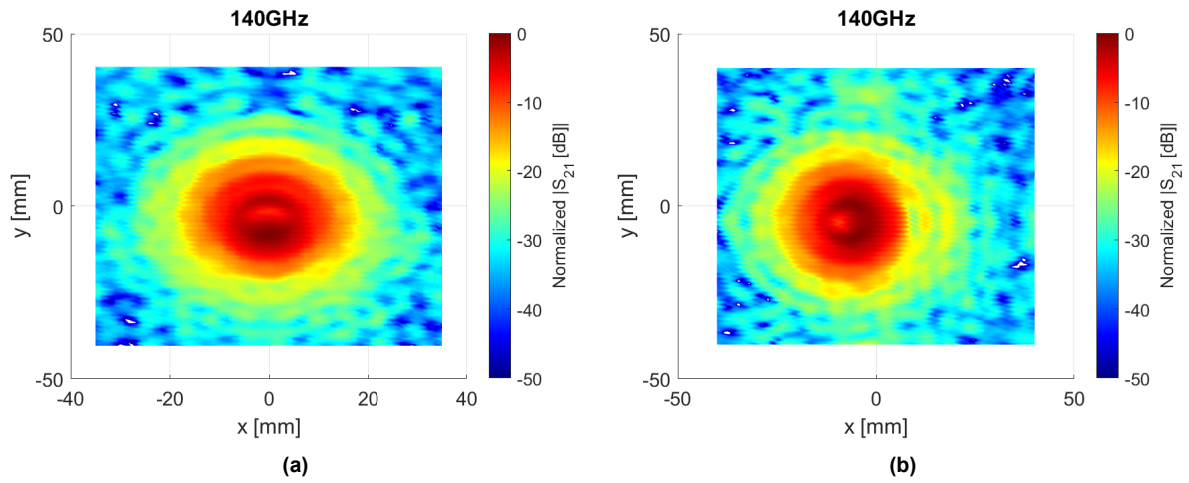


Figure C.2: (a) 140GHz CO-pol for E-plane 5° and (b) 140GHz CO-pol for H-plane 5° .

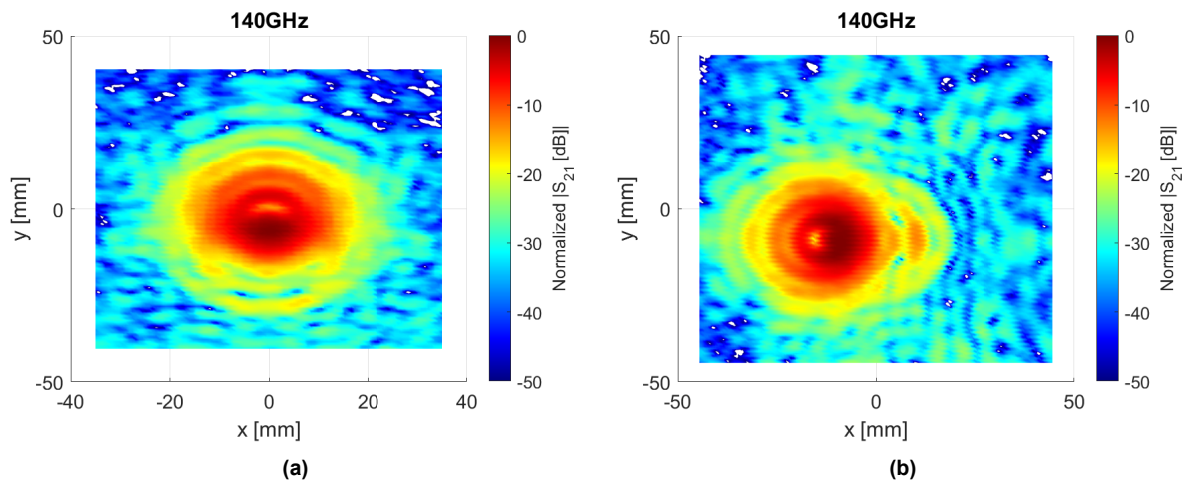


Figure C.3: (a) 140GHz CO-pol for E-plane 10° and (b) 140GHz CO-pol for H-plane 10° .

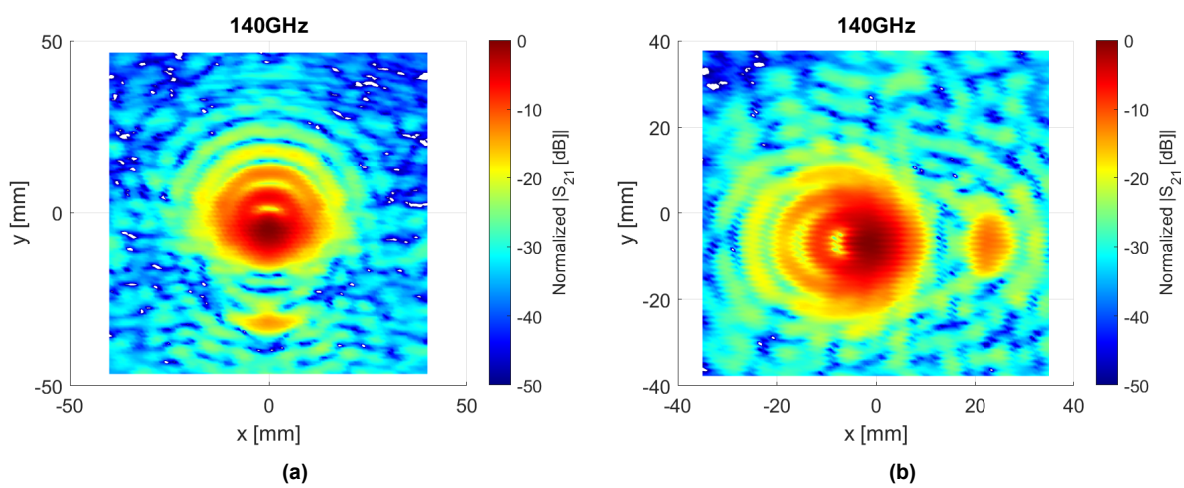


Figure C.4: (a) 140GHz CO-pol for E-plane 15° and (b) 140GHz CO-pol for H-plane 15° .